

BHLS₂, a New Breaking of the HLS Model and its Phenomenology

M. Benayoun^a, L. DelBuono^a, F. Jegerlehner^{b,c}

^a LPNHE des Universités Paris VI et Paris VII, IN2P3/CNRS, F-75252 Paris, France

^b Humboldt-Universität zu Berlin, Institut für Physik, Newtonstrasse 15, D-12489 Berlin, Germany

^c Deutsches Elektronen-Synchrotron (DESY), Platanenallee 6, D-15738 Zeuthen, Germany

January 9, 2020

Abstract

Previous studies have shown that the Hidden Local Symmetry (HLS) Model, supplied with appropriate symmetry breaking mechanisms, provides an Effective Lagrangian (BHLS) able to encompass a large number of processes within a unified framework. This allowed to design a global fit procedure which provides a fair simultaneous description of the e^+e^- annihilation into 6 final states ($\pi^+\pi^-$, $\pi^0\gamma$, $\eta\gamma$, $\pi^+\pi^-\pi^0$, K^+K^- , K_LK_S), the dipion spectrum in the τ decay and some more light meson decay partial widths. In this paper, additional breaking schemes are defined which improve the BHLS working and extend its scope so as to absorb spacelike processes within a new framework (BHLS₂). The phenomenology previously explored with BHLS is fully revisited in the BHLS₂ context with special emphasis on the ϕ mass region using all available data samples. It is shown that BHLS₂ addresses perfectly the close spacelike region covered by NA7 and Fermilab data; it is also shown that the recent Lattice QCD (LQCD) information on the pion form factor are accurately *predicted* by the BHLS₂ fit functions derived from fits to *only* annihilation data. The contribution to the muon anomalous magnetic moment a_μ^{th} of these annihilation channels over the range of validity of BHLS₂ (up to $\simeq 1.05$ GeV) is updated within the new BHLS₂ framework and shown to strongly reduce the former BHLS systematics. The uncertainty on $a_\mu^{\text{th}}(\sqrt{s} < 1.05 \text{ GeV})$ is much improved compared to standard approaches relying on direct integration methods of measured spectra. Using the BHLS₂ results, the leading order HVP contribution to the muon anomalous moment is $a_\mu^{\text{HVP-LO}} = 686.65 \pm 3.01 + (+1.16, -0.75)_{\text{syst}}$ in units of 10^{-10} . Using a conservative estimate for the light-by-light contribution, our evaluation for the muon anomalous magnetic moment is $a_\mu^{\text{th}} = [11\,659\,175.96 \pm 4.17 + (+1.16, -0.75)_{\text{syst}}] \times 10^{-10}$. The relationship between the dispersive and LQCD approaches to the $\rho^0 - \gamma$ mixing is also discussed which may amount to a shift of $\delta a_\mu[\pi\pi]_{\rho\gamma} = +(3.10 \pm 0.31) \times 10^{-10}$ at LO+NLO, presently treated as additional systematics. Taking also this shift into account, the difference $a_\mu^{\text{th}} - a_\mu^{\text{BNL}}$ exhibits a significance not smaller than 3.8σ .

1 Introduction

The Standard Model is widely recognized as the (gauge) theory which unifies the whole realm of weak, electromagnetic and strong interactions among quarks, leptons and the various gauge bosons (gluons, photons, W^\pm , Z^0). For the physics processes – and quantities – involving strong interactions, QCD is at work under two different regimes tightly connected with the energy involved and the onset of the perturbative regime is *a priori* expected to occur at high energies. However, as clearly shown by the data recently collected by KEDR [1, 2] on the ratio $R(s) = \sigma(e^+e^- \rightarrow \text{hadrons})/\sigma(e^+e^- \rightarrow \mu^+\mu^-)$, the $\{u, d, s\}$ sector of this ratio reaches the perturbative regime at energies as low as $\simeq 2.0$ GeV (see [3, 4], for instance); above this energy, the observed departures from perturbative QCD predictions – including, of course, the $c\bar{c}$ and $b\bar{b}$ threshold effects therein – are only spikes and narrow bumps associated with the charmonium and bottomonium states which require an additional specific treatment in the mass range where they are located.

However, in the low energy region where the non-perturbative regime of QCD is involved, getting theoretical predictions able to compete with the accuracy of some important experimental measurements may be challenging. This is, in particular, the issue met with the photon hadronic vacuum polarization (HVP), which contributes importantly to the muon anomalous magnetic moment a_μ , one of the best measured particle properties. The hadronic part of a_μ is related to the so-called $R(s)$ ratio and is given (at leading order) by :

$$a_\mu^{\text{had}} = \left[\frac{\alpha m_\mu}{3\pi} \right]^2 \int_{s_0}^{\infty} \frac{ds}{s^2} \hat{K}(s) R(s), \quad (1)$$

where $s_0 = m_{\pi^0}^2$ is the lowest hadronic threshold and $\hat{K}(s)$ is a known smoothly varying positive function [5]. The $1/s^2$ factor strongly enhances the low energy contribution of the spectrum, *i.e.* just in the validity domain of non-perturbative QCD. Fortunately, as obvious from the KEDR data [1, 2], one can undoubtedly consider that the non-perturbative regime does not extend to energies larger than $\simeq 2.0$ GeV.

So, the real issue with predictions for objects such as a_μ is to get precise estimates of the effects covered by the non-perturbative regime of QCD. Chiral Perturbation Theory (ChPT)[6, 7], the low energy limit of QCD, is of limited help for the present purpose as its realm does not extend much beyond the $400 \div 500$ MeV region and misses the quite important meson resonance mass region.

The most promising approach to the non-perturbative regime of QCD is certainly Lattice QCD (LQCD) which already provides valuable information at low energies [8]. The recently derived LQCD evaluations of a_μ^{had} [9, 10, 11, 12] have been found in accord with the experimental measurement performed at BNL [13, 14]. However, the magnitude of the reported uncertainties is by far too large to fruitfully compare with the already existing BNL datum and, *a fortiori*, with the measurements expected from the Fermilab experiment [15, 16], already running, or from the experiment planned to start later on at J-PARC [17], as both are expected to improve the uncertainties by a factor of 4. So much progress remains to be done before getting satisfactory uncertainties from LQCD.

This leaves room for low energy Effective Resonance Lagrangian Approaches, which can

contribute to improve the knowledge of a_μ^{had} by providing a good description of the rich amount of experimental data collected in the timelike region. Among the richest possible Lagrangians, the elegant Hidden Local Symmetry (HLS) Model [18] is worth to be considered; it has been proven to be equivalent to $R\chi\text{PT}$ [19, 20], provided consistency with the QCD asymptotic behavior is incorporated. It thus follows that the HLS model is a motivated and constraining QCD rooted framework, moreover, easy enough to handle in phenomenological applications.

The original HLS Model deals with the lowest vector meson nonet and provides a framework for hadron production in e^+e^- annihilation, naturally bounded by the ϕ mass region – *i.e.* up to $\simeq 1.05$ GeV. It thus represents a tool giving a handle on a mass region contributing for $\simeq 83\%$ of the total muon hadronic VP. The region extending from just above the ϕ meson mass to 2 GeV only contributes for 7%, slightly less than the $[2 \text{ GeV}, \infty]$ region (10%).

As such, the non-anomalous HLS Lagrangian [21] sets up a unified framework which encompasses the $e^+e^- \rightarrow \pi^+\pi^-$, $e^+e^- \rightarrow K^+K^-$ and $e^+e^- \rightarrow K^0\bar{K}^0$ annihilation channels; the $\tau^\pm \rightarrow \pi^\pm\pi^0\nu$ spectrum also belongs to the same framework, allowing naturally a simultaneous treatment of all the mentioned annihilation and decay processes. On the other hand, the HLS Model possesses an anomalous sector [22, 18] which also brings the $e^+e^- \rightarrow \pi^0\gamma$, $e^+e^- \rightarrow \eta\gamma$ and $e^+e^- \rightarrow \pi^+\pi^-\pi^0$ annihilation channels inside the same framework, together with some radiative decay modes and the dipion spectra in the $\eta/\eta' \rightarrow \pi^+\pi^-\gamma$ decays as shown in former studies [23, 24]. The annihilation channels just listed exhaust almost completely the processes contributing to a_μ^{had} below 1.05 GeV; indeed the missing channels¹ (4π , $2\pi\eta$, ...) contributes only $\simeq 2\%$ of the full HVP. Such a broken HLS (BHLS) Model has already been built up [25, 26] and shown to provide a pretty good simultaneous description of almost all data samples covering the six channels listed above up to $\simeq 1.05$ GeV. This work has also proved that there was no contradiction between the $e^+e^- \rightarrow \pi^+\pi^-$ and $\tau^\pm \rightarrow \pi^\pm\pi^0\nu$ spectra.

The non-anomalous [21] and anomalous [22] sectors of the HLS Model thus open a unified framework able to encompass a large corpus of data and physics processes. However, as such, the HLS framework – with only the universal vector coupling g as free parameter – cannot pretend to provide a satisfactory simultaneous description of the wide ensemble of high statistics data samples collected by several sophisticated experiments in several annihilation channels.

In order to achieve such a program, the HLS model must be supplied with appropriate symmetry breaking mechanisms not present in its original formulation [18]. A first successful attempt has been done in [25, 26, 27] which has set up a model (BHLS) based on a breaking mechanism originally proposed in [28], hereafter named BKY.

The present work reports on a new breaking scheme for the HLS model which aims at improving the behavior of the form factors in the dipion threshold region and also in the ϕ region where the original BHLS [25] meets some difficulty leading to introduce additional systematic uncertainties in the evaluation of the muon $g - 2$. The model (BHLS₂) presented here will be shown to widen the scope of BHLS, in particular to the spacelike domain and improve the BHLS prediction for the muon $g - 2$. Indeed, using variants of BHLS₂, together with the original BHLS should allow evaluating the model dependence effects in the estimates of derived physics quantities, noticeably the photon HVP.

The layout of the paper is as follows. Sections 2 gives a brief reminder of the original HLS

¹The $e^+e^- \rightarrow \eta'\gamma$ channel has been considered in [25, 26] and found to contribute to a_μ^{had} at the 10^{-12} level only and can thus be safely discarded.

model while Section 3 briefly reminds the BKY mechanism, still involved in BHLS₂. Sections 4 and 5 introduce a new breaking mechanism at the level of the covariant derivative which is the basic object leading to the original HLS model. Section 6 describes the $O(p^4)$ terms [18] of the HLS framework which are included in the BHLS₂ Lagrangian.

At this step, one has at hand the first variant of the BHLS₂ model, named Basic Solution (BS), and, relying on its vector meson mass term, Section 7 defines its parameter properties. Remarking that there is no fundamental reason why the neutral vector fields involved in physics processes should be their ideal combinations $(\rho_0^I, \omega^I, \phi^I)$, one allows for combinations of these via a mechanism called Primordial Mixing described in Section 8. This gives rise to a second variant of the BHLS₂ model, named Reference Solution (RS). In Section 9, one first reminds the parametrization of the propagators for the ω and ϕ fields [25] in connection with form factor behaviors at $s = 0$; this part of the work also shows that the breaking of nonet symmetry in the vector meson sector must be accompanied by breaking of SU(3) of the same intensity.

The dynamical breaking of vector meson [29, 25] is revisited in Section 10 and the role of anomalous loop corrections is emphasized, especially in order to connect smoothly the timelike and spacelike branches of the pion form factor. The derivation of the pion and kaon form factors is the subject of Section 11. The anomalous sector is fully analyzed in Section 12 and the cross sections for the $e^+e^- \rightarrow (\pi^0/\eta)\gamma$ and $e^+e^- \rightarrow \pi^+\pi^-\pi^0$ annihilations are derived.

Altogether, the above-listed Sections and the Appendix fully report on the BHLS₂ model properties and tools. Section 13 provides a comprehensive discussion of the available data samples falling into the BHLS₂ scope and their peculiarities. Relying on several preliminary studies, one comments here on the 3 discarded data samples; one should note that the number of data samples found to accommodate with each other within the BHLS₂ framework exceeds now 50 and the total number of data points reaches 1237.

Sections 15 and 16 give a full description of all aspects of the fits to the 6 annihilation channels performed within the global BHLS₂ framework. Moreover, Section 16 also provides a comprehensive analysis within our global framework of the existing $K\bar{K}$ data samples. The aim is to substantiate the issue between the BaBar, CMD-3 and CMD-2 spectra revealed by fits. A summary of the various fit properties is presented in Section 17.

The description of the spacelike region for the pion and kaon form factors as coming from BHLS₂ is the purpose of Section 18. The existing model-independent data for the π^\pm and K^\pm form factors are found to naturally accommodate our global framework, giving support to the low energy behavior predicted by BHLS₂ for all meson form factors. This fair agreement extends to the π^\pm form factor data provided by several Lattice QCD (LQCD) groups. One may infer from these data and from other model-dependent data that BHLS₂ should almost certainly apply down to $\simeq -1 \text{ GeV}^2$. The prediction for the K^0 form factor is shown to cope with expectations at $s \simeq 0$. Information on the charge radii of the π^\pm and K^\pm mesons is provided. Section 19 examines the P -wave $\pi\pi$ phase shift prediction and shows its agreement with data and other predictions, including our former BHLS, over an energy range extending up to the ϕ mass region.

The values found for some parameters, noticeably the a HLS parameter and some BKY breaking parameters, deserve a specific account given in Section 20.

The main motivation of the present work is the study of the BHLS₂ predictions and their consequences on the muon $g - 2$. This topic is addressed in Section 21. The part ($\simeq 83\%$) of the muon HVP contribution to a_μ covered by BHLS₂ is estimated in several contexts to

derive $a_\mu^{\text{HVP-LO}}(\sqrt{s} < 1.05 \text{ GeV})$ and estimate additional systematics possibly due to modeling effects and to observed tension among some data samples. Complementing this piece by the non-HLS part of the HVP derived by more usual means, one gives our best evaluation of the full HVP and our estimate of the muon anomalous magnetic moment. We also discuss an issue in the relationship between the LO-HVP results derived by dispersive approaches – in particular BHLS/BHLS₂ – and the LQCD results, where the $\rho^0 - \gamma$ mixing appears as a NLO effect. Comparison is done with other published evaluations for $a_\mu^{\text{HVP-LO}}$. Finally, Section 22 summarizes our results and conclusions.

2 Outline of the Hidden Local Symmetry (HLS) Model

Let us briefly outline the derivation of the HLS model². The usual ChPT Lagrangian [6, 7] can be written in two different manners [18, 30] :

$$\mathcal{L}_{\text{chiral}} = \frac{f_\pi^2}{4} \text{Tr} \left[\partial_\mu U \partial^\mu U^\dagger \right] = -\frac{f_\pi^2}{4} \text{Tr} \left[\partial_\mu \xi_L \xi_L^\dagger - \partial_\mu \xi_R \xi_R^\dagger \right]^2, \quad (2)$$

where f_π ($\approx 92.42 \text{ MeV}$) is the pion decay constant and :

$$U(x) = \exp [2iP(x)/f_\pi], \quad \xi_{R/L}(x) = \exp [\pm iP(x)/f_\pi] \implies U(x) = \xi_L^\dagger(x) \xi_R(x), \quad (3)$$

when working in the so-called unitary gauge which removes a scalar field term in the definition of $\xi_{R/L}(x)$; $P(x)$ is the pseudoscalar (PS) field matrix. The hidden local symmetry which gives its name to the HLS Lagrangian has transformation properties which affect $\xi_{R/L}(x)$ letting U unchanged. Ignoring for the moment the weak sector to ease the discussion, the HLS Lagrangian is derived by replacing in Equation (2) the usual derivative by the covariant derivative :

$$D_\mu \xi_{R/L} = \partial_\mu \xi_{R/L} - ig V_\mu \xi_{R/L} + ie \xi_{R/L} A_\mu Q, \quad (4)$$

where A_μ is the photon field, $Q = \text{Diag}[2/3, -1/3, -1/3]$ the quark charge matrix and V_μ is the vector field matrix; the expressions for P and V are the usual ones – fulfilling the $U(3)$ flavor symmetry – and can be found in [18, 30, 25]. In the expressions for $D_\mu \xi_{R/L}$, the universal vector coupling g occurs beside the unit electric charge e . The ω and ϕ fields occurring in the diagonal of the V matrix, also denoted V^I below, are the so-called ideal combinations generally denoted ω_I and ϕ_I .

Substituting the covariant derivative Equation (4) to the usual derivative in Equation (2), $\mathcal{L}_{\text{chiral}}$ becomes the first HLS Lagrangian piece denoted \mathcal{L}_A while another piece \mathcal{L}_V shows up which vanishes in the reversed substitution $D_\mu \Rightarrow \partial_\mu$:

$$\mathcal{L}_A = -\frac{f_\pi^2}{4} \text{Tr} \left[D_\mu \xi_L \xi_L^\dagger - D_\mu \xi_R \xi_R^\dagger \right]^2, \quad \mathcal{L}_V = -\frac{f_\pi^2}{4} \text{Tr} \left[D_\mu \xi_L \xi_L^\dagger + D_\mu \xi_R \xi_R^\dagger \right]^2. \quad (5)$$

The full HLS Lagrangian is then defined by :

$$\mathcal{L}_{\text{HLS}} = \mathcal{L}_A + a \mathcal{L}_V, \quad (6)$$

²See, for instance, [18] for a full derivation.

where a is a parameter specific of the HLS approach [18]. The usual VMD framework is obtained by setting $a = 2$ [30] while the presently reported phenomenology prefers larger values [24, 29]. The explicit expression for this unbroken \mathcal{L}_{HLS} can be found fully developed in [30]. Let us note that \mathcal{L}_{HLS} contains a photon mass term; however this Reference also showed that the loop dressing (in the HLS context) cancels out the physical photon mass and thus, this mass term can be safely ignored in phenomenological studies.

So, the unperturbed (*i.e.* unbroken) HLS Lagrangian depends on only two parameters (g and a) which can be adjusted using data; it is obviously unrealistic to expect this basic \mathcal{L}_{HLS} to describe precisely the large amount of data covering its scope with so few parameters. To have any chance to account for real data, additional input should enter the HLS Lagrangian to make it more flexible; this is what motivates the introduction of breaking procedures within the HLS framework.

As already noted, both HLS Lagrangian pieces fulfill a $U(N_f) \times U(N_f)$ symmetry and not $SU(N_f) \times SU(N_f)$. To reduce this symmetry which introduces a ninth PS meson, one includes [31, 25] the 't Hooft determinant terms [32] which break the axial $U(1)$ symmetry; this turns out to complement the \mathcal{L}_A Lagrangian piece with :

$$\mathcal{L}'_{\text{'tHooft}} = \frac{\mu^2}{2} \eta_0^2 + \frac{\lambda}{2} \partial_\mu \eta_0 \partial^\mu \eta_0 . \quad (7)$$

The singlet mass term manifestly breaks nonet symmetry in the PS sector. Nothing analogous affects the vector sector.

3 Breaking the HLS Lagrangian I : The BKY Mechanism

Up to now, a single breaking mechanism for the HLS Lagrangian has been proposed [28]; it is named here BKY after its proponent names. However, undesirable properties of the original BKY proposal have led to modifications of this breaking scheme [33, 34] originally proposed to break (only) the flavor symmetry of the Lagrangian. The "new scheme" variant from [34] has been analyzed with data and its results shown to compare fairly well to ChPT expectations [31]. It has been extended to include isospin breaking effects in [25] following the lines of [35]. This (modified) BKY breaking scheme, intended to cover isospin and $SU(3)$ breaking effects within the same framework, has been proved fairly successful, allowing for a high quality global fit of (almost) all available data covering the validity range of the HLS model [25, 26, 27] : e^+e^- annihilations, τ decay spectra and radiative decays of light flavor mesons; in particular, the dipion spectra in the $\eta/\eta' \rightarrow \pi^+\pi^-\gamma$ decays are fairly well predicted [23, 24], especially the detailed form of the drop-off in the $\rho - \omega$ interference region as recently measured at BESIII [36, 37]. Nevertheless, as already stated in [25, 26, 27], the description of the threshold region in the dipion spectrum and of the ϕ mass region in the three pion annihilation channel deserves improvements; this issue is addressed by the present paper.

As BKY is one of the breaking mechanisms used in the present work, let us briefly remind how it is implemented. To lighten writing, we use the notations $L = D_\mu \xi_L \xi_L^\dagger$ and $R = D_\mu \xi_R \xi_R^\dagger$. The (modified and extended) BKY breaking which also underlies the broken HLS (BHLS) model developed in [25] turns out to modify Equations (5) as follows :

$$\mathcal{L}_A = -\frac{f_\pi^2}{4} \text{Tr} [(L - R)X_A]^2 \quad , \quad \mathcal{L}_V = -\frac{f_\pi^2}{4} \text{Tr} [(L + R)X_V]^2 \quad , \quad (8)$$

where $X_{A/V} = \text{Diag}(q_{A/V}, y_{A/V}, z_{A/V})$ are constant real matrices. In practice, one prefers setting $q_{A/V} = 1 + (\Sigma_{A/V} + \Delta_{A/V})/2$ and $y_{A/V} = 1 + (\Sigma_{A/V} - \Delta_{A/V})/2$. As $z_{A/V}$ are affecting the $s\bar{s}$ entries, their departure from 1 can be large compared to $q_{A/V}$ and $y_{A/V}$ – which refer to resp. the $u\bar{u}$ and $d\bar{d}$ entries; so, the Σ 's and Δ 's are expected small. Within the previous broken HLS framework – hereafter named BHLS – [25, 26], one got $z_A \simeq [f_K/f_\pi] \simeq 1.5$, $z_V \simeq 1.2$ while the Σ 's and Δ 's were found at the few percent level.

Once these breakings are applied, the PS kinetic energy term contained in \mathcal{L}_A is no longer diagonal and a PS field redefinition has to be performed in order to restore the kinetic energy term to canonical form. The procedure is fully described in Section 4 of [25] and is valid unchanged in the present work; it is not repeated here.

In the BHLS model [25], after the X_V breaking, the vector meson mass term is no longer diagonal and writes ($m^2 = ag^2 f_\pi^2$) :

$$\mathcal{L}_V^{\text{mass}} = \frac{m^2}{2} \left[(1 + \Sigma_V)(\rho_I^2 + \omega_I^2) + 2\Delta_V \rho_I \cdot \omega_I + z_V \phi_I^2 + 2(1 + \Sigma_V)\rho^+ \rho^- \right], \quad (9)$$

discarding the unessential K^* sector and neglecting terms of degree greater than 1 in the breaking parameters. This mass term can be diagonalized by a 45° rotation, a quite unacceptable solution as it does not give a smooth limit in the symmetry limit $\Delta_V \rightarrow 0$. A smooth solution is obtained by the following transform to renormalized (R) fields :

$$\begin{pmatrix} \rho_I \\ \omega_I \end{pmatrix} = \begin{pmatrix} \rho_R \\ \omega_R \end{pmatrix} - \Delta_V \begin{pmatrix} h_V \omega_R \\ (1 - h_V) \rho_R \end{pmatrix}, \quad (10)$$

where h_V is a parameter submitted to fit, together with z_V , Σ_V and Δ_V . This solution, adopted in [25, 26, 27], provides a quite satisfactory description of the data. This transformation introduces a $\Delta_V \partial \rho_R \partial \omega_R$ term in the kinetic energy term of the vector mesons; this issue is known to imply the occurrence of wave-function renormalization factors absorbed in the effective couplings [38]; in the case of BHLS, they can be considered absorbed in the breaking parameters.

The full account of the BHLS model also requires the dynamical breaking [29, 25] generated by PS loop effects which also calls for an additional s -dependent renormalization step. It is rediscussed below within the context of the present work.

4 Breaking the HLS Lagrangian II : The Covariant Derivative (CD) Handle

As clear in Equations (8), BKY breaks the symmetry of the HLS Model in the very definition of its Lagrangian. This is quite legitimate and strongly validated by its remarkable description of a considerable amount of data [25, 26, 27]. Nevertheless, it is of interest to explore other possibilities to improve the description of the data in some specific mass regions and, then, reduce or cancel out the additional systematic uncertainties reported in [27].

Let us focus on Equation (4) which defines the original HLS covariant derivative :

$$D_\mu \xi_{R/L} = \partial_\mu \xi_{R/L} - ig V_\mu^I \xi_{R/L} + ie \xi_{R/L} A_\mu Q \quad .$$

The superscript I assigned to the vector field matrix V aims at reminding that the Isospin zero mesons are the so-called ideal combinations ω^I and ϕ^I . These naturally occur in the $U(3)$ symmetric expression of V .

The vector meson term in $D_\mu \xi_{R/L}$ can be written $gV^I = g \sum_{a=0,8} V_a T_a$ where the V_a 's are the vector meson fields and T_a , ($a = 1, \dots, 8$) are the Gell-Mann matrices normalized such that $\text{Tr}[T_a T_b] = \delta_{ab}/2$; T_0 is the unit matrix appropriately normalized : $T_0 = I/\sqrt{6}$. Thus, the (nonet) $U(3)_V$ symmetry of HLS is obtained by :

- Plugging the appropriately constructed V^I into the covariant derivative $D_\mu \xi_{R/L}$,
- Assuming the universality of the vector coupling g to the external world.

Therefore, we propose a direct breaking of the covariant derivative, a new tool independent of the BKY mechanism. Such a breaking mechanism is expressed by the modified covariant derivative :

$$D_\mu \xi_{R/L} = \partial_\mu \xi_{R/L} - ig \left[V_\mu^I + \delta V_\mu \right] \xi_{R/L} + ie \xi_{R/L} A_\mu Q, \quad (11)$$

where δV_μ can be chosen to break the $U(3)_V$ symmetry in a controlled way. For instance, breaking solely the nonet symmetry of V^I turns out to allow the coupling to the singlet V_μ^0 to differ from those of the octet fields, preserving in this way the $SU(3)_V$ symmetry. It will become clearer below why a more systematic approach must be preferred.

Identifying the field combinations associated with each of the canonical T_a matrices, one is led to define the following components which can participate to δV_μ separately or together :

$$\begin{cases} \delta V_\mu^0 = \frac{\xi_0}{\sqrt{2}} \left[\frac{\sqrt{2}\omega_\mu^I + \phi_\mu^I}{3} \right] \text{Diag}[1, 1, 1], \\ \delta V_\mu^8 = \frac{\xi_8}{\sqrt{2}} \left[\frac{\omega_\mu^I - \sqrt{2}\phi_\mu^I}{3\sqrt{2}} \right] \text{Diag}[1, 1, -2], \\ \delta V_\mu^3 = \frac{\xi_3}{\sqrt{2}} \left[\frac{\rho_\mu^0}{\sqrt{2}} \right] \text{Diag}[1, -1, 0], \end{cases} \quad (12)$$

in terms of the usual ideal field combinations.

The (free) breaking parameters ξ_0 , ξ_8 and ξ_3 are only requested to be real in order that δV_μ is hermitian as V_μ^I itself. Clearly, δV_μ^0 defines a breaking of the nonet symmetry down to $SU(3)_V \times U(1)_V$, δV_μ^8 rather expresses the breaking of the $SU(3)_V$ symmetry, while δV_μ^3 is related to a direct breaking of Isospin symmetry in the vector sector.

One could also introduce some breaking affecting the ρ^\pm entries of the V^I matrix³. The ρ^\pm entries are given by the sum of the Gell-Mann matrix terms T_1 and T_2 ; forcing a breaking for these entries requires two real parameters which should be equal ($\xi_{1,2}$) in order to preserve hermiticity.

So, ξ_3 and this $\xi_{1,2}$ could summarize the whole isospin breaking effects in the vector meson side; however, one can choose $\xi_{1,2} = 0$ as no theoretical value for the (unbroken) universal

³For the sake of simplicity, the case for the K^* sectors is left aside; substantially, this would introduce two additional real parameters $\xi_{4,5}$ and $\xi_{6,7}$ which may be fixed by the two radiative K^* decays; additional constraints may come from the τ decay to $K\pi\nu$.

coupling g is presently available. Indeed, all vector couplings in the HLS Lagrangian could then be reexpressed in terms of $g' = g(1 + \xi_{1,2})$; in this case, all physics quantities will depend on g' and $\xi'_i = \xi_i/(1 + \xi_{1,2})$ ($i = 0, 8, 3$) without any other occurrence of $\xi_{1,2}$ dependency.

Therefore, phenomenologically, the ξ_i 's and g itself are defined up to a normalization factor presently out of reach. This scaling property has obviously no consequence on physics observables like cross-sections or form factors.

So, from now on, one assumes the maximal breaking of $U(3)_V$ experimentally accessible : $\delta V_\mu = \delta V_\mu^0 + \delta V_\mu^8 + \delta V_\mu^3$. Compared with the original V^I entries, this turns out to modify only the diagonal entries of V^I by the following substitutions⁴ :

$$\begin{cases} \frac{\rho_I}{\sqrt{2}} \Rightarrow \frac{\rho_I}{\sqrt{2}}[1 + \xi_3], \\ \frac{\omega_I}{\sqrt{2}} \Rightarrow \frac{\omega_I}{\sqrt{2}} \left[1 + \frac{2\xi_0 + \xi_8}{3} \right] + \frac{[\xi_0 - \xi_8]}{3} \phi_I, \\ \phi_I \Rightarrow \phi_I \left[1 + \frac{\xi_0 + 2\xi_8}{3} \right] + \frac{\sqrt{2}[\xi_0 - \xi_8]}{3} \omega_I. \end{cases} \quad (13)$$

Then, the $U(3)_V$ breaking of the covariant derivative generates a breaking of the vector coupling universality. For this purpose, one should note that a vector mixing is generated, except if $\xi_0 = \xi_8$. For the sake of conciseness, this mechanism is referred to below as CD breaking.

5 BHLS₂ : A New Broken HLS Lagrangian

Here, we define a new version of the broken HLS Lagrangian, merging the two breaking schemes just presented – BKY and CD – as these two ways of breaking are conceptually independent. Their contributions are thus complementing each other. In order to fully take into account the electroweak sector, one should modify correspondingly the covariant derivative to :

$$\begin{cases} D_\mu \xi_L = \partial_\mu \xi_L - ig [V_\mu^I + \delta V_\mu] \xi_L + i \xi_L \mathcal{L}_\mu, \\ D_\mu \xi_R = \partial_\mu \xi_R - ig [V_\mu^I + \delta V_\mu] \xi_R + i \xi_R \mathcal{R}_\mu, \end{cases} \quad (14)$$

where, as usual[18] :

$$\mathcal{L}_\mu = eQA_\mu + \frac{g_2}{\sqrt{2}}(W_\mu^+ T_+ + W_\mu^- T_-) \quad \text{and} \quad \mathcal{R}_\mu = eQA_\mu, \quad (15)$$

discarding the Z^0 boson terms of no concern for the phenomenology we address. The T_\pm matrices are constructed out of the matrix elements V_{ud} and V_{us} of the Cabibbo-Kobayashi-Maskawa matrix and can be found in [18]. Finally, the weak coupling g_2 is related to the Fermi constant by $g_2 = 2m_W \sqrt{G_F \sqrt{2}}$.

The expression for the non-anomalous HLS Lagrangian pieces given in Section 2 remains formally valid, being understood that the covariant derivatives are modified according to Equations (14–15). As a result, the \mathcal{L}_V piece substantially differs from its partner in [25] while the \mathcal{L}_A piece in the present scheme is strictly identical to those given in [25]. The non-anomalous BHLS₂ Lagrangian is given expanded in Appendix A.

⁴ Remind that a $1/\sqrt{2}$ term is factored out in the definition of V^I .

6 The Order $\mathcal{O}(p^4)$ Terms of the HLS Lagrangian

Beside the \mathcal{L}_A and \mathcal{L}_V pieces which are $\mathcal{O}(p^2)$, the HLS approach also possesses terms of order $\mathcal{O}(p^4)$ (see Section 4.3 in [18]), which modify the $V - \gamma/W$ couplings in a specific way. As the role of such terms has never been really examined in phenomenology⁵, it looks worthwhile examining their relevance when dealing with data of high accuracy.

Using \mathcal{L}_μ and \mathcal{R}_μ just given, one first defines :

$$\begin{cases} \mathcal{L}_{\mu,\nu} = \partial_\mu \mathcal{L}_\nu - \partial_\nu \mathcal{L}_\mu - i [\mathcal{L}_\mu, \mathcal{L}_\nu] , \\ \mathcal{R}_{\mu,\nu} = \partial_\mu \mathcal{R}_\nu - \partial_\nu \mathcal{R}_\mu - i [\mathcal{R}_\mu, \mathcal{R}_\nu] , \end{cases} \quad (16)$$

and also :

$$\widehat{\mathcal{L}}_{\mu,\nu} = \xi_L \mathcal{L}_{\mu,\nu} \xi_L^\dagger , \quad \widehat{\mathcal{R}}_{\mu,\nu} = \xi_R \mathcal{R}_{\mu,\nu} \xi_R^\dagger , \quad (17)$$

where $\xi_R = \xi_L^\dagger = \exp[iP/f_\pi]$. Furthermore defining :

$$\widehat{\mathcal{V}}_{\mu,\nu} = \frac{1}{2} [\widehat{\mathcal{R}}_{\mu,\nu} + \widehat{\mathcal{L}}_{\mu,\nu}] , \quad \widehat{\mathcal{A}}_{\mu,\nu} = \frac{1}{2} [\widehat{\mathcal{R}}_{\mu,\nu} - \widehat{\mathcal{L}}_{\mu,\nu}] , \quad (18)$$

the $\mathcal{O}(p^4)$ Lagrangian writes [18] :

$$\mathcal{L}_z = z_1 \text{Tr} [\widehat{\mathcal{V}}_{\mu,\nu} \widehat{\mathcal{V}}^{\mu,\nu}] + z_2 \text{Tr} [\widehat{\mathcal{A}}_{\mu,\nu} \widehat{\mathcal{A}}^{\mu,\nu}] + z_3 \text{Tr} [\widehat{\mathcal{V}}_{\mu,\nu} V^{\mu,\nu}] , \quad (19)$$

where one has generically defined :

$$X_{\mu,\nu} = \partial_\mu X_\nu - \partial_\nu X_\mu - i [X_\mu, X_\nu] , \quad (20)$$

and where the z_i are constants not theoretically constrained. The z_3 term, the most involved in the phenomenology one addresses, writes :

$$\mathcal{L}_{z_3} = \frac{ge}{2} z_3 A_{\mu,\nu} \left[\rho_{\mu,\nu}^0 + \frac{1}{3} \omega_{\mu,\nu} - \frac{\sqrt{2}}{3} \phi_{\mu,\nu} \right] + \frac{gg_2}{4} z_3 [\overline{V}_{ud} W_{\mu,\nu}^- \rho_{\mu,\nu}^+ + V_{ud} W_{\mu,\nu}^+ \rho_{\mu,\nu}^-] \quad (21)$$

at lowest order in the expansion of the $\xi_{L/R}$ fields; here one has kept the unbroken V_μ matrix for clarity. By integrating by part and fixing the gauge condition to $\partial_\mu X^\mu = 0$ for all vector fields, this piece becomes :

$$\mathcal{L}_{z_3} = egz_3 s A_\mu \left[\rho_\mu^0 + \frac{1}{3} \omega_\mu - \frac{\sqrt{2}}{3} \phi_\mu \right] + \frac{g_2 g z_3 s}{2} [\overline{V}_{ud} \rho_\mu^+ W_\mu^- + V_{ud} \rho_\mu^- W_\mu^+] . \quad (22)$$

Thus, the \mathcal{L}_{z_3} piece exhibits s -dependent parts for the $V - \gamma$ and $V - W$ transition amplitudes which complement their constant parts provided by the usual $\mathcal{O}(p^2)$ HLS Lagrangian. The 'broken' version of Equation (22) is given in Appendix A.3.

⁵See, however, the discussion in [23] which is revisited here.

7 The Basic Solution (BS) and the Vector Mass Term

In the context where both the BKY and CD breaking mechanisms are at work, the vector mass term in \mathcal{L}_V becomes :

$$\mathcal{L}_{\text{mass}} = af_\pi^2 \text{Tr} \left[X_V (V_\mu^I + \delta V_\mu) \right]^2 . \quad (23)$$

Ignoring the K^* sector and setting $m^2 = ag^2 f_\pi^2$, it writes :

$$\begin{aligned} \mathcal{L}_{\text{mass}} = \frac{m^2}{2} & \left[(1 + \Sigma_V + 2\xi_3) [\rho_I^0]^2 + (1 + \Sigma_V + \frac{4}{3}\xi_0 + \frac{2}{3}\xi_8) [\omega_I]^2 + z_V (1 + \frac{2}{3}\xi_0 + \frac{4}{3}\xi_8) [\phi_I]^2 \right. \\ & \left. + 2\Delta_V \rho_I^0 \cdot \omega_I + \frac{2\sqrt{2}}{3} (1 + z_V) (\xi_0 - \xi_8) \omega_I \cdot \phi_I \right] + m^2 (1 + \Sigma_V) \rho^+ \cdot \rho^- . \end{aligned} \quad (24)$$

Therefore the CD breaking, via its δV_3 component, allows for a $\rho^0 - \rho^\pm$ (HK) mass difference, provided fits favor non-vanishing ξ_3 values. Moreover, all the components of δV defined above contribute to generate different HK masses for the ρ^0 and ω mesons as $\Delta m_{\rho^0-\omega}^2 = m^2 [\xi_3 - (2\xi_0 + \xi_8)/3]$. This contrasts with the previous BHLS model [25] where $m_{\rho^0}^2 = m_{\rho^\pm}^2 = m_\omega^2$ is fulfilled. Because of the non-vanishing HK mass difference between the ρ^0 and ω , one can already expect an improved treatment of the dipion threshold and spacelike regions in the BHLS₂ framework compared to BHLS.

Equation (24) is manifestly diagonalized by setting :

$$\Delta_V = 0 \quad , \quad \xi_0 = \xi_8 . \quad (25)$$

This solution – which lets z_V unconstrained– defines our Basic Solution (BS). Within the framework of this solution, the breaking parameters to be derived from fits are Σ_V , z_V , ξ_3 , ξ_0 ($= \xi_8$). Here one feels the issue with assuming solely nonet symmetry breaking; indeed, as this turns out to state $\xi_8 = 0$, the CD breaking implies $\xi_0 = 0$ and thus breaking HLS via the covariant derivative intrinsically implies that nonet symmetry cannot be solely broken.

At leading order in breaking parameters, the vector meson mass term in \mathcal{L}_V becomes diagonal and one has :

$$\left\{ \begin{array}{l} m_{\rho^\pm}^2 = m^2 (1 + \Sigma_V) , \\ m_{\rho^0}^2 = m^2 [1 + \Sigma_V + 2 \xi_3] , \\ m_\omega^2 = m^2 \left[1 + \Sigma_V + \frac{4}{3} \xi_0 + \frac{2}{3} \xi_8 \right] = m^2 [1 + \Sigma_V + 2 \xi_0] , \\ m_\phi^2 = m^2 z_V \left[1 + \frac{2}{3} \xi_0 + \frac{4}{3} \xi_8 \right] = m^2 z_V [1 + 2 \xi_0] . \end{array} \right. \quad (26)$$

So, BHLS₂ *a priori* yields different HK masses for all the vector mesons.

8 The Primordial Mixing (PM) and the Reference Solution (RS)

Another unused mechanism can be invoked; indeed, independently of the BKY and CD mechanisms just defined, one can always consider that the neutral vector fields ρ^0 , ω , ϕ involved in physical processes are not directly the ideal ones but combinations of these. For this purpose, let us define an infinitesimal rotation matrix $R(U_3) = \mathbf{1} + \mathcal{O}(\epsilon)$, which associates to the ideal field vector $\mathcal{V}_I = (\rho_I, \omega_I, \phi_I)$ a (first step) renormalized field vector $\mathcal{V}_R = (\rho_R, \omega_R, \phi_R)$ via :

$$\begin{pmatrix} \rho_I \\ \omega_I \\ \phi_I \end{pmatrix} = \begin{pmatrix} 1 & -\psi_\omega & \psi_\phi \\ \psi_\omega & 1 & \psi_0 \\ -\psi_\phi & -\psi_0 & 1 \end{pmatrix} \begin{pmatrix} \rho_R \\ \omega_R \\ \phi_R \end{pmatrix}, \text{ also denoted } \mathcal{V}_I = R(U_3) \cdot \mathcal{V}_R. \quad (27)$$

This is also a quite legitimate tool to extend the flexibility of BHLS₂.

The matrix $R(U_3)$ fulfills $R(U_3)\tilde{R}(U_3) = \tilde{R}(U_3)R(U_3) = \mathbf{1}$, up to terms of order $\mathcal{O}(\epsilon^2)$ which are discarded in our $\mathcal{O}(\epsilon)$ approach. As it is a rotation, this transformation preserves the canonical structure of the vector field kinetic term provided by the Yang-Mills Lagrangian (up to $\mathcal{O}(\epsilon^2)$ terms).

However, the (real) ψ (Euler) angles from transformation in Equation (27) should be chosen in such a way that $\mathcal{L}_{\text{mass}}(\mathcal{V}_I)$ remains canonical in the change of fields $\mathcal{V}_I \rightarrow \mathcal{V}_R$, *i.e.* the crossed terms in $\mathcal{L}_{\text{mass}}(\mathcal{V}_R)$ should be canceled out. Restarting from the mass term given by Equation (24), three conditions should be fulfilled :

$$\begin{cases} \rho_R - \omega_R = 0 \Rightarrow \Delta_V + \left[\frac{4}{3} \left\{ \xi_0 + \frac{1}{2}\xi_8 - \frac{3}{2}\xi_3 \right\} \psi_\omega \right] = 0, \\ \rho_R - \phi_R = 0 \Rightarrow [1 - z_V] \psi_\phi + \frac{\sqrt{2}}{3} \{1 + z_V\} (\xi_0 - \xi_8) + [\psi_\omega \psi_0] = 0, \\ \omega_R - \phi_R = 0 \Rightarrow 3[1 - z_V] \psi_0 + [1 + z_V]\sqrt{2} (\xi_0 - \xi_8) - 3[\psi_\omega \psi_\phi] = 0. \end{cases} \quad (28)$$

The last bracketed terms in these expressions can be discarded as clearly of second order in the breaking parameters $\{\xi_i, \psi_j\}$; this already implies that $\Delta_V = 0$ and that ψ_ω becomes unconstrained.

As for the parameter z_V – generated by the BKY breaking in its $s\bar{s}$ entry – the situation deserves further comments :

- **Either** z_V is found such that⁶ $1 - z_V \simeq \mathcal{O}(\epsilon)$, then none of the ψ angles is constrained at order $\mathcal{O}(\epsilon)$ and, moreover, the last two Equations (28) then imposes $\xi_0 = \xi_8$.
- **Or** z_V is returned by fits such that $1 - z_V$ is not $\mathcal{O}(\epsilon)$. Then, at first order in breakings, the last two equations imply $\psi_\phi = \psi_0$ and that they are proportional to $\xi_0 - \xi_8$.

⁶ One may think that a reference magnitude for any generic ϵ is $\mathcal{O}(\epsilon) \simeq e = \sqrt{4\pi\alpha_{\text{em}}} \simeq 0.3$.

Preliminary fits, performed using this mechanism – named from now on Primordial Mixing (PM) – indicate that $1 - z_V$ is in the range $(1 \div 2)\epsilon$ and thus, in this case also $\xi_0 = \xi_8$ can be imposed. Therefore, besides the Basic Solution (BS), one gets an additional one, we name it Reference Solution (RS), which also includes the Primordial Mixing (PM). Also considering the former BHLS model [25, 26, 27], one thus has at disposal three different models. This allows for a better insight into the systematics and model dependence effects.

9 Vector Meson Propagators and Form Factors

Let us anticipate on form factor calculations using the Lagrangian given in Appendix A and have a look at the form factor values at $s = 0$ – before introducing mixing effects due to loop corrections. For this purpose, let us start with a preliminary digression on vector meson propagators, especially those for the ω and ϕ mesons, as these play an important role at the chiral point and in the physics of the (close) spacelike region which is also addressed in the present work.

For the ρ meson, following the pioneering work [39], the inverse propagator at one loop can be written (also see [23, 24, 25]) :

$$D_\rho(s) = s - m_\rho^2 - \Pi(s) ,$$

where the self-energy $\Pi(s)$ is the sum of the loops allowed by the non-anomalous Effective Lagrangian given in Appendix A; in our context, these are essentially pion and kaon loops⁷. $\Pi(s)$ is a real analytic function ($\Pi(s^*) = [\Pi(s)]^*$) which vanishes at $s = 0$ because of current conservation, and is real for negative s – in fact, this property holds already below $m_{\pi^0}^2$, the lowest energy hadronic threshold. Hence, this implies that $D_\rho(0) = -m_\rho^2$, where m_ρ^2 is displayed in Equations (26).

In principle, this also applies to the ω and ϕ propagators; however, taking into account their narrow character, it looks unmotivated to enter into such complications when fitting objects like e^+e^- annihilation cross sections. In this case, phenomenology has lengthily experienced a broad success using Breit-Wigner (BW) lineshapes. However, as discussed in [25], some physics quantities like the contribution of the $e^+e^- \rightarrow \pi^+\pi^-$ cross-section to the estimate for the muon HVP, may require some care about the behavior of approximations close to the chiral point, as this region gives an enhanced contribution to the muon HVP. For this purpose, [25] proposed the following modified BW lineshape for the ω and ϕ mesons :

$$D_V(s) = s - m_V^2 - \frac{s}{m_V^2} \left[\widetilde{m}_V^2 - m_V^2 - i\widetilde{m}_V\widetilde{\Gamma}_V \right] , \quad (29)$$

where $(\widetilde{m}_V, \widetilde{\Gamma}_V)$ are parameters to be fitted and the m_V^2 's are the relevant HK square masses as displayed in Equations (26). Numerically, this expression for the $D_V(s)$'s is close to usual BW lineshapes⁸. This BW-like parametrization imposes the ω and ϕ meson inverse propagators to

⁷ Loops generated by the anomalous HLS Lagrangian pieces [18, 22] also contribute but can be discarded [25] as reminded in the next Section; however, some anomalous loops, suppressed by a factor of e^2 , can have to be kept as they may play some role in specific expressions as will be emphasized below.

⁸ Setting $\widetilde{m}_V = m_V$ in this approximation gives $D_V(s) = s - m_V^2 + is\widetilde{\Gamma}_V/m_V$; more common choices for the imaginary part here are $m_V\widetilde{\Gamma}_V$ or $\sqrt{s}\widetilde{\Gamma}_V$, quite analogous to our own choice.

fulfill $D_V(0) = -m_V^2$ as already does the ρ meson inverse propagator; this property of the propagators at $s = 0$ is essential to recover the expected values for the pion and kaon form factors at the origin within the HLS framework.

On the other hand, if one wishes to examine the analytic continuation of the ω and ϕ propagators somewhat inside the spacelike region, it might be desirable to make it real there; this can be achieved by simply replacing $\tilde{\Gamma}_V$ in Equation (29) by $\theta(s)\tilde{\Gamma}_V$ – or rather, $\theta(s - m_{\pi^0}^2)\tilde{\Gamma}_V$.

Using the Basic Solution (BS) or the Reference Solution (RS) to redefine the physical vector meson fields, one can show, using the Lagrangian given in the Appendix A, that :

$$F_\pi(0) = 1 \quad , \quad F_{K^\pm}(0) = 1 \quad , \quad F_{K^0}(0) = 0 \quad , \quad (30)$$

up to terms of order $\mathcal{O}(\epsilon^2)$. One can check that the conditions $\Delta_V = 0$ and $\xi_0 = \xi_8$ are essential in the derivation of these constraints.

So, the breaking parameters to be derived from fits are Σ_V , ξ_3 , $\xi_0 (= \xi_8)$ and z_V when working within the BS framework; one should also include the ψ rotation angles when extending BHLS₂ to the Reference Solution.

It is worthwhile reminding that the effects of δV_μ^0 and δV_μ^8 are intimately intricated within our new Lagrangian frameworks. Here, indeed, a breaking of solely nonet symmetry (*i.e.* $\xi_0 \neq 0$) cannot occur if not accompanied by a breaking of the $SU(3)_V$ symmetry of the same intensity.

In conclusion, the present model (BHLS₂) is not a trivial variant of BHLS [25]. Some important properties of BHLS₂ versus BHLS mentioned below, will further substantiate this statement.

10 Dynamical Mixing of Vector Mesons

10.1 The Squared Mass Matrix at One Loop ...

As previously noted [29, 25] and reminded above, all variants of the HLS Model, including BHLS₂ (see Appendix A.1), exhibit $\rho^0/\omega/\phi \rightarrow K\bar{K}$ couplings. This implies that, at one loop, the squared mass matrix of the $\rho^0/\omega/\phi$ system receives non-diagonal entries, *i.e.* the vector fields occurring in the Lagrangian Eq (116) are no longer mass eigenstates. Mass eigenstates are constructed using perturbative methods as performed in [29, 25]. As the loops are (real analytic) functions of s , the mass eigenstates become also s -dependent. Within the BHLS and BHLS₂ frameworks, the kaon loops produce a s -dependent difference between the $\rho^\pm - W^\pm$ and $\rho^0 - \gamma$ transition amplitudes which has provided the first solution [29, 25] to the long standing e^+e^- versus τ puzzle [40, 41, 42]. Nevertheless, in another Effective Lagrangian context, this s -dependent difference can be successfully generated by other means [43].

Basically, the Dynamical (or Loop) Mixing of Vector Mesons has been first defined⁹ and motivated in [29]. In order to ease the reading, we remind it and emphasize the new features provided by the BHLS₂ context.

⁹See also [25].

The (squared) mass matrix of the $\rho^0/\omega/\phi$ sector can be written :

$$M^2(s) = M_0^2(s) + \delta M^2(s) , \quad (31)$$

where :

$$M_0^2(s) = \text{Diag}(m_{\rho^0}^2 + \Pi_{\pi\pi}(s), m_\omega^2, m_\phi^2) . \quad (32)$$

The Higgs-Kibble masses m_V are displayed in Equations (26), and $\Pi_{\pi\pi}(s)$ is the pion loop weighted by the square of the $\rho^0\pi^+\pi^-$ coupling constant. Because all the loop functions are real analytic function of s , $M_0^2(s)$, $\delta M^2(s)$, and hence $M^2(s)$, are hermitian analytic matrices (e.g. fulfilling $[X(s)]^\dagger = X(s^*)$).

In order to construct explicitly $\delta M^2(s)$, it is worth reexpressing some VPP coupling constants in a suitable manner. One can write :

$$\left\{ \begin{array}{l} g_{K^+K^-}^\rho = \tilde{G}(1 - \frac{\Delta_A}{2}) \bar{g}_\rho^\pm , \quad g_{K^+K^-}^\omega = \tilde{G}(1 - \frac{\Delta_A}{2}) \bar{g}_\omega^\pm , \quad g_{K^+K^-}^\phi = \tilde{G}(1 - \frac{\Delta_A}{2}) \bar{g}_\phi^\pm , \\ g_{K^0\bar{K}^0}^\rho = \tilde{G}(1 + \frac{\Delta_A}{2}) \bar{g}_\rho^0 , \quad g_{K^0\bar{K}^0}^\omega = \tilde{G}(1 + \frac{\Delta_A}{2}) \bar{g}_\omega^0 , \quad g_{K^0\bar{K}^0}^\phi = \tilde{G}(1 + \frac{\Delta_A}{2}) \bar{g}_\phi^0 , \end{array} \right. \quad (33)$$

having defined $\tilde{G} = ag/(4z_A)$. Using Equations (25), common to both the BS and RS variants, one finds :

$$\left\{ \begin{array}{l} \bar{g}_\rho^\pm = \{1 + \Sigma_V + \xi_3 + \psi_\omega + \sqrt{2}z_V\psi_\phi\} , \\ \bar{g}_\omega^\pm = \{1 + \Sigma_V + \xi_8 - \psi_\omega + \sqrt{2}z_V\psi_0\} , \\ \bar{g}_\phi^\pm = \{-\sqrt{2}z_V(1 + \xi_8) + \psi_\phi + \psi_0\} , \end{array} \right. \quad (34)$$

and :

$$\left\{ \begin{array}{l} \bar{g}_\rho^0 = \{1 + \Sigma_V + \xi_3 - \psi_\omega - \sqrt{2}z_V\psi_\phi\} , \\ \bar{g}_\omega^0 = -\{1 + \Sigma_V + \xi_8 + \psi_\omega + \sqrt{2}z_V\psi_0\} , \\ \bar{g}_\phi^0 = \{\sqrt{2}z_V(1 + \xi_8) + \psi_\phi - \psi_0\} . \end{array} \right. \quad (35)$$

When dealing specifically with the BS variant, these two sets of equations are used by simply dropping out the ψ_α parameters.

Denoting by resp. $\Pi_\pm(s)$ and $\Pi_0(s)$ the *amputated* charged and neutral kaon loops, the $\mathcal{V}_R^i \rightarrow \mathcal{V}_R^j$ transition amplitudes ($i, j = \rho^0, \omega, \phi$) are given by :

$$\varepsilon_{i,j}(s) = g_{K^+K^-}^i g_{K^+K^-}^j \Pi_\pm(s) + g_{K^0\bar{K}^0}^i g_{K^0\bar{K}^0}^j \Pi_0(s) \quad (36)$$

using the notations just defined. Then, the elements of the $\delta M^2(s)$ matrix are :

$$\delta M_{i,j}^2(s) = \varepsilon_{i,j}(s) . \quad (37)$$

As in the former BHLS [25], $\delta M^2(s)$ is non-diagonal for non-zero values of s . Therefore, at one-loop order, the field combinations defined in both the BS and RS variants are not mass eigenstates, as in the previous BHLS release. This calls for a mass-dependent diagonalization which is reminded in the next Subsection.

Let us make a few more remarks about the non-diagonal entries of δM^2 . In the no breaking limit, where the neutral and charged kaon loops coincide, the $\rho^0 - \omega$ and $\rho^0 - \phi$ entries identically vanish; however, the $\omega - \phi$ entry, proportional to the sum of the neutral and charged kaon loops, does not vanish, indicating that the $\omega - \phi$ mixing is always at work at one loop order within the HLS framework.

In the former BHLS, however, if no breaking is applied in the \mathcal{L}_A sector and if there is no mass breaking among the kaons, there was no $\rho^0 - \omega$ and $\rho^0 - \phi$ transitions. This remains true within the BS framework defined above. However, within the RS framework, the ψ_α 's come in such a way that none of the entries of $\delta M^2(s)$ vanishes.

10.2 ...And its Diagonalization

The diagonalization of $\mathcal{L}_{\text{mass}}$ at one loop order is performed by means of another (s -dependent) rotation matrix to a second step of vector field renormalization $R \Rightarrow R'$:

$$\begin{pmatrix} \rho_R \\ \omega_R \\ \phi_R \end{pmatrix} = \begin{pmatrix} 1 & -\alpha(s) & \beta(s) \\ \alpha(s) & 1 & \gamma(s) \\ -\beta(s) & -\gamma(s) & 1 \end{pmatrix} \begin{pmatrix} \rho_{R'} \\ \omega_{R'} \\ \phi_{R'} \end{pmatrix}, \text{ also denoted } \mathcal{V}_R = R(\text{Loop}) \cdot \mathcal{V}_{R'} \quad (38)$$

so that the full renormalization procedure is obtained by :

$$\mathcal{V}_I \Rightarrow [R(U_3) \cdot R(\text{Loop})] \cdot \mathcal{V}_{R'}. \quad (39)$$

The R' fields are the physical vector meson fields. When working within the Basic Solution variant, $\mathcal{V}_R \equiv \mathcal{V}_I$ and $R(U_3)$ can be dropped out from Equation (39); otherwise, within the RS framework, $R(U_3)$ is given in Equation (27).

The complex "angles" in Equation (38) can be derived from the $\delta M^2(s)$ matrix elements :

$$\alpha(s) = \frac{\varepsilon_{\rho^0\omega}(s)}{\lambda_\rho(s) - \lambda_\omega(s)}, \quad \beta(s) = -\frac{\varepsilon_{\rho^0\phi}(s)}{\lambda_\rho(s) - \lambda_\phi(s)}, \quad \gamma(s) = -\frac{\varepsilon_{\omega\phi}(s)}{\lambda_\omega(s) - \lambda_\phi(s)}, \quad (40)$$

where the numerators manifestly depend on the kaon loops only and the λ 's are the eigenvalues of $M^2(s)$ matrix. At leading order in breaking parameters, these write [25] :

$$\lambda_\rho(s) = m_{\rho^0}^2 + \Pi_{\pi\pi}(s) + \varepsilon_{\rho^0\rho^0}(s), \quad \lambda_\omega(s) = m_\omega^2 + \varepsilon_{\omega\omega}(s), \quad \lambda_\phi(s) = m_\phi^2 + \varepsilon_{\phi\phi}(s), \quad (41)$$

the vector meson masses being those displayed in Equations (26). As the three m_V^2 's occurring here are different, the three angles defined above vanish at $s = 0$; in contrast, within the former BHLS context [25], because the HK masses for ρ^0 and ω were equal, $\alpha(0)$ has a non-zero limit at $s = 0$, compromising a proper analytic continuation of the form factors downwards into the spacelike region¹⁰.

In summary the full transform from ideal to fully renormalized ρ_0, ω, ϕ fields is given either by (BS solution) :

$$R(I \Rightarrow R') \equiv R(\text{Loop}) \quad (42)$$

¹⁰See, in particular, the comments in Section 6.3 of [25].

or by (RS solution) :

$$R(I \Rightarrow R') \equiv [R(U_3) \cdot R(Loop)] = \begin{pmatrix} 1 & -[\psi_\omega + \alpha(s)] & [\psi_\phi + \beta(s)] \\ [\psi_\omega + \alpha(s)] & 1 & [\psi_0 + \gamma(s)] \\ -[\psi_\phi + \beta(s)] & -[\psi_0 + \gamma(s)] & 1 \end{pmatrix}, \quad (43)$$

where breaking terms of order greater than 1 have been discarded. We will refer from now on to Equation (43) for both the BS and RS variants, being understood that in the former case, the ψ_i 's are zero. When relevant, the entries in the matrix just above will be denoted $\tilde{\alpha}(s)$, $\tilde{\beta}(s)$ and $\tilde{\gamma}(s)$, using obvious notations. Moreover, in the following, the fully renormalized fields can be either indexed by R' – if useful – or deprived of indexation to lighten expressions. For clarity, in all displayed Lagrangian pieces, one always writes the couplings for the *ideal* ρ_0 , ω , ϕ fields. To go to physical fields, one has to apply the appropriate transformation $R(I \Rightarrow R')$ and collects the contributions in order to yield the *physical* ρ_0 , ω , ϕ couplings.

10.3 The Effects of Anomalous Loops

When defining the loops contributing to $\delta M^2(s)$, we have only considered those generated by the non-anomalous HLS Lagrangian. However, the anomalous (FKTUY) HLS Lagrangian pieces [22, 18] allow for (anomalous) couplings also generating loop contributions¹¹ to $\delta M^2(s)$ as, for instance, $K^*\bar{K}$ or 3-pion loops. As all the two particle channels have thresholds above our fitting region, their loops – of order $\mathcal{O}(g^2)$ – are real in our fitting range and, thus, can be discarded, assuming their effects numerically absorbed by the subtraction polynomials of the other (pion and kaon) loops involved [25].

However, one should also note that the anomalous (FKTUY) sector of the HLS Lagrangian generates couplings of the neutral vector mesons to the $\pi^0\gamma$, $\eta\gamma$ and $\eta'\gamma$ final states, even when setting $c_3 = c_4$ [25, 27]. Then the FKTUY sector generates the corresponding loops, which have couplings of order $\mathcal{O}(g^2e^2)$ and develop tiny imaginary parts far inside our fitting region for the first two and close to its upper border for the third one. These contributions, and their imaginary parts, are higher order and can generally be discarded; nevertheless, their tiny imaginary parts were accounted for in our previous studies [25, 26, 27] by simply adding some fixed $i\epsilon$ to the eigenvalue differences $\lambda_i(s) - \lambda_j(s)$ which occur in the denominators of the mixing "angles" shown in Equations (40).

So, these (complex) mixing "angles" exhibit a dependence upon differences of the $M^2(s)$ eigenvalues. However, these eigenvalues – see Equations (41) – being s -dependent, their differences may exhibit zeros for real values of s which, accordingly, generate real poles for the mixing "angles". Poles occurring at real negative s are not a real issue as they can be dropped out by means of customary dispersive techniques. For the others, the $i\epsilon$ trick emphasized just above, permits to avoid unwanted singularities on the physical region $s \geq m_{\pi^0}$.

¹¹The Yang-Mills part of the full Lagrangian may also contribute with other loops like $K^*\bar{K}^*$. The $VPPP$ Lagrangian generate 2-loop contributions with coefficients of $\mathcal{O}(\epsilon)$ or $\mathcal{O}(\epsilon^2)$ to the transitions among the vector mesons; they are presently ignored.

In the previous BHLS version[25], the main purpose of this *ad hoc* $i\varepsilon$ was to force¹² $\alpha(s = 0) = 0$, which is no longer necessary in the present version of BHLS. A more natural way to proceed – giving the same results – is, however, to take into account the $\pi^0\gamma$ loop which introduces a small imaginary part to the eigenvalue differences, for $s_0 \geq m_{\pi^0}^2$ upwards. For this purpose, we use the loop expression derived in [44] (see its Appendix C) which can be written ($s_0 = m_{\pi^0}^2$) :

$$\epsilon_{\pi^0}^V(s) = \frac{[g_{V\pi^0\gamma}^R]^2}{96\pi^2} [G(s) - s_0^2] \equiv [g_{V\pi^0\gamma}^R]^2 \epsilon_{\pi^0}(s) . \quad (44)$$

Along the real axis in the complex s -plane, one has :

$$\begin{cases} G(s) = -\frac{(s_0 - s)^3}{s} \ln \frac{(s_0 - s)}{s_0} , & s \leq s_0 \\ G(s) = \frac{(s - s_0)^3}{s} \left[\ln \frac{(s - s_0)}{s_0} - i\pi \right] , & s \geq s_0 . \end{cases} \quad (45)$$

The derivation of the $g_{V\pi^0\gamma}^R$ couplings is given in Subsection 12.2. The constant term inside the bracket in Equation (44) ensures that $\epsilon_{\pi^0}(0) = 0$. Full consistency would impose to add (using obvious notations) :

$$\delta_2 M_{i,j}^2(s) = [g_{V_i\pi^0\gamma}^R g_{V_j\pi^0\gamma}^R] \epsilon_{\pi^0}(s) + [g_{V_i\eta\gamma}^R g_{V_j\eta\gamma}^R] \epsilon_{\eta}(s) + [g_{V_i\eta'\gamma}^R g_{V_j\eta'\gamma}^R] \epsilon_{\eta'}(s) \quad (46)$$

¹²As clear from the first Equations (40), the numerator of $\alpha(s)$ behaves as s close to the origin and, as $m_{\rho^0} = m_{\omega}$ in the previous BHLS [25], $\lambda_{\rho}(s) - \lambda_{\omega}(s)$ exhibits a similar s -behavior.

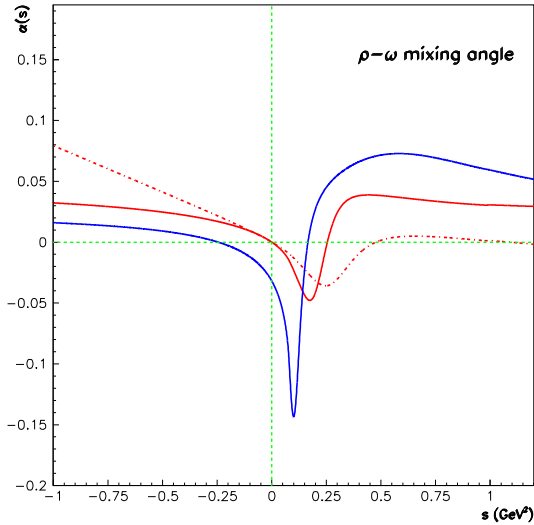


Figure 1: Real part of the $\alpha(s)$ mixing "angle"; the full blue curve shows the case for the (former) BHLS, the full red curve refers to the Reference Solution of BHLS₂ and the dashed red curve to its Basic Solution. See Subsection 10.3 for more comments.

to $\delta M^2(s)$ as expressed above; however, because of the e^2 factor, they are higher order and can be neglected, except in the diagonal where they avoid possible real poles in the physical region. Additionally, the $\epsilon_\eta(s)$ and $\epsilon_{\eta'}(s)$ contributions displayed for completeness will also be discarded.

In order to substantiate the effect of the $\pi^0\gamma$ loops, let us anticipate on the global fit information. The main effect of these loops is to prevent naturally the occurrence of poles on the physical region. This effect is prominent for the "angle" $\alpha(s)$ which produces a $\rho^0 - \omega$ mixing; Figure 1 displays the behavior of $\text{Re}[\alpha(s)]$ for the BHLS₂ BS and RS variants and also, for comparison, its behavior within the former BHLS, where a $i\epsilon$ trick prevents a real pole close to the 2-pion threshold [25]. Even if the overall lineshapes are similar, one observes significant differences between the various solutions; for instance, $\alpha(s)$ vanishes at $s = 0$ within the two variants of BHLS2, as the denominator is non-zero at the chiral point, allowing for a smooth connection between the spacelike and timelike regions.

Over the range $[-3.5 \div 1.2] \text{ GeV}^2$, the behavior observed for the two other mixing angles $\beta(s)$ and $\gamma(s)$ is much smoother (see also [23]); nevertheless, specific parametrizations may lead to a real pole¹³ for $\beta(s)$ at negative s below $\simeq -1.5 \text{ GeV}^2$. As noted above, such poles can be eliminated by means of usual dispersive methods.

11 The Model Pion and Kaon Form Factors

Using the non-anomalous sectors of the HLS model, broken as pointed out in the previous Sections (see Appendix A), one can already derive some of the form factors expressions needed for our global fit framework.

11.1 The Pion Form Factor in the τ Decay

The τ sector of BHLS₂ is almost identical to that of BHLS [25]; indeed the main \mathcal{L}_τ piece reminded in Appendix A.2 is unchanged, but the newly introduced \mathcal{L}_{z_3} contributes. This yields :

$$F_\pi^\tau(s) = \left[1 - \frac{a}{2}(1 + \Sigma_V) \right] - \frac{ag}{2}(1 + \Sigma_V)F_\rho^\tau(s) \frac{1}{D_\rho(s)}, \quad (47)$$

with :

$$\begin{cases} D_\rho(s) = s - m_\rho^2 - \Pi_{\rho\rho}^\tau(s), \\ F_\rho^\tau(s) = f_\rho^\tau - gz_3s - \Pi_W(s), \\ f_\rho^\tau = agf_\pi^2(1 + \Sigma_V) \quad , \quad m_\rho^2 = ag^2f_\pi^2(1 + \Sigma_V), \end{cases} \quad (48)$$

where z_3 is a new HLS parameter [18] introduced by the $\mathcal{O}(p^4)$ terms of the HLS Lagrangian (see Appendix A.3). $\Pi_{\rho\rho}^\tau(s)$ is the loop correction to the ρ^\pm propagator and $\Pi_W(s)$ the loop correction to the $W^\pm - \rho^\pm$ transition amplitude; both are defined just below.

Using the following short-hand notations :

$$G_\pi = \frac{ag}{2} \quad , \quad G_K = \frac{ag}{4z_A}, \quad (49)$$

¹³One should note that a pole at such a location is exhibited by the usual Gounaris-Sakurai formula [45].

one first defines the pion and kaon loop contributions to the ρ^\pm self-energy $\Pi_{\rho\rho}^\tau(s)$:

$$\Pi_\pi^\tau(s) = [\ell_\pi^\tau(s) + P_\pi^\tau(s)] \quad , \quad \Pi_K^\tau(s) = [\ell_K^\tau(s) + P_K^\tau(s)] \quad , \quad (50)$$

where $\ell_\pi^\tau(s)$ and $\ell_K^\tau(s)$ denote the amputated loop functions for resp. $\pi^\pm\pi^0$ and $K^\pm K^0$, each having absorbed *only* a factor of resp. G_π^2 and G_K^2 ; in this way, only the breaking parameters affecting the V sector of BHLS₂ are factored out and displayed. $P_\pi^\tau(s)$ and $P_K^\tau(s)$ are subtraction polynomials chosen to vanish at $s = 0$ because of current conservation. Then one has¹⁴ :

$$\begin{cases} \Pi_{\rho\rho}^\tau(s) = [(1 + \Sigma_V)]^2 \Pi_\pi^\tau(s) + [\sqrt{2}(1 + \Sigma_V)]^2 \Pi_K^\tau(s) , \\ \Pi_W(s) = \frac{(1 + \Sigma_V)}{G_\pi} \left[1 - \frac{a}{2}(1 + \Sigma_V) \right] \Pi_\pi^\tau(s) + \frac{\sqrt{2}(1 + \Sigma_V)}{z_A G_K} \left[z_A - \frac{a}{2}(1 + \Sigma_V) \right] \Pi_K^\tau(s) . \end{cases} \quad (51)$$

As the loop functions vanish at $s = 0$, one clearly has $F_\pi^\tau(0) = 1$. One should note that the same subtraction polynomials occur in the $W - \rho$ transition amplitude $F_\rho^\tau(s)$ and in the inverse propagator $D_\rho(s)$ but differently weighted.

The expression for the loop functions $\ell_\pi^\tau(s)$ and $\ell_K^\tau(s)$ along the real s -axis can be found in Subsection F.2 of the Appendix to [29]; the subtraction polynomial needed to ensure that they vanish at $s = 0$ has coefficients given in Equations (122) of this reference. The coefficients for the constant term and for the second degree one given therein are correct, but the coefficient for the term linear in s should be corrected to :

$$c_1 = \frac{1}{\pi} \left[1 - \frac{m_0^2 + m_c^2}{2m_0 m_c} \ln \frac{m_0 - m_c}{m_0 + m_c} \right]$$

using the notations¹⁵ of [29].

11.2 Parametrization of Loops in e^+e^- Annihilations and τ Decays

The ρ^0 self-energy and the $\gamma \Rightarrow (\rho^0/\omega/\phi)$ transition amplitudes involve important loop corrections; these already play a central role in the dynamical mixing of vector mesons as shown in Section 10. Let us define a parametrization common to the computation of the "angles" $\alpha(s)$, $\beta(s)$ and $\gamma(s)$, to the self-energies and to the $A \Rightarrow V$ transition amplitudes as these are involved in all form factors addressed in our global fitting code.

One first defines the following loops :

$$\Pi_\pi^e(s) = [\ell_\pi^e(s) + P_\pi^e(s)] \quad , \quad \Pi_{K^\pm}^e(s) = [\ell_{K^\pm}^e(s) + P_{K^\pm}^e(s)] \quad , \quad \Pi_{K^0}^e(s) = [\ell_{K^0}^e(s) + P_{K^0}^e(s)] \quad , \quad (52)$$

where $\ell_\pi^e(s)$, $\ell_{K^\pm}^e(s)$ and $\ell_{K^0}^e(s)$ are resp. the $\pi^+\pi^-$, K^+K^- and $K^0\bar{K}^0$ loops. These are defined as the amputated loops, including only a factor of G_π^2 for the former loop and of G_K^2 for the two others (see Equations (49)). The expression for these loops along the real s -axis can be found in Section F.1 of the Appendix to [29].

¹⁴Here and in the following, one can be led to keep breaking parameter dependencies higher than first order to simplify the expression writing.

¹⁵ m_0^2 and m_c^2 are the s values of the direct and crossed thresholds energies.

The loop parts being defined this way, $P_\pi^e(s)$, $P_{K^\pm}^e(s)$ and $P_{K^0}^e(s)$ are the subtraction polynomials, chosen of the second degree and vanishing at $s = 0$.

However, as already observed in Section 10, besides the pion loop, it is rather the sum and difference of the kaon loops which are relevant :

$$\begin{cases} \Pi_{K_{\text{sum}}}^e(s) = [\ell_{K^\pm}^e(s) + \ell_{K^0}^e(s) + P_S^e(s)] \equiv \Pi_S^e(s), \\ \Pi_{K_{\text{diff}}}^e(s) = [\ell_{K^\pm}^e(s) - \ell_{K^0}^e(s) + P_D^e(s)] \equiv \Pi_D^e(s), \end{cases} \quad (53)$$

where $P_S^e(s)$ and $P_D^e(s)$ are denoting their respective subtraction polynomials. As already noted, one can consider $\Pi_{K_{\text{diff}}}^e(s)$ and $P_D^e(s)$ to be first order in breaking ($\mathcal{O}(\epsilon)$). So, it is certainly more appropriate to parametrize $P_S^e(s)$ and $P_D^e(s)$ for fits and propagate them into the subtraction polynomials of $\Pi_{K^\pm}^e(s)$ and $\Pi_{K^0}^e(s)$ by stating :

$$P_{K^\pm}^e(s) = \frac{1}{2} [P_S^e(s) + P_D^e(s)] \quad , \quad P_{K^0}^e(s) = \frac{1}{2} [P_S^e(s) - P_D^e(s)] \quad , \quad (54)$$

keeping in mind that $P_D^e(s)$ is $\mathcal{O}(\epsilon)$, while $P_S^e(s)$ is $\mathcal{O}(1)$.

On the other hand, as one certainly has :

$$\begin{cases} \Pi_\pi^\tau(s) \simeq \Pi_\pi^e(s) + \mathcal{O}(\epsilon), \\ \Pi_K^\tau(s) \simeq \Pi_{K_{\text{sum}}}^e(s) + \mathcal{O}(\epsilon), \end{cases} \quad (55)$$

and it is appropriate to impose :

$$\begin{cases} P_\pi^\tau(s) = P_\pi^e(s) + \delta P^\tau(s), \\ P_K^\tau(s) = P_S^e(s), \end{cases} \quad (56)$$

and submit to fit the coefficients of the $\delta P^\tau(s)$ polynomial rather than those for $P_\pi^\tau(s)$ directly. This turns out to attribute the full breaking in e^+e^- versus τ to the pion loop subtraction term; as our fitting region is mostly below the $K\bar{K}$ thresholds, this looks a safe assumption. The second relation, additionally, is an assumption which allows to reduce the number of free parameters in the minimization procedure by two units without any degradation of the fit quality.

As a general statement, all our subtraction polynomials have been chosen of second degree and vanishing at $s = 0$. An exception is made, however, by choosing the third degree for $\delta P^\tau(s)$ which is found to provide a significantly better description of the τ spectra, especially for the Belle dipion spectrum [46].

11.3 The Pion Form Factor in the e^+e^- Annihilations

Because of the vector meson mixing, deriving the pion form factor in the e^+e^- annihilation is slightly more involved than in the τ decay. To start, one needs to propagate the transformation in Equation (43) into the Lagrangian in Appendix A.1 and collect all contributions to the fully

renormalized ρ , ω and ϕ field couplings. The derived pion form factor in e^+e^- annihilations $F_\pi^e(s)$ writes :

$$F_\pi^e(s) = \left[1 - \frac{a}{2}(1 + \Sigma_V)\right] - F_{\rho\gamma}^e(s) \frac{g_{\rho\pi\pi}}{D_\rho(s)} - F_{\omega\gamma}^e(s) \frac{g_{\omega\pi\pi}}{D_\omega(s)} - F_{\phi\gamma}^e(s) \frac{g_{\phi\pi\pi}}{D_\phi(s)}. \quad (57)$$

Using the $\rho^I \pi^+ \pi^-$ coupling in the Lagrangian displayed in Appendix A.1 and the $I \Rightarrow R$ transform given by Equation (43), one readily gets :

$$g_{\rho\pi\pi} = \frac{ag}{2}(1 + \Sigma_V + \xi_3), \quad g_{\omega\pi\pi} = -\frac{ag}{2}[\psi_\omega + \alpha(s)], \quad g_{\phi\pi\pi} = \frac{ag}{2}[\psi_\phi + \beta(s)], \quad (58)$$

keeping only the leading $\mathcal{O}(\epsilon)$ terms in breaking. So, BHLS₂ generates ω and ϕ direct couplings to $\pi\pi$. The inverse ρ^0 propagator writes :

$$D_{\rho^0}(s) = s - m_{\rho^0}^2 - \Pi_{\rho\rho}^e(s), \quad (59)$$

where $m_{\rho^0}^2$ is defined in Equations (26) and $\Pi_{\rho\rho}^e(s)$ is the self-energy of the physical (*i.e.* fully renormalized) ρ^0 . This can be defined in terms of the loop functions constructed in the Subsection just above. $\Pi_{\rho\rho}^e(s)$ is made up of two pieces :

$$\begin{cases} \Pi_\pi^e(s) = [\tilde{g}_\pi^\rho]^2 [\ell_\pi^e(s) + P_\pi^e(s)] & , \quad \tilde{g}_\pi^\rho = (1 + \Sigma_V + \xi_3), \\ \Pi_K^e(s) = [\tilde{g}_{K\pm}^\rho]^2 \ell_{K\pm}^e(s) + [\tilde{g}_{K0}^\rho]^2 \ell_{K0}^e(s) + \frac{1}{2} \left[[\tilde{g}_{K\pm}^\rho]^2 + [\tilde{g}_{K0}^\rho]^2 \right] P_S^e(s) + \mathcal{O}(\epsilon^2), \end{cases} \quad (60)$$

where the couplings $\tilde{g}_{K\pm}^\rho$ and \tilde{g}_{K0}^ρ are given in Appendix A.4. A term $\left[[\tilde{g}_{K\pm}^\rho]^2 - [\tilde{g}_{K0}^\rho]^2 \right] P_D^e(s)/2$ has been omitted in the expression for $\Pi_K^e(s)$ as being $\mathcal{O}(\epsilon^2)$.

As for the inverse propagators $D_\omega(s)$ and $D_\phi(s)$, one uses the expression given by Equation (29) with the appropriate values for HK masses m_V^2 , and having $([\tilde{m}_V, \tilde{\Gamma}_V], V = \omega, \phi)$ as parameters to be determined by fit.

The loop corrected $V - \gamma$ transitions amplitudes $F_{V\gamma}^e(s)$ are given by :

$$F_{V\gamma}^e(s) = f_{V\gamma} - c_{V\gamma} z_3 s - \Pi_{V\gamma}(s), \quad (V = \rho_R^0, \omega_R, \phi_R), \quad (61)$$

where the new-comer $z_3 s$ terms occur as in $F_\rho^\tau(s)$ above. Using together the ideal couplings Equations (A.3), the renormalization matrix Equation (43) and the RS conditions (see Section 8), one derives :

$$\begin{cases} f_{\rho\gamma} = agf_\pi^2 \left[1 + \Sigma_V + \xi_3 + \frac{[\psi_\omega + \alpha(s)]}{3} + z_V \frac{\sqrt{2}[\psi_\phi + \beta(s)]}{3} \right], \\ f_{\omega\gamma} = \frac{agf_\pi^2}{3} \left[1 + \Sigma_V + \xi_8 - 3[\psi_\omega + \alpha(s)] + z_V \sqrt{2}[\psi_0 + \gamma(s)] \right], \\ f_{\phi\gamma} = \frac{agf_\pi^2}{3} \left[-z_V \sqrt{2}(1 + \xi_8) + 3[\psi_\phi + \beta(s)] + [\psi_0 + \gamma(s)] \right], \end{cases} \quad (62)$$

which become s -dependent thanks to the dynamical vector mixing. Similarly, using the couplings which can be read off \mathcal{L}_{z_3} in Equation (119) and the transformation matrix given by Equation (43), one also derives :

$$\begin{cases} c_{\rho\gamma} = g \left[1 + \xi_3 + \frac{[\psi_\omega + \alpha(s)]}{3} + \frac{\sqrt{2}[\psi_\phi + \beta(s)]}{3} \right], \\ c_{\omega\gamma} = \frac{g}{3} \left[1 + \xi_8 - 3[\psi_\omega + \alpha(s)] + \sqrt{2}[\psi_0 + \gamma(s)] \right], \\ c_{\phi\gamma} = \frac{g}{3} \left[-\sqrt{2}(1 + \xi_8) + 3[\psi_\phi + \beta(s)] + [\psi_0 + \gamma(s)] \right], \end{cases} \quad (63)$$

neglecting terms of breaking order greater than 1. Finally, the relevant loop transition terms $\Pi_{V\gamma}(s)$ are collected in Appendix A.5.

11.4 The Charged and Neutral Kaon Form Factors

The charged and neutral kaon electromagnetic form-factors can also be derived from the BHLS₂ Lagrangian given in Appendix A.1 :

$$\begin{aligned} F_{K_c}^e(s) &= \left[1 - \frac{a}{6z_A}(3 + 2\Sigma_V - \frac{3\Delta_A}{2}) \right] \\ &\quad - F_{\rho\gamma}(s) \frac{g_{\rho K^+ K^-}}{D_\rho(s)} - F_{\omega\gamma}(s) \frac{g_{\omega K^+ K^-}}{D_\omega(s)} - F_{\phi\gamma}(s) \frac{g_{\phi K^+ K^-}}{D_\phi(s)}, \\ F_{K_0}^e(s) &= -\frac{a\Sigma_V}{6z_A} - F_{\rho\gamma}(s) \frac{g_{\rho K^0 \bar{K}^0}}{D_\rho(s)} - F_{\omega\gamma}(s) \frac{g_{\omega K^0 \bar{K}^0}}{D_\omega(s)} - F_{\phi\gamma}(s) \frac{g_{\phi K^0 \bar{K}^0}}{D_\phi(s)}, \end{aligned} \quad (64)$$

where the $\gamma - V$ transition amplitudes $F_{V\gamma}$ and the propagators have been already defined and the $V K \bar{K}$ couplings are displayed in the Appendix A.4.

The experimental spectra measured in the spacelike region, in particular by the NA7 Collaboration [47, 48], being squared form factors, the modulus squared of the form factors given in Equation (57) and in Equations (64) apply directly. In the timelike region, experimentalists rather publish cross-sections :

$$\sigma(e^+e^- \rightarrow P\bar{P}) = \frac{8\pi\alpha_{\text{em}}^2}{3s^{5/2}} q_P^3 |F_P^e(s)|^2, \quad (65)$$

where $q_P = \sqrt{s - 4m_P^2}/2$ is the meson momentum in the center-of-mass system ($P = K^+, K^0$). In the case of the $K^+ K^-$ final state, the cross-section should take into account the significant interaction between the charged kaons emerging from the e^+e^- annihilation. Traditionally, this is done by multiplying the $e^+e^- \rightarrow K^+ K^-$ cross-section by the leading term describing the Coulomb interaction as formulated by [49, 50] :

$$Z(s) = \left[1 + \pi\alpha_{\text{em}} \frac{1 + v^2}{2v} \right], \quad v = \frac{\sqrt{s - 4m_{K^\pm}^2}}{s}. \quad (66)$$

As the data have become more and more precise, it looks more convenient to use the exponentiated expression derived in [51] which includes also the Final State Radiation (FSR) correction factor; indeed, the $K^+ K^-$ spectra provided by the various experiments are not amputated from FSR effects.

11.5 Form Factors in BHLS versus BHLS₂

It looks worth pointing out the difference between the form factor expressions in BHLS and in BHLS₂. As already noted, the \mathcal{L}_A Lagrangian is common to both frameworks. In contrast, the \mathcal{L}_V Lagrangian is significantly different. Obvious differences for \mathcal{L}_V have already been noted. For instance, within BHLS₂, $\Delta_V = 0$ and its sharing parameter h_V drop out whereas they are a key ingredient in the diagonalization procedure of BHLS.

Three parameters¹⁶ arise from the Covariant Derivative breaking (ξ_3, ξ_0, ξ_8). Moreover, a key role is played by the ψ rotation angles within the RS solution of BHLS₂. None of these parameters occur in the BHLS framework of [25].

The effect of a significant ξ_3 value is obviously equivalent to shifting apart the Higgs-Kibble masses of both ρ 's and their couplings to $\pi\pi$ in a correlated way. As this kind of exercise performed within BHLS concluded to a small effect [25, 26], one expects a small value for ξ_3 . Also, BHLS₂ deals with different subtraction polynomials – the $\delta P^\tau(s)$ function already referred to above – for the $\pi^\pm\pi^0$ and $\pi^+\pi^-$ loops, a new (loop) mechanism able alone to contribute to physical mass and width differences between the ρ^0 and ρ^\pm mesons.

One should also note another difference : In the present framework, as already noted in Subsection 11.1, the pion and kaon loops entering the amplitudes $F_\rho^\tau(s)$ and $F_\rho^e(s)$ carry fitted subtraction polynomials already involved in the charged and neutral ρ inverse propagators $D_\rho(s)$. In BHLS, one allowed the subtraction polynomial in $F_\rho^{e/\tau}(s)$ to carry a piece independent of both $D_\rho(s)$'s. Because of the $\mathcal{O}(p^4)$ term still introduced, it means that a second-degree term in s has been removed from $F_\rho^{e/\tau}(s)$ in the BHLS₂ framework. We should see below the effect of this on the $\pi\pi$ P -wave phase-shift above the ϕ mass.

12 The Anomalous Sector of BHLS₂

As in [25], the anomalous FKTUY Lagrangian [22, 18] is used to address the $e^+e^- \rightarrow (\pi^0/\eta)\gamma$ and $e^+e^- \rightarrow \pi^0\pi^+\pi^-$ processes, and also the radiative decays with couplings of the form $VP\gamma$ and $P\gamma\gamma$ which are parts of our global fitting framework. One can display its various pieces :

$$\begin{aligned} \mathcal{L}_{\text{anomalous}} &= (1 - c_4) \mathcal{L}_{AAP} + c_3 \mathcal{L}_{VVP} + \left[1 - \frac{3}{4}(c_1 - c_2 + c_4)\right] \mathcal{L}_{APPP} \\ &+ (c_1 - c_2 - c_3) \mathcal{L}_{VPPP} + (c_4 - c_3) \mathcal{L}_{AVP}, \end{aligned} \quad (67)$$

where, temporarily, the weight of each piece has been extracted out to exhibit its dependence upon the unconstrained c_i constants of the anomalous HLS Lagrangian [22]. If one imposes to yield the Wess-Zumino-Witten terms [52, 53] at the chiral point – the so-called triangle and box anomalies – the condition $c_3 = c_4$ is known to be mandatory [21, 18]. Reference [25] having also shown that this condition is indeed favored by fits to the annihilation data, one endorses the $c_3 = c_4$ constraint and, thus, cancels out the last term in Equation (67). Hence, the $VP\gamma$ couplings become entirely generated by the combination of VVP couplings with the $V - \gamma$ transitions provided by the non-anomalous HLS Lagrangian.

¹⁶Additional constraints arising in the diagonalization procedure of the vector mass term, have reduced this number to two as $\xi_0 = \xi_8$ is requested.

The surviving Lagrangian pieces displayed in Equation (67) are given by :

$$\left\{ \begin{array}{l} \mathcal{L}_{VVP} = -\frac{N_c g^2}{4\pi^2 f_\pi} c_3 \epsilon^{\mu\nu\alpha\beta} \text{Tr}[\partial_\mu V_\nu \partial_\alpha V_\beta P] , \\ \mathcal{L}_{AAP} = -\frac{N_c e^2}{4\pi^2 f_\pi} (1 - c_4) \epsilon^{\mu\nu\alpha\beta} \partial_\mu A_\nu \partial_\alpha A_\beta \text{Tr}[Q^2 P] , \\ \mathcal{L}_{VPPP} = -i \frac{N_c g}{4\pi^2 f_\pi^3} (c_1 - c_2 - c_3) \epsilon^{\mu\nu\alpha\beta} \text{Tr}[V_\mu \partial_\nu P \partial_\alpha P \partial_\beta P] , \\ \mathcal{L}_{APPP} = -i \frac{N_c e}{3\pi^2 f_\pi^3} [1 - \frac{3}{4}(c_1 - c_2 + c_4)] \epsilon^{\mu\nu\alpha\beta} A_\mu \text{Tr}[Q \partial_\nu P \partial_\alpha P \partial_\beta P] , \end{array} \right. \quad (68)$$

where N_c is the number of colors and the c_i factors have been reabsorbed in the normalization of the various Lagrangian pieces. P and V denote the *bare* pseudoscalar and vector field matrices. In the present context, one has, however :

$$V_\mu = V_\mu^I + \delta V_\mu , \quad (69)$$

where V_μ^I is the (usual) $U(3)$ symmetric vector field matrix and $\delta V_\mu = \delta V_\mu^3 + \delta V_\mu^0 + \delta V_\mu^8$ which has been expressed in term of the ideal field combinations in Equations (12).

For the reader's convenience, Appendix B reminds briefly the renormalization procedure which leads from the bare PS fields to their renormalized partners [25].

12.1 Renormalization of the VVP Couplings

As displayed in Equation (39), referring to :

$$\tilde{\mathcal{V}} = (\rho_0, \omega, \phi) ,$$

the relation between the fully renormalized vector fields (denoted R here and from now on) and their ideal combination is given by :

$$\mathcal{V}^I \Rightarrow [R(U_3) \cdot R(Loop)] \cdot \mathcal{V}^R ,$$

where the product $R(U_3) \cdot R(Loop)$, given by Equation (43), will be denoted from now on :

$$\mathcal{R}(s) = R(U_3) \cdot R(Loop) . \quad (70)$$

Let us point out that $\mathcal{R}(s)$ is a real analytic 3×3 matrix function and fulfills at order $\mathcal{O}(\epsilon)$:

$$\widetilde{\mathcal{R}}(s + i\epsilon) \cdot \mathcal{R}(s + i\epsilon) = \mathcal{R}(s + i\epsilon) \cdot \widetilde{\mathcal{R}}(s + i\epsilon) = 1 \quad (71)$$

along the right-hand cut on the physical sheet [29]. The VVP Lagrangian displayed in Appendix C can be symbolically written :

$$\mathcal{L}_{VVP}^{\text{ideal}}(P) = \frac{C}{2} \epsilon^{\mu\nu\alpha\beta} \left\{ P_0 \partial_\mu \mathcal{V}_{i\nu}^I G_{i,j}^I(P_0) \partial_\alpha \mathcal{V}_j^I + G_i^I(\pi^\pm) [\pi^- \partial_\mu \rho_\nu^+ \partial_\alpha \mathcal{V}_{i\beta}^I + \pi^+ \partial_\mu \rho_\nu^- \partial_\alpha \mathcal{V}_{i\beta}^I] \right\} , \quad (72)$$

in terms of ideal field combinations, P_0 being any of the π^0 , η or η' fields; summation over greek and latin indices is understood. The 3-vector $G^I(\pi^\pm)$ and the 3×3 matrix $G^I(P_0)$ can easily be constructed using the relevant pieces of information given in Appendix C. One thus has :

$$\widetilde{G}^I(\pi^\pm) = (\widetilde{g}_{\rho^0 \rho^\pm}^\pm, \widetilde{g}_{\omega \rho^\pm}^\pm, \widetilde{g}_{\phi \rho^\pm}^\pm) , \quad (73)$$

with the obvious (ρ, ω, ϕ) component indexing. On the other hand, one has defined :

$$G^I(P_0) = \begin{pmatrix} \widetilde{g}_{\rho\rho} & \frac{1}{2}\widetilde{g}_{\rho\omega} & \frac{1}{2}\widetilde{g}_{\rho\phi} \\ \frac{1}{2}\widetilde{g}_{\omega\rho} & \widetilde{g}_{\omega\omega} & \frac{1}{2}\widetilde{g}_{\omega\phi} \\ \frac{1}{2}\widetilde{g}_{\phi\rho} & \frac{1}{2}\widetilde{g}_{\phi\omega} & \widetilde{g}_{\phi\phi} \end{pmatrix} , \quad (74)$$

where, for each P_0 , \widetilde{g}_{ij} is the coupling of the form $P_0 \mathcal{V}_i \mathcal{V}_j$ which can be read off the relevant expressions given in Appendix C.

Performing the replacement $\mathcal{V}^I = \mathcal{R}(s) \mathcal{V}^R$ in Equation (72), one can derive the fully renormalized VVP Lagrangian :

$$\begin{aligned} \mathcal{L}_{VVP}^{\text{ren}}(P) = & \frac{C}{2} \epsilon^{\mu\nu\alpha\beta} \left[P_0 \partial_\mu \mathcal{V}_{i\nu}^R G_{i,j}^R(P_0) \partial_\alpha \mathcal{V}_{j\beta}^R \right. \\ & \left. + \pi^- \partial_\mu \rho_\nu^+ G_i^R(\pi^\pm) \partial_\alpha \mathcal{V}_{i\beta}^R + \pi^+ \partial_\mu \rho_\nu^- G_i^R(\pi^\pm) \partial_\alpha \mathcal{V}_{i\beta}^R \right] , \end{aligned} \quad (75)$$

where, the coupling vector $G^R(\pi^\pm)$ and the coupling matrix $G^R(P_0)$ inherit from \mathcal{R} a s -dependence; they are related to their ideal partners by :

$$G^R(\pi^\pm) = \widetilde{\mathcal{R}}(s) \widetilde{G}^I(\pi^\pm) , \quad G^R(P_0) = \widetilde{\mathcal{R}}(s) G^I(P_0) \mathcal{R}(s) , \quad (76)$$

which is a concise way to express the renormalized couplings.

12.2 The Renormalized AVP Effective Lagrangian

As already noted, setting $c_3 = c_4$ turns out to cancel the direct FKTUY AVP Lagrangian piece; hence, all AVP couplings inside BHLS₂ are generated by VVP couplings followed by one $V \rightarrow \gamma$ transition. Let us consider the $V - \gamma$ transition term of the non-anomalous BHLS₂ Lagrangian (see Equation (116)). Having defined the transposed vector $\widetilde{f}_{V\gamma}^I = (f_{\rho\gamma}^I, f_{\omega\gamma}^I, f_{\phi\gamma}^I)$, one can rewrite it :

$$\mathcal{L}_{AV} = -e \left[\widetilde{f}_{V\gamma}^I \cdot \mathcal{V}_\mu^I \right] A^\mu = -e \left[\widetilde{f}_{V\gamma}^R(s) \cdot \mathcal{V}_\mu^R \right] A^\mu , \quad (77)$$

which defines the 3-vector $f_{V\gamma}^R$ as :

$$f_{V\gamma}^R = \widetilde{\mathcal{R}}(s) f_{V\gamma}^I . \quad (78)$$

The effective \mathcal{L}_{AVP} Lagrangian can be derived from Equation (75) by replacing one neutral vector meson, say \mathcal{V}_i^R , using the rule :

$$\mathcal{V}_{i\mu}^R \Rightarrow (-ie f_{\gamma\mathcal{V}_i}^R) \left(\frac{-i}{D_{\mathcal{V}_i}(0)} \right) A_\mu = \frac{e f_{\gamma\mathcal{V}_i}^R}{m_i^2} A_\mu \equiv e H_{i\gamma} A_\mu, \quad (i = \rho^0, \omega, \phi) \quad (79)$$

where m_i^2 is the renormalized squared mass of the \mathcal{V}_i vector meson as given in Equations (26); let us note that each $H_{i\gamma}$ carries a hidden factor of $1/g$. Starting with the charged pion part of Equation (75), one gets :

$$\mathcal{L}_{AVP}^{\text{ren}}(\pi^\pm) = \frac{eC}{2} [G^R(\pi^\pm) \cdot H_{\gamma V}] \epsilon^{\mu\nu\alpha\beta} \partial_\mu A_\nu [\partial_\alpha \rho_\beta^+ \pi^- + \partial_\alpha \rho_\beta^- \pi^+] , \quad (80)$$

where $H_{\gamma V}$ is the 3-vector constructed from the $H_{i\gamma}$ defined just above :

$$\widetilde{H}_{\gamma V} = \left(\frac{f_{\gamma\rho^0}^R}{m_{\rho^0}^2}, \frac{f_{\gamma\omega}^R}{m_\omega^2}, \frac{f_{\gamma\phi}^R}{m_\phi^2} \right) . \quad (81)$$

For the P_0 part of the Lagrangian Equation (75), the algebra is slightly more involved and gives :

$$\mathcal{L}_{AVP}^{\text{ren}}(P_0) = eC \sum_{i=\rho,\omega,\phi} [\widetilde{H}_{\gamma V} G^R(P_0)]_i \epsilon^{\mu\nu\alpha\beta} \partial_\mu V_{i\nu}^R \partial_\alpha A_\beta P_0, \quad P_0 = (\pi^0, \eta, \eta'), \quad (82)$$

with :

$$C = -\frac{N_c g^2}{4\pi^2 f_\pi} c_3 . \quad (83)$$

This effective Lagrangian is the tool to parametrize the $e^+e^- \rightarrow (\pi^0/\eta)\gamma$ cross-sections and the $VP\gamma$ radiative decays.

12.3 The $e^+e^- \rightarrow (\pi^0/\eta)\gamma$ Cross-Sections

Using the AAP and AVP Lagrangians derived above in terms of renormalized vector and pseudoscalar fields, one can construct the amplitudes for $\gamma^* \rightarrow (\pi^0/\eta)\gamma$ transitions. These can be written :

$$T(\gamma^* \rightarrow P_0\gamma) = -i \frac{3\alpha_{\text{em}}}{\pi f_\pi} \left[g^2 c_3 \widetilde{H}_{\gamma V} G^R(P_0) K_{\gamma V} - (1 - c_3) L_{P_0} \right] = -i \frac{3\alpha_{\text{em}}}{\pi f_\pi} F_{P_0\gamma}(s), \quad (84)$$

where the (co)vector $\widetilde{H}_{\gamma V}$ is defined in Equation (81), the $G^R(P_0)$ matrix in Equation (76) (and Equation (74)). One has also defined :

$$\widetilde{K}_{\gamma V} = \left(\frac{F_{\gamma\rho^0}^R(s)}{D_{\rho^0}(s)}, \frac{F_{\gamma\omega}^R(s)}{D_\omega(s)}, \frac{F_{\gamma\phi}^R(s)}{D_\phi(s)} \right), \quad (85)$$

the functions $F_{\gamma V}^R(s)$ and $D_V(s)$ having been defined in Subsection 11.3. Finally, one has :

$$L_{\pi^0} = \frac{g_{\pi^0\gamma\gamma}}{3}, \quad \text{and} \quad L_\eta = \frac{g_{\eta\gamma\gamma}}{\sqrt{3}}, \quad (86)$$

with $g_{P_0\gamma\gamma}$, derived in [25], and reminded in Appendix D.

In the case of the $e^+e^- \rightarrow (\pi^0/\eta)\gamma$ annihilations, the available data are always cross-sections which are related to $F_{P_0\gamma}(s)$ just defined by :

$$\sigma(e^+e^- \rightarrow P_0\gamma, s) = \frac{3\alpha_{\text{em}}^3}{8\pi f_\pi^2} \left[\frac{s - m_{P_0}^2}{s} \right]^3 |F_{P_0\gamma}(s)|^2 . \quad (87)$$

12.4 The $e^+e^- \rightarrow \pi^0\pi^+\pi^-$ Cross-section

The amplitude for the $\gamma^* \rightarrow \pi^0\pi^+\pi^-$ transition involves most of the FKTUY Lagrangian pieces; it can be written :

$$T(\gamma^* \rightarrow \pi^0\pi^+\pi^-) = T_{APPP} + T_{VPPP} + T_{VVP} , \quad (88)$$

labeling each term by the particular piece of the FKTUY Lagrangian from which it originates. As already noted, because $c_3 = c_4$ is assumed, there is no T_{AVP} piece.

The T_{APPP} contribution to the full $T(\gamma^* \rightarrow \pi^0\pi^+\pi^-)$ amplitude can be derived from the information given in Appendix D; it writes :

$$T_{APPP} = C_{APPP} [1 - G(\delta_P)] \epsilon_{\mu\nu\alpha\beta} \epsilon_\mu(\gamma) p_0^\nu p_-^\alpha p_+^\beta , \quad (89)$$

where one has defined :

$$G(\delta_P) = \frac{\Delta_A}{2} + \epsilon_1 \sin \delta_P - \epsilon_2 \cos \delta_P , \quad C_{APPP} = -\frac{ie}{4\pi^2 f_\pi^3} \left[1 - \frac{3}{4}(c_1 - c_2 + c_4) \right] . \quad (90)$$

Three pieces are coming from the $VPPP$ Lagrangian also displayed in Appendix E; they are collected in :

$$T_{VPPP} = C_{VPPP} \left[\sum_{V=\rho,\omega,\phi} \frac{F_{V\gamma}^e(s)}{D_V(s)} g_{V\pi}^R(s) \right] \epsilon_{\mu\nu\alpha\beta} \epsilon_\mu(\gamma) p_0^\nu p_-^\alpha p_+^\beta , \quad (91)$$

where the renormalized vector couplings $g_{V\pi}^R(s)$ to 3 pions have to be derived from using Equations (149) and Equation (152), $\mathcal{R}(s)$ being given by Equation (43). The $V-\gamma$ amplitudes $F_{V\gamma}^e(s)$ have been constructed in Subsection 11.3 and the inverse propagators in Subsection 11.3 for the ρ^0 meson. The inverse propagators for the ω and ϕ mesons have been discussed and defined in Section 7. One has also defined :

$$C_{VPPP} = -\frac{3ige}{4\pi^2 f_\pi^3} [c_1 - c_2 - c_3] . \quad (92)$$

The VVP Lagrangian piece in Equation (140) has been rewritten in terms of renormalized fields in Equation (75) with (renormalized) couplings derivable by means of Equation (76). The simplest way to write down $T(\gamma^* \rightarrow \pi^0\pi^+\pi^-)$ in a way easy to code within our global fit procedure is displayed just below.

One first defines the $H_i(s)$ functions :

$$\begin{cases} H_0(s) = 1 , & H_1(s) = \frac{1}{D_\rho(s_{+-})} + \frac{1}{D_\rho(s_{0+})} + \frac{1}{D_\rho(s_{0-})} , \\ H_2(s) = \frac{1}{D_\rho(s_{+-})} , & H_3(s) = \tilde{\alpha}(s_{+-}) \left[\frac{1}{D_\rho(s_{+-})} - \frac{1}{D_\omega(s_{+-})} \right] , \end{cases} \quad (93)$$

where s is the incoming squared energy and the s_{ij} 's indicate the invariant mass squared of the corresponding outgoing (i, j) pairs; the primed mixing angles have been defined in Subsection

10.2. T_{VVP} depends on the 3 functions ($H_i(s)$, $i = 1 \dots 3$ with s -dependent coefficients $F_i(s)$ given below.

Collecting all terms, the full amplitude writes :

$$T(\gamma^* \rightarrow \pi^0 \pi^+ \pi^-) = \left[F_0(s) H_0(s) + C_{VVP} \sum_{i=1 \dots 3} F_i(s) H_i(s) \right] \epsilon_{\mu\nu\alpha\beta} \epsilon_\mu(\gamma) p_0^\nu p_-^\alpha p_+^\beta, \quad (94)$$

with :

$$C_{VVP} = -i \frac{3egm^2}{8\pi^2 f_\pi^3} (1 + \Sigma_V) c_3. \quad (95)$$

In this way, to write down the full amplitude, the various $F_i(s)$ functions only depend on the incoming off-shell photon energy squared s ; the dependence upon the various sub-energies s_{ij} is, instead, only carried by the $H_i(s)$ functions as clear from Equations (93). One has :

$$\left\{ \begin{array}{l} F_0(s) = C_{APPP} [1 - G(\delta_P)] + C_{VPPP} \left[\frac{F_{\rho\gamma}^R(s)}{D_\rho(s)} g_{\rho\pi}^0(s) + \frac{F_{\omega\gamma}^R(s)}{D_\omega(s)} g_{\omega\pi}^0(s) + \frac{F_{\phi\gamma}^R(s)}{D_\phi(s)} g_{\phi\pi}^0(s) \right], \\ F_1(s) = \tilde{\alpha}(s) \frac{F_{\rho\gamma}^R(s)}{D_\rho(s)} + \left[1 + \frac{2\xi_0 + \xi_8}{3} \right] \frac{F_{\omega\gamma}^R(s)}{D_\omega(s)} + \left[\frac{\sqrt{2}}{3} (\xi_0 - \xi_8) + \tilde{\gamma}(s) \right] \frac{F_{\phi\gamma}^R(s)}{D_\phi(s)}, \\ F_2(s) = \left[\epsilon_2 \cos \delta_P - \epsilon_1 \sin \delta_P - \frac{\Delta_A}{2} \right] \frac{F_{\rho\gamma}^R(s)}{D_\rho(s)} + \frac{3\xi_3}{2} \frac{F_{\omega\gamma}^R(s)}{D_\omega(s)}, \\ F_3(s) = \frac{F_{\rho\gamma}^R(s)}{D_\rho(s)}. \end{array} \right. \quad (96)$$

where $\tilde{\alpha}(s) = \alpha(s) + \psi_\omega$ and $\tilde{\gamma}(s) = \gamma(s) + \psi_0$.

One should note, as in BHLS [25] and earlier in [23], that all parameters already fitted with the (five) $e^+e^- \rightarrow (\pi\pi/K\bar{K}/\pi^0\gamma/\eta\gamma)$ processes fully determine all the ($F_i(s)$, $i = 1 \dots 3$). The only new parameter coming with $e^+e^- \rightarrow \pi^0\pi^+\pi^-$ is $c_1 - c_2$, only affecting $F_0(s)$; for practical purposes, it is handled in a specific manner, as in the previous versions of the (broken) HLS model just quoted.

Indeed, a global fit to all cross-sections but $e^+e^- \rightarrow \pi^0\pi^+\pi^-$ allows to yield the relevant parameters with a good approximation; thus, having at hand all ingredients defining the $F_i(s)$'s, a first minimization run including the $e^+e^- \rightarrow \pi^0\pi^+\pi^-$ cross-section can be performed to also derive a first estimate for $c_1 - c_2$. The output of this MINUIT minimization run is then used as input for a next minimization step. This initiates an iteration procedure involving all cross-sections which is carried on up to convergence – when some criterion is met.

This method has been proven to converge in a very few minimization steps [25]. What makes such a minimization procedure unavoidable is that the $e^+e^- \rightarrow \pi^0\pi^+\pi^-$ cross-section expression implies to integrate over the s_{ij} 's at each step. This is obviously prohibitively computer time consuming for a negligible gain. Hence, at each step, one starts by tabulating coef-

ficient functions, exhibited in the next expression between curly brackets :

$$\begin{aligned} \sigma(e^+e^- \rightarrow \pi^0\pi^+\pi^-, s) = & \frac{\alpha_{\text{em}} s^2}{192\pi^2} \times \left[\left\{ \int G dx dy \right\} |F_0(s)|^2 \right. \\ & + C_{VVP}^2 \sum_{i,j=1\dots 3} F_i(s) F_j^*(s) \left\{ \int G H_i H_j^* dx dy \right\} \\ & \left. + C_{VVP} \sum_{i=1\dots 3} \left(F_0(s) F_i^*(s) \left\{ \int G H_i^* dx dy \right\} + F_0^*(s) F_i(s) \left\{ \int G H_i dx dy \right\} \right) \right] \end{aligned} \quad (97)$$

and these tables are used all along this step. Equation (97) uses the Kuraev-Silagadze parametrization [54] and its kernel $G(x, y)$ function; these are reminded in Appendix H of [25].

13 The Data Samples Submitted to Global Fits

Basically, 48 experimental data samples are presently available which enter the scope of the HLS Model. Relying on the global fits performed in [25, 26], one has been led to discard a few of them from our fitting procedure; this situation happens again within the present framework. Before going on, let us remind the most important part of the data samples and list the newcomers. Newcomers encompass either newly collected samples or existing form factor spectra covering spacelike momenta not treated within the former BHLS framework [25].

Substantially, the set of available data samples includes :

- *i/ For the $\pi^+\pi^-$ annihilation channel :*

The earliest data samples date back to the beginning of the eighties [55, 56]. These have been followed by quite precise data samples collected in scan mode by CMD-2 [57, 58, 59] and SND [60] on the VEPP-2M collider at Novosibirsk. The published spectra cover the energy region from 370 MeV to 970 MeV; presently, there is still no published spectrum covering the $\phi(1020)$ energy region.

These measurements, referred to globally as NSK, have been followed by large statistics data collected using the so-called initial state radiation (ISR) mechanism (see [61], for instance). In this way, three data samples [62, 63, 64] have been collected with the KLOE detector running on the DAPHNE collider up to $\simeq 1$ GeV, just below the ϕ meson mass. In the same period of time, another $\pi^+\pi^-$ sample has been collected by BaBar [65, 66] covering the energy range up to 3 GeV. By 2015, BESIII has also published a $\pi^+\pi^-$ sample [67] and, by end of 2017, a group from the CLEO-c Collaboration has published the latest to date $\pi^+\pi^-$ sample [68] collected with the CESR detector.

As a whole, the most precise data samples represent now 8 spectra. One has been led to discard from our global framework KLOE08 [62] and BaBar [65, 66] for different reasons¹⁷ discussed in [26, 27]. A reanalysis unifying the three KLOE data samples has been recently performed [70, 71] and an 85 data-point spectrum has been derived which will be commented at the appropriate place. Moreover, the full error covariance matrix

¹⁷As for the BaBar spectrum, a recent comprehensive study [69] analyzing the $\omega \rightarrow \pi^+\pi^-$ branching ratio reaches conclusions similar to ours. One also has to keep in mind that the BaBar $\pi\pi$ spectrum is in conflict with the τ data corrected for the isospin breakings. This is what we learn from Figure 1 of Ref. [27].

including the correlations between KLOE08, KLOE10 and KLOE12 is now available; this is used here to account for the (weak) correlations between KLOE10 and KLOE12.

- **ii/ For the K^+K^- annihilation channel :**

Up to very recently, the available data samples covering this channel were the three scans collected by CMD-2 [72, 73] and the two scans of SND [74]. They were included within the global fits performed in the (previous) BHLS framework (see [25, 27]). Quite recently, the CMD-3 Collaboration has found that the two CMD-2 scans [73] should undergo a rescaling by [75] 1.094 ± 0.04 which represents an important correction of the spectrum absolute normalization and of its (correlated) systematics ($2.2\% \rightarrow 4.45\%$). The influence of this correction on the physics information previously derived within BHLS in [25, 26, 27] imposes the quite significant update performed in the present study.

BaBar has published in 2013 the first measurement [76] of this cross-section performed in the ISR mode. This high statistics spectrum covers the full energy range from threshold to 3 GeV. Moreover, very recently, CMD-3 has also produced a new high statistics measurement of this spectrum in scan mode [77]. However, as emphasized in the CMD-3 publication, this measurement is inconsistent with the BaBar data sample [76]. This issue is addressed below.

- **iii/ For the $K_L K_S$ annihilation channel :**

To our knowledge, the first reported measurement of the $e^+e^- \rightarrow K_L K_S$ cross section has been provided by CMD-2 in 1995 [72] and has been followed in 2004 by the 4 scans reported in [78]. In the meantime SND also produced 4 data samples, 2 in the charged decay mode of the K_S meson, 2 in its neutral mode [74]. These were the data encompassed in our former studies. The present work also includes the CMD-3 data sample [79] recently published.

- **iv/ For the $(\pi^0/\eta)\gamma$ annihilation channels :**

As for the $e^+e^- \rightarrow \pi^0\gamma$ cross section, in our energy range, the available data samples are scarce : One sample has been provided by CMD-2 [80] and another one by SND [81] – which supersedes the former [82] used in our previous studies [25, 26, 27]; the older SND $\pi^0\gamma$ spectrum given in [83] is also considered.

Regarding the $e^+e^- \rightarrow \eta\gamma$ cross section, the situation is more favorable as six data samples corresponding to different η decay modes have been collected by CMD-2 [84, 85, 80] and SND [83, 86]. Nevertheless, no newly collected data sample for this channel has been reported.

- **v/ For the $\pi^+\pi^-\pi^0$ annihilation channel :**

As no newly collected sample covering the energy region up to the ϕ mass has been reported, we are left with only the samples already examined in our previous analyses [25, 26, 27]. These have been collected by CMD-2 [72, 78, 87, 88] and SND [89, 90] and cover either the ω peak region or the ϕ peak region. We also consider the 3-pion spectrum given in [91] as it mostly deals with the region in between the ω and ϕ peaks, allowing for a valuable constraint on the ρ^0 meson physics background.

However, preliminary fits showing that the sample in [87] exhibits an average χ^2 per data point much above 2 – as also yielded by [92] in a different theoretical context – we have been led to discard it from our fits. Overall, one is left with nine data samples, including an old sample from the former CMD Collaboration.

- **vi/** *The pion and kaon form factors in the spacelike region :*

One of the motivations to develop a new breaking procedure for the HLS Model is to design it in such a way that the resulting broken model (BHLS₂) could encompass accurately the close spacelike region of the pion and kaon form factors. Indeed, a fair account of $F_\pi(s)$ in a region which stretches on both sides of $s = 0$ is the best way to ascertain the low energy behavior of the $e^+e^- \rightarrow \pi^+\pi^-$ cross section which provides an enhanced contribution to $(g - 2)_\mu$.

The NA7 Collaboration has measured the pion form factor [47] in the spacelike range $Q^2 \in [-0.253, -0.015]$ GeV² with good statistics and a small reported normalization error (0.9%); two years later, NA7 has also published a measurement of the charged kaon form factor [48] over the range $Q^2 \in [-0.0950, -0.0175]$ GeV² with also a small reported normalization uncertainty of 1%. On the other hand, an experiment at Fermilab had previously published less precise spectra on the pion and kaon form factors [93, 94] over resp. $Q^2 \in [-0.092, -0.039]$ GeV² and $Q^2 \in [-0.1145, -0.0409]$ GeV². Unlike former experiments¹⁸ at higher virtualities and, more modern experiments¹⁹ [96, 97, 98, 99, 100, 101], Refs. [47, 93] – and [48, 94] as well – report on results derived in resp. π and K scattering on atomic electrons and are, thus, model independent.

As a matter of fact, one should also note that there is no K^0 form factor spectrum measurement in the spacelike region, which would be a real challenge; nevertheless, measurements of $\langle r_{K^0}^2 \rangle$ exist [102, 103] which report negative values.

A common feature of the data samples we have to deal with is that their systematic errors are quite generally reported as correlated; this implies that the corresponding error covariance matrices W can be of large dimension (especially for the BaBar and KLOE samples). As the input to the χ^2 expressions which feed our fitting code are just their inverses W^{-1} , the issue has been to ascertain the quality of these. For this purpose, we have chosen using the subroutines of the NAG library. Numerical checks have nevertheless been performed on the eigenvalues, the diagonal and non-diagonal elements of the products $W \cdot W^{-1}$ to verify that numerical departures from unit matrix properties were indeed negligible.

14 Comments on the Model Parameters

Before going on, it is worthwhile commenting on the fit parameters of the broken HLS Models. Basically, the number of parameters of the original (unbroken) HLS Model [21, 18, 22] to be fixed from data is small. As for its non-anomalous sector, besides f_π , these are the universal vector coupling g and the specific HLS parameter a , generally found to slightly depart from 2, the value expected from standard VMD approaches. Its anomalous sector [22] involves

¹⁸ Reference [95] has collected the results of several of them.

¹⁹ Former references can be found in the quoted papers.

a few more parameters already displayed in the Lagrangian pieces presented in Section 12 : $c_1 - c_2$, c_3 and c_4 . There are strong motivations [21, 18] to impose $c_3 = c_4$. So, when unbroken, the HLS model depends on only four unconstrained parameters.

There are two parameter categories introduced in our approach: the coefficients of the subtraction polynomials which supplement the corresponding loops and, on the other hand, the breaking parameters inherently affecting the present Lagrangian – and those defined in [25].

Traditionally, as illustrated by the Gounaris-Sakurai formula [45], the coefficients of the subtraction polynomials are reexpressed in terms of the resonance mass and width, which are determined by a fit to the data. In a global approach like ours, the subtraction polynomials affect loops which come *simultaneously* in the various amplitudes associated with the various annihilation processes *simultaneously* under examination. In this case, as there is no reason to favor a specific channel to fix the meaning and the value of parameters which come in all channels, the strategy adopted is to let the data, *as a whole*, determine the subtraction parameter values via a *global* fit. Even if the parameter content may look less intuitive, this approach – also adopted in BHLS [25] – looks the most motivated. This does not prevent to extract usual physics quantities, relying on the fit results, as done since [24, 25], for instance.

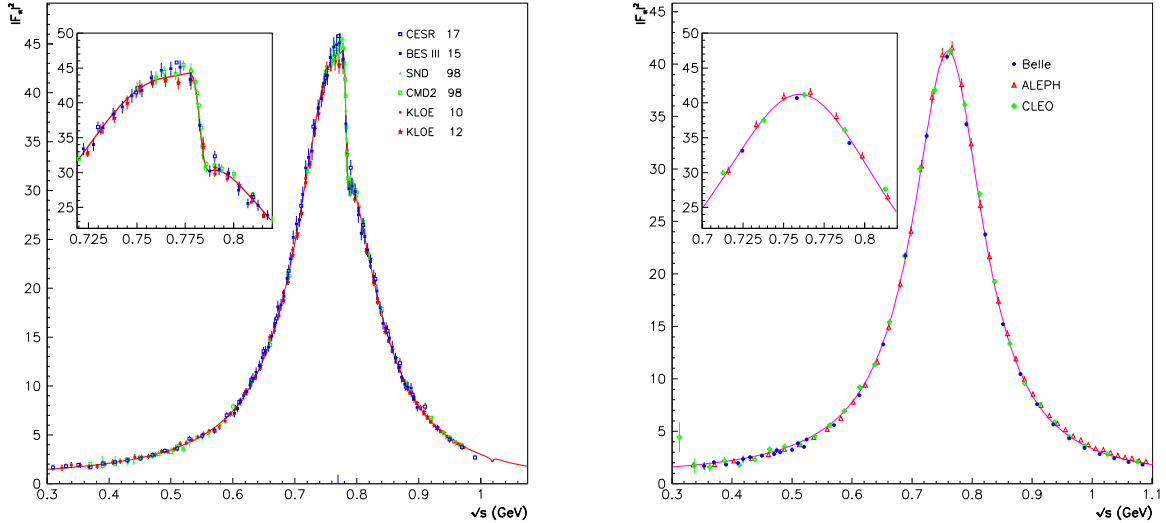


Figure 2: BHLS₂ fit to the $\pi\pi$ data, the RS solution : The leftmost panel shows the pion form factor squared in the e^+e^- annihilation and the rightmost one displays the same spectrum in the τ decay. The fitted regions extend up to $s = 1.0 \text{ GeV}^2$.

In the second category of parameters, besides the parameters of the unbroken HLS model reminded just above, one finds all those introduced by the various aspects of the breaking procedure at work. As for the parameters generated by the BKY mechanism and reminded in Section 3, six in total, the condition $\Sigma_A = 0$ is already stated since the original BHLS Model [25]. It has been shown in Section 7 that the diagonalization procedure of BHLS₂ imposes $\Delta_V = 0$. Therefore, four BKY parameters only (Σ_V , Δ_A , z_A and z_V) remain free.

In Sections 7 and 9, it was also shown that $\xi_0 = \xi_8$ comes as a natural constraint on the parameters of the CD breaking defined in Section 4. Therefore the CD breaking involves two more parameters²⁰ $\xi_0 (= \xi_8)$ and ξ_3 . Finally, switching on the Primordial Mixing introduces three more parameters (ψ_0 , ψ_ω and ψ_ϕ) into the fit procedure.

15 The BHLS₂ Global Fits : General Features

Various kinds of global fits have been performed using the data samples and channels listed in Section 13, with or without the spacelike data, with or without the τ data, fixing some of the model parameters (the ψ_α 's angles and z_V) or leaving all of them free.

When mixing as many data samples carrying important – sometimes dominant – overall normalization uncertainties, the effect of the so-called Peelle's Pertinent Puzzle (PPP) [104] cannot be ignored to avoid getting biased estimates for physics quantities. The use of χ^2 minimization methods, first questioned, has been finally justified [105, 106]; however, when dealing with distributions or form factors, the pertinent method turns out to invoke the underlying (theoretical) model function which is just what fits are supposed to provide. Following [107], [27] has defined an iterative procedure proved to cancel out biases (see the Appendix in [27]).

It is worthwhile briefly sketching the conclusions of²¹ [27] concerning the issue just reminded : **1/** The normalization uncertainty (denoted σ , possibly s -dependent) of any spectrum T is absorbed within the total covariance matrix contributing to the general χ^2 , **2/** The correction which affects the normalization of T is *derived* from the data, the theoretical function provided by the fit, σ and the *statistical* covariance matrix – which may absorb the uncorrelated systematics.

Let us make a few general statements about fit results and data before focusing on specific topics, mainly the $K\bar{K}$ and τ sectors and the spacelike region behavior of the pion and kaon form factors. The detailed properties will be emphasized in the next Sections.

- As for the behavior of the data samples within our global fits, one can state that the issues met with the dipion spectra from BaBar [65, 66] and KLOE08 [62] within the BHLS framework [25] are confirmed within the BS and RS variants of the BHLS₂ framework studied here; they are also discarded in the present study.

Whatever the specific conditions of the various fits performed, the $\pi^+\pi^-$ data samples from NSK (*i.e.* CMD-2 and SND), KLOE10/12, BESIII [67] and CLEO-c [68] are as well described within the BHLS₂ framework as they were already within BHLS [25]; more precisely, NSK and KLOE10/12 contribute an average χ^2 per data point of $\simeq 1$, while the BESIII and CLEO-c samples yield $\chi^2/N_{\text{pts}} \simeq 0.6$. Figure 2 displays the spectra and fits for the pion form factor in the e^+e^- annihilation and in the τ decay.

- In order to account for the difficulty to fully address the $\pi^+\pi^-\pi^0$ channel in the ϕ mass region within BHLS, a so-called B model was defined which simply turns out to discard from fit this mass region for (only) this channel [25]. In contrast, BHLS₂ does not meet

²⁰Rigorously speaking, as already noted, two more breaking parameters can be defined addressing the charged and neutral K^* mesons.

²¹See, in particular, its Section 4.

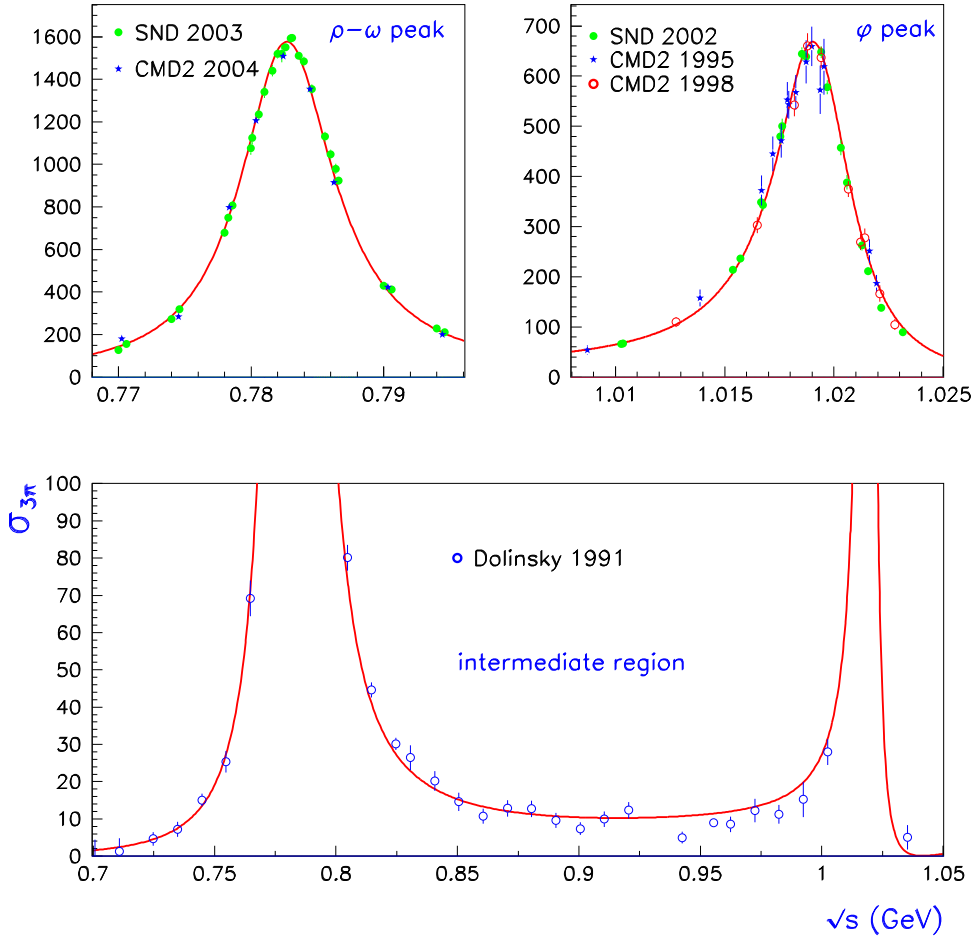


Figure 3: BHLS₂ fit to the $\pi^+\pi^-\pi^0$ spectra, the RS solution : Top panels show the fit and data in, resp. the ω and ϕ regions, the bottom one focuses on the intermediate region.

any issue²² and achieves a fair description of the $\pi^+\pi^-\pi^0$ data up to, and including, the ϕ mass region. The spectra are shown in Figure 3.

- Finally, the $e^+e^- \rightarrow (\pi^0/\eta)\gamma$ spectra are also nicely fitted within BHLS₂ – as well as in the former BHLS – as illustrated by Figure 4. Quite generally, one obtains $\chi^2/N_{\text{pts}} \simeq 90/112$ and $\chi^2/N_{\text{pts}} \simeq 120/182$ for resp. the $\pi^0\gamma$ and $\eta\gamma$ channels.

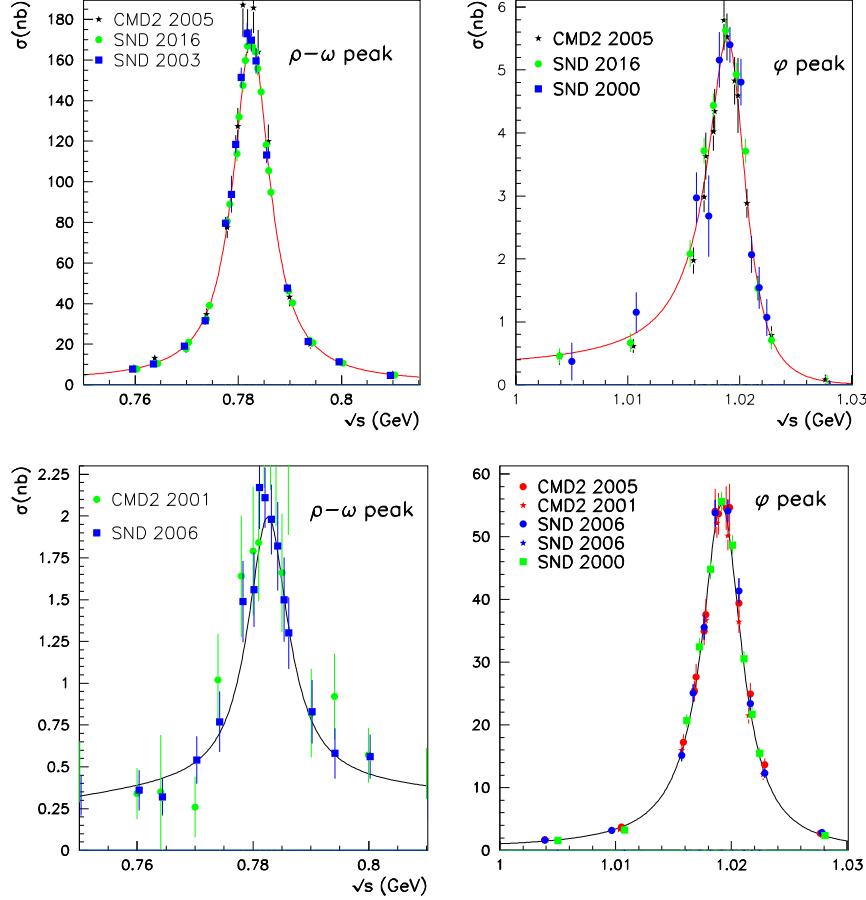


Figure 4: BHLS₂ fit to the $(\pi^0/\eta)\gamma$ spectra, the RS solution : Top panels show the case for the $\pi^0\gamma$ spectra in the ω and ϕ regions, the bottom panels display the corresponding plots for the $\eta\gamma$ spectra.

In order to perform global fits, one obviously should make an assumption on the energy calibration of each of the data samples considered. For the dipion spectra, one has gathered into the fit data coming from the VEPP-2M machine at Novosibirsk (CMD-2 and SND), data from DAPHNE (KLOE10 and KLOE12), from BESIII and from CESR. A significant mismatch of the relative energy calibrations of these would have produced a failure of their common fit because of the $\rho - \omega$ drop off region; this is clearly not seen neither in the χ^2 contributions of

²²As for the discarded data sample [87], see the above Section 13 and also [92].

the various samples, nor in Figure 2 (see the inset in its leftmost panel). Moreover, comparing both panels in this Figure excludes a significant energy calibration mismatch between e^+e^- and τ data.

Moreover, the data collected by CMD-2 and SND around the ω and ϕ peaks in the 3-pion channel as well as in the $(\pi^0/\eta)\gamma$ final states indicate a good consistency between the energy calibrations of the various data samples collected in different runs distributed over several years. This is visible in the fit properties as well as in the Figures where the fit function and the various data are displayed.

16 The BHLS₂ Global Fits : The $e^+e^- \rightarrow K\bar{K}$ Channels

The available data covering the K^+K^- channel²³ come from SND, CMD-2 and BaBar. Recently CMD-3 has published a new K^+K^- measurement [77]. As for the neutral channel, most data come from CMD-2 and SND and have been listed in Section 13. A new data sample covering our fitting range has also been produced by CMD-3 [79]; unfortunately, the published K_LK_S spectrum from BaBar starts at 1.06 GeV, just above our fitting range [108].

16.1 Preliminary Remarks

As for the K^+K^- channel : In its [77], the CMD-3 Collaboration points toward disagreements with both the BaBar [76] and the original CMD-2 data samples [73]. Once the correction factor (1.094 ± 0.040) for the trigger efficiency of CMD-2 is applied, the discrepancy between the CMD-3 and CMD-2 K^+K^- samples looks much reduced [75] – possibly washed out. Anyway, a full examination of the various $e^+e^- \rightarrow K\bar{K}$ data samples²⁴ is worth addressing.

On the other hand, preliminary BHLS₂ analyses based on the CMD-3 and BaBar data, made us aware of a visible degradation of both $K\bar{K}$ channel data description above $1.025 \div 1.030$ GeV; therefore, in the present work, one limits the fit region for the $K\bar{K}$ data to the $\sqrt{s} \in [2m_K, 1.025 \text{ GeV}]$ range. The explanation for this effect is unclear. It could be an intrinsic weakness of the BHLS/BHLS₂ models²⁵ which, as it stands, does address a possible onset of the high mass vector meson contributions; it could also reflect an experimental issue. For the sake of consistency, we have chosen to impose the same fitting range also to the former CMD-2 and SND data samples in both the charged and neutral modes,

16.2 A Specific Issue of the $K\bar{K}$ Data

As already pointed out, one does not detect any indication for a mismatch in the energy calibration of the various data samples covering the 3-pion and $(\pi^0/\eta)\gamma$ channels, all collected

²³In the following, as already noted in Section 13, the two CMD-2 scans [73] are corrected as stated in [75]. As for the BHLS predictions in [25, 26, 27], they are updated correspondingly.

²⁴As for the contribution to the muon HVP of the energy region from $s \in [4m_K^2, 1.06 \text{ GeV}^2]$ to $a_\mu(K^+K^-)$, BaBar obtains $18.64 \pm 0.16_{\text{stat}} \pm 0.13_{\text{syst}} \pm 0.03_{VP}$ while CMD-3 gets 19.33 ± 0.040 in units of 10^{-10} , a difference of $\simeq 0.7 \times 10^{-10}$ between the central values, a 3.25σ effect.

²⁵The standard HLS framework [18], which underlies the BHLS/BHLS₂ models, does not account for vector particles not belonging to the fundamental vector nonet.

with the CMD-2 and SND detectors on the same VEPP-2M collider. One also does not observe any mismatch between the energy calibration of the 3-pion and $(\pi^0/\eta)\gamma$ data and those collected by the same collaborations in the $K\bar{K}$ channels. Nevertheless²⁶, CMD-2 and SND carry a (correlated) absolute energy uncertainty in the range of $30 \div 40$ keV, while for CMD-3, the absolute energy uncertainty is $\simeq 60$ keV, statistically independent of that of CMD-2 & SND. Moreover, BaBar also reports a 50 keV correlated energy scale uncertainty[76]. When dealing with an object as narrow as the ϕ meson within a global framework, these uncertainties should be accounted for otherwise, the fits cannot succeed.

As the bulk of data samples for both $K\bar{K}$ channels has been provided by CMD-2 and SND, it looks quite natural to choose their common energy calibration as a reference; this will be denoted E_{NSK} in the following. For this purpose, one defines $E_{\text{CMD3}} = E_{\text{NSK}} + \delta E_{\text{CMD3}}$ and $E_{\text{BaBar}} = E_{\text{NSK}} + \delta E_{\text{BaBar}}$ to recalibrate the CMD-3 and BaBar data point energies in a fully correlated way and derive their E_{NSK} equivalent energy.

Therefore, in order to deal with the $K\bar{K}$ data, we are faced with a case where two kinds of correlated uncertainties have to be accounted for: Energy calibration and absolute normalization of the cross-sections. Hence, one merges in the minimization procedure the method developed in [27] and the two calibration parameters δE_{CMD3} and δE_{BaBar} to be also determined within the same fits.

For this purpose, one assumes that there is no *functional* relation between the normalization uncertainty λ_i – of an experiment labeled i – and the energy scale uncertainty δE_i ; then, as $\partial\lambda_i/\partial[\delta E_i] = 0$ for each experiment, substituting, as emphasized in [27], the value for λ_i derived from $\partial\chi^2/\partial\lambda_i = 0$ into the expression for χ^2 is unchanged compared to [27].

16.3 Fitting the $K\bar{K}$ Channels : NSK, BaBar and CMD-3 Separately

In the following, the non-kaon sector data and channels used in our fits include, unless otherwise stated, the $\pi^+\pi^-$, $\pi^+\pi^-\pi^0$, $\pi^0\gamma$, $\eta\gamma$ annihilations, the τ decay to $\pi^\pm\pi^0$ and a few decay partial widths (see [25]). One starts by discussing the fits where the CMD-2 & SND (NSK), BaBar and CMD-3 kaon data are not influencing each other within the minimization procedure. Table 1 gathers most of our results in this case; these are commented right now.

- With regard to NSK : $\langle \chi^2 \rangle$, the average (partial) χ^2 per NSK data points, is of order 1 in both the neutral and charged kaon channels; thanks to the fair description of the other channels involved in the fit, the global fit probability exceeds the 90% level.

As reminded above, the procedure defined in [27] allows us to derive from the fit procedure the normalization (absolute scale) correction to be applied to each spectrum²⁷. For the charged channel, one gets +5.0% for SND (expect. value 7.1%), a 0.7σ effect, and –1.6% for CMD-2 (updated expectation 4.4%), a 0.3σ effect; in the neutral channels, one correspondingly obtains –1.8% (expect. value 4.2%) for SND and +0.6% (expect. 1.7%) for CMD-2, resp. 0.4σ and 0.3σ effects.

²⁶E. Solodov, Budker Institute, Novosibirsk, private communication.

²⁷One should stress that such a "renormalization" is the natural outcome to the scale uncertainty problem and that the main advantage of any kind of global fit is to allow determining such a correction in consistency with a (large) set of data samples coming from different sources.

Therefore the CMD-2 and SND data samples successfully fit the BHLS₂ framework and, moreover, the derived scale corrections meet the reported scale uncertainty expectations.

- With regard to BaBar : One has chosen to supply the NSK neutral data to the fits in order to populate each dikaon channel as the BaBar $K_L K_S$ data [108] do not cover our fitting energy range. As the BaBar charged spectrum [76] has been collected in the ISR mode, it looks appropriate to compare, within the fit, each spectrum datum in a bin to an average value of the model spectrum over the bin width. The second data column in Table 1 shows that the BaBar sample yields $\langle \chi^2 \rangle = 1.7$, somewhat large, and a global fit probability also above the 90% level.

The minimization procedure returns as energy shift vs NSK $\delta E_{\text{BaBar}} = -125.8 \pm 19.0$ keV; this looks fair when compared to the independent $30 \div 40$ keV (NSK) and 50 keV (BaBar) energy calibration uncertainties. Moreover, the spectrum scale correction is at the 10^{-4} level – so that the absolute scale of the BaBar spectrum has not to be corrected. On the other hand, the scale corrections for the neutral NSK data included in the fit are -2.1% (SND) and $+0.7\%$ (CMD-2), almost identical to what has been obtained in the fit of the NSK data in isolation mode.

Interestingly one can also derive the scale correction for the charged data of SND ($+5.2\%$) and CMD-2 (-3.7%) even if they are not submitted to the fit; these predictions are clearly in the expected ballpark. This indicates, beforehand, that NSK and BaBar data in the kaon sectors are consistent with each other.

- As for CMD-3 : This Collaboration has provided data samples in both dikaon final states, When fitting these data, the correspondence is made – as with NSK – between each datum and the theoretical model computed at the nominal energy. As for NSK and BaBar, the systematic uncertainties are treated as fully correlated and serve to build up the systematic covariance matrices to be added up to the statistical ones; these are used in the fitting of the neutral and charged CMD-3 data within the global BHLS₂ framework. The fit results are displayed in Table 1.

The $\langle \chi^2 \rangle$ for both CMD-3 data samples are clearly very large and the global fit probability poor. The scale corrections found are $+1.2\%$ (charged channel) and -1.2% (neutral channel) to be compared to the reported r.m.s., resp. 2.0% and 1.8% . The possibility of treating the bin information as in ISR experiments²⁸ has been examined – specifically, only in the neutral channel – and in view of the outcome, we gave up.

For the sake of completeness, we have nevertheless also performed the fit of the CMD-3 data in isolation by discarding the *non-diagonal part* of the total covariance matrix²⁹, as seemingly done in [76] for the BaBar data; the fit results change dramatically as one reaches $\langle \chi^2 \rangle = 14/16$ and $\langle \chi^2 \rangle = 17/17$ for resp. the charged and neutral modes of the CMD-3 data and with a fit probability exceeding 90%. Moreover, in this case (CMD-3 data in isolation) the corrections to the original normalization of the cross-sections

²⁸Comparing the datum information to the fit function averaged over the bin width, as just sketched for BaBar.

²⁹This turns out to consider that the systematic uncertainties are fully uncorrelated; some configurations intermediate between full correlation and no correlation can lead to similar results.

become negligible ($\simeq 10^{-4}$) for both the charged and neutral channels³⁰. As for the energy shift vs NSK it moves from -51.4 ± 13.7 keV (see Table 1) to -44.6 ± 14.8 keV, still in the expected ballpark.

χ^2 ($K\bar{K}$ Sample Set)	NSK	BaBar	CMD3
NSK $K_L K_S$ (92)	107	100	—
NSK $K^+ K^-$ (49)	51	—	—
BaBar $K^+ K^-$ (27)	—	46	—
CMD3 $K_L K_S$ (17)	—	—	120
CMD3 $K^+ K^-$ (16)	—	—	88
χ^2/N_{pts}	1087/1210	1078/1188	1155/1102
Probability	97.5%	95.2 %	3.8 %
δE (keV)	—	-125.8 ± 19.0	-51.4 ± 13.7

Table 1: BHLS₂ fit properties in the kaon sectors. The kaon data from NSK, BaBar and CMD-3 are fitted in isolation. Running BaBar data ”alone” is complemented by the NSK data for the $K_L K_S$ channel. The data and channels other than kaon are identical in all cases; the full χ^2 value and the total number of data points (N_{pts}) refer to the global fit. The last line displays the shift values δE_{CMD3} or δE_{BaBar} relative to the NSK data energy calibration.

16.4 Fitting the $K\bar{K}$ Channels : NSK, BaBar and CMD-3 Combined

This Subsection is devoted to analyzing the consistency of the three available groups of data. Quite generally, the covariance matrices used within the fit procedure assume full correlation for the systematics, as in the previous paragraph. Nevertheless, one also briefly reports on additional information about a fit performed assuming the systematics uncorrelated for CMD-3 data. It is worthwhile proceeding with pairwise combinations.

- As clear from the first data column in Table 2 – and as could be inferred from the results already reported – one observes a fair consistency between NSK and BaBar samples within the global BHLS₂ framework. Comparing the present NSK and BaBar contributions to the (total) χ^2 with their analogs in their fits in isolation clearly shows that there is no significant tension between them. The only noticeable difference is the central value for δE_{BaBar} found closer to 100 keV by 1σ .

³⁰The $\langle \chi^2 \rangle$'s of the *fit prediction* to NSK data remain in reasonable correspondence with the NSK fit in isolation (55/49 and 105/92) while the distance of this prediction to BaBar data degrades more severely (76/27).

Other pieces of information concerning the absolute spectrum normalization³¹ are worth to be mentioned. The fit outcome indicates that the BaBar data normalization should be downscaled by $\simeq 0.4\%$, the (updated) CMD-2 charged spectrum by 1% while the SND charged data normalization should be increased by 8.1%. These corrections are always consistent with the respective expectations reminded above.

$K\bar{K}$ Sample Set	NSK+BaBar	NSK+CMD3	BaBar+CMD3	NSK +BaBar
(# data points)		(CMD3 corr.)	(CMD3 corr.)	+ CMD3 uncorr.
NSK $K_L K_S$ (92)	106	105	(108)	113
NSK $K^+ K^-$ (49)	50	52	(50)	50
BaBar $K^+ K^-$ (27)	46	—	45	56
CMD3 $K_L K_S$ (17)	—	121	122	18
CMD3 $K^+ K^-$ (16)	—	98	97	23
χ^2/N_{pts}	1133/1237	1331/1243	1212/1129	1193/1270
Probability	93.3%	1.1 %	0.8 %	81.5 %
δE_{CMD3} (keV)	—	-46.5 ± 6.7	-45.9 ± 3.9	-38.2 ± 11.7
δE_{BaBar} (keV)	-105.8 ± 17.2	—	-105.5 ± 16.1	-103.2 ± 16.7

Table 2: BHLS₂ fit properties in the kaon sectors. The kaon data from NSK, BaBar and CMD-3 are fitted pairwise combined. The χ^2 values are displayed for individual channels or for the total number of data points N_{pts} . In the two rightmost data columns, the top entry is δE_{CMD3} and the bottom one δE_{BaBar} . The rightmost column displays the fit results when treating the CMD-3 systematics as uncorrelated.

- The second data column in Table 2 displays results from fits combining NSK and CMD-3. Here also one observes a striking resemblance between the individual partial χ^2 's in the combined fit and in their fits in isolation, *i.e.* the NSK data samples go on yielding $\langle \chi^2 \rangle_{\text{NSK}} \simeq 1$ while one gets $\langle \chi^2 \rangle_{\text{CMD3}} > 6$; the global fit probability is also poor.

Besides the energy shift $\delta E_{\text{CMD3}} = -46.5 \pm 6.7$ keV, the spectrum rescalings derived from the fit are interesting pieces of information. In this way, the fit returns an increase of the charged CMD-3 data normalization by only 0.2% while the neutral CMD-3 ones should be downscaled by 2.6% (a 1.5σ effect). One also finds that the SND charged data normalization should undergo an increase by 9.2%, while for CMD-2 the increase is only 1.5%. As for the neutral kaon normalizations, SND should be downscaled by 2.1%,

³¹ For SND and CMD-2, as their corrections are computed run by run and sample by sample, here we only give average values, for simplicity.

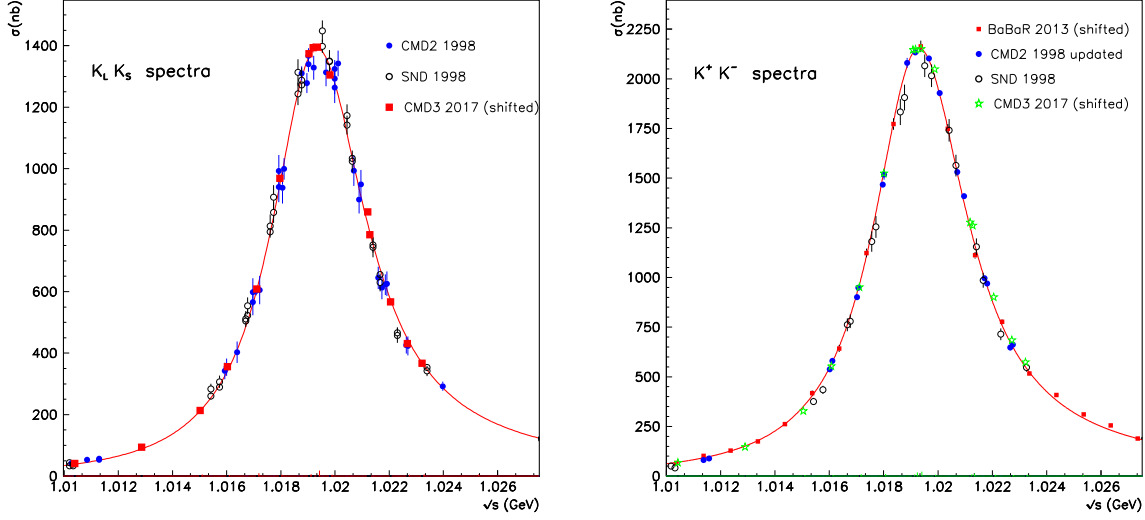


Figure 5: BHLS₂ global fit to the K^+K^- and K_LK_S spectra (RS solution) : The plotted CMD-3 data are *not* fitted but are shifted by a δE_{CMD3} determined elsewhere. The value for δE_{BaBar} is derived from this fit. All experimental spectra are rescaled as emphasized in the text.

while CMD-2 is increased by 0.5%. So, one does not observe major changes in the NSK normalizations.

- The third data column in Table 2 displays results from fits combining BaBar and CMD-3 kaon data, excluding their NSK analogs. The global fit probability clearly indicates that such a combination is not really favored; one should remark, nevertheless, that all properties exhibited by CMD-2 and SND are in fair correspondence with their analogs yielded in their fits in isolation; additionally, even the χ^2 distances of the CMD-3+BaBar fit function to the NSK data (not under fit) – given within parentheses – are analog to their values derived in NSK alone or NSK+BaBar fits.

Quite interestingly, the tension observed between CMD-3 on the one hand, and BaBar and NSK on the other hand, is not manifest in plots, as soon as the energy calibration of CMD-3 vs NSK is applied. For instance Figure (5), shows the $K\bar{K}$ cross sections derived from the fit to NSK + BaBar; the corresponding data are rescaled and appropriately shifted as emphasized in the previous item; one has *superimposed* the (unfitted) data from CMD-3 shifted by -45.9 keV and rescaled as *predicted* by the NSK + BaBar fit : -4.3% and -2.4% for resp. the charged and neutral CMD-3 data samples.

On the other hand, one has found worth to also perform the fit sketched in the rightmost data column in Table 2, *i.e.* treating the NSK and BaBar uncertainties as fully correlated and both CMD-3 data samples as carrying uncorrelated uncertainties. Using the corrections to the absolute normalization of each sample as derived from this fit³², one gets a

³² This amounts to the following rescalings w.r.t. the original normalizations : -1.3% (CMD-3 K^+K^-), -0.5% (CMD-3 K_LK_S), $+8.1\%$ and -0.3% (K^+K^- from resp. SND & CMD-2), $+0.4\%$ and -0.5% (K_LK_S from resp. SND & CMD-2) and $\simeq -0.3\%$ for BaBar K^+K^- .

figure which superimposes exactly to Figure (5), in the smallest detail.

This clearly indicates that the observed tension is essentially due to the non-diagonal parts of the CMD-3 error covariance matrices constructed from experimental information, as also done for the other data samples, CMD-2 in particular.

17 Fit Properties of the Various Broken HLS Models

Channels	BHLS [25]	BHLS ₂ (BS) space, NO τ	BHLS ₂ (BS) space, τ	BHLS ₂ (RS) space, τ
NSK $\pi^+\pi^-$ (127)	137	140	139	137
KLOE $\pi^+\pi^-$ (135)	140	138	154	137
τ (ABC) (85)	85	—	98	92
$\pi^0\gamma$ (112)	91	88	89	86
$\eta\gamma$ (182)	120	121	122	120
$\pi^+\pi^-\pi^0$ (158)	79/96	148	153	141
NSK $K_L K_S$ (92)	97	107	106	106
NSK K^+K^- (49)	51	49	48	50
BaBar K^+K^- (27)	49	45	44	46
space K^+K^- (25)	—	19	19	18
space $\pi^+\pi^-$ (59)	—	58	63	55
χ^2/N_{pts}	949/1056	1054/1152	1185/1237	1133/1237
Probability	96.7%	93.9 %	67.6%	93.2%

Table 3: Global fit properties of BHLS and of the BS and RS variants of BHLS₂ : χ^2 values yielded by each group of data samples for the indicated channel. Numbers within parentheses in the first column indicate the numbers of data points submitted to fits; for BHLS, the actual number of fitted data points in the 3π channel (model B) is shown in the entry as χ^2/N_{pts} .

All fits referred to in this Section involve the collection of data samples and channels already described and listed in Section 13; as for the $K\bar{K}$ channels, one limits oneself to using only the samples from CMD-2 (updated), SND and BaBar which do not show any obvious

tension. The motivation for this choice is to avoid disentangling model dependence effects, on the one hand, and identified tensions among data samples³³ on the other hand. There is indeed no gain in increasing the statistics if this turns out to increase the systematics in an uncontrollable way.

The BHLS₂ fits presented up to now have been derived using the so-called Reference Solution (RS); this solution combines the so-called Basic Solution (BS) defined in Section 7 and the Primordial Mixing defined in Section 8.

Nevertheless, in order to explore model dependence effects, analyzing also the fit results derived using BS is certainly relevant. On the other hand, for the same concern, we have rerun the BHLS model [27] using the SND together with the *updated* CMD-2 data; it then looked appropriate to also include the BaBar dikaon sample.

Therefore, with the BS and RS variants of BHLS₂ and with BHLS, one actually has at disposal three approaches to the same data; as for BHLS, one concentrates on the so-called model B which circumvents the issue met at the ϕ mass in the three pion annihilation channel which is one of the motivations having led to BHLS₂. The other one was to ascertain the description of the dipion threshold region and to improve the accountability of the spacelike region. The main fit properties are sketched in Table 3 and deserve some comments.

The leftmost data column – dealing with BHLS – shows the various χ^2 for the displayed channels and the sum of the contributions of all data submitted to the fit. In all channels the average χ^2 is of the order 1 or better³⁴ and the (global) fit probability is fairly good.

The rightmost data column displays the corresponding information derived with the RS variant of BHLS₂. Here also, the fit quality is good and one yields a fair probability. One should note the quite favorable $\langle \chi^2 \rangle$'s for the pion and kaon form factors in the spacelike energy region in conjunction with good χ^2 's in their timelike regions; the spacelike data samples – coming from NA7 and Fermilab – are discussed in detail in the next Section. As far as we know, the fits presented here are the first ones involving the pion and kaon form factors simultaneously in their timelike and spacelike regions with such quality.

The third data column displays the fit properties derived from the BS variant of BHLS₂ using the same data as those just discussed for the RS variant. The fit probability is lower than usual in the HLS context. Scrutinizing the various items displayed in Table 3, one clearly observes a significant tension in the BS fit absent from the RS fit results *when the τ data are involved*. Indeed, when going from RS to BS χ^2_τ increases by 6 units, but $\chi^2_{3\pi}$ increases by 12 and $\chi^2_{\text{space}\pi}$ by 8; moreover³⁵, $\chi^2_{KLOE\ 2\pi}$ increases by 17 units whereas $\chi^2_{NSK\ 2\pi}$ is marginally affected (a 2 unit increase).

Instead, the BS fit performed *when discarding the τ data* leads to a picture in good correspondence with the RS fit results already commented; indeed, the partial χ^2 's reported in the second data column of Table 3 are similar to those obtained by fitting with the RS variant of the BHLS₂ model. Nevertheless, some tension survives in the 3-pion sector while the dipion

³³The issue between BaBar and CMD-3 charged kaon data has already been noted in [77].

³⁴One should note the smaller number of data points considered in the fit procedure for the $\pi^+\pi^-\pi^0$ annihilation channel, because of excluding the data points from the ϕ region.

³⁵The different behavior of the NSK and KLOE dipion data under BS global fits reflects the different magnitude of the uncertainties which makes the NSK dipion data – and likewise for those from BESIII and CESR – more permissive than their KLOE analogs.

spectra and the spacelike data almost recover their optimum fit quality; so, the BS variant of BHLS₂ exhibits a quite acceptable behavior once the τ sector is discarded.

In conclusion, despite their different structures – and taking into account the peculiarities of the BS variant of BHLS₂ – these models/variants open the possibility to examine model dependence effects in the evaluation of some reconstructed physical quantities; this may allow to compare these with the systematics generated by dealing with contradictory samples.

18 The Pion and Kaon Form Factors in the Spacelike Region

By allowing different HK masses for the ρ^0 and ω mesons, BHLS₂ naturally permits a smooth connection between the spacelike and timelike sectors of the pion and kaon form factors. Moreover, applying in this context the vector meson dynamical mixing (see Section 10), does not break this smooth connection because $\alpha(s=0)=0$ becomes automatic and supplements the (already) vanishing properties of the other angles : $\beta(s=0)=\gamma(s=0)=0$.

BHLS ₂ : BS fit	incl. spacelike data	excl. spacelike data **
space $\pi^+\pi^-$ (59)	57.6	58.6
space K^+K^- (25)	18.8	19.0
χ^2/N_{dof}	1054/1152	977/1068
Probability	93.9%	92.8 %

Table 4: BS variant global fits excluding τ data: The leftmost data column shows the partial χ^2 's in the fit including both kinds of spacelike data, the rightmost one shows the corresponding results in the fit excluding all spacelike data. Global fit information is displayed in the last lines. The numbers of fitted data points in each channel are given within parentheses.

18.1 The Pion and Kaon Form Factors in the Close Spacelike Region

Figure 6 displays the pion and kaon form factors in the spacelike region coming out from the fit. The spacelike data supplied to the global fit procedure are only the (model-independent) data samples collected by the NA7 [47, 48] and Fermilab experiments [93, 94]. Altogether, these experiments cover photon virtualities down to $\simeq -0.25 \text{ GeV}^2$ and $\simeq -0.12 \text{ GeV}^2$ for resp. the pion and kaon form factors.

The pion and kaon form factors derived from the global fit including the spacelike data are the red curves in Figure 6. Global fits have also been performed using the BS and RS variants of BHLS₂, *excluding the spacelike data*. The relevant fit results obtained using, for instance, the BS variant are displayed in Table 4. They correspond to the green curve in Figure 6; as for the kaon form factor the predicted (green) curve superimposes exactly to the fitted (red) one.

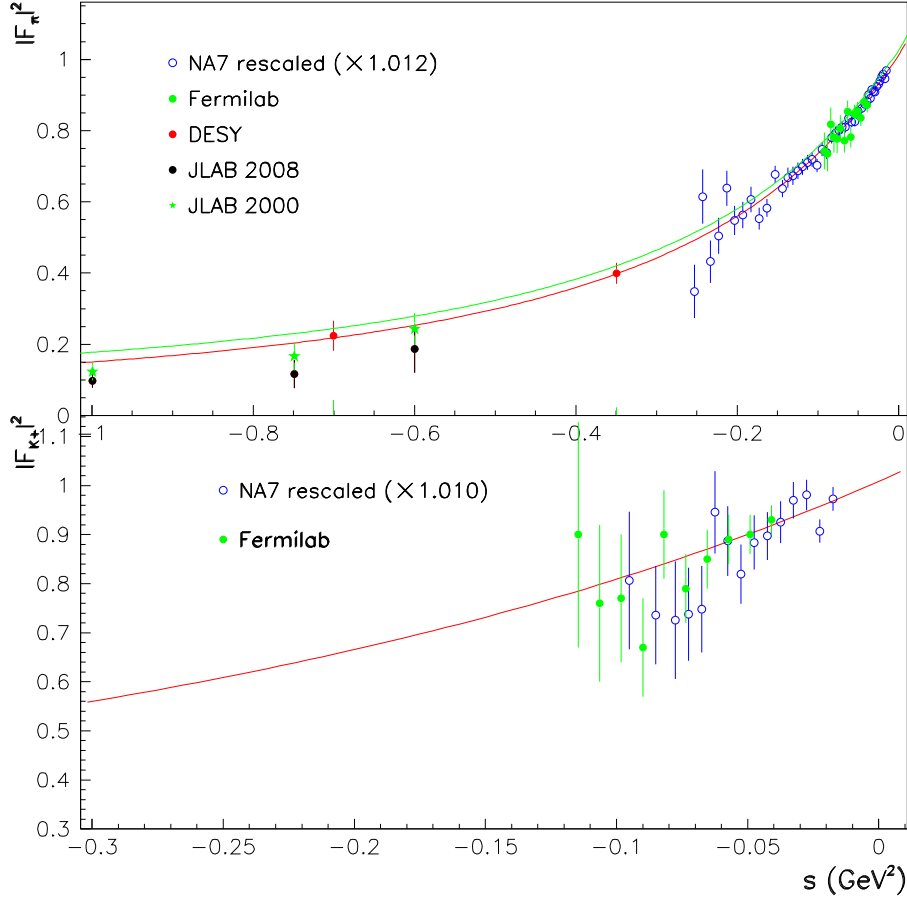


Figure 6: Form factors squared in the spacelike region. The top panel displays the BHLS₂ prediction (green curve) and the fit (red curve) together with the rescaled data for $|F_\pi(s)|^2$. The bottom panel displays the fit and the rescaled data for $|F_{K^\pm}(s)|^2$; the prediction from the fit excluding the spacelike data exactly superimposes to the fit (red curve). The unfitted points from DESY and JLab are only superimposed. See Section 18 for details.

Table 4 and Figure 6 obviously prove that the spacelike data are not a real constraint in the BHLS₂ global fit approach; stated otherwise, the BHLS₂ model supplied with *only* timelike data fairly well predicts the spacelike behaviors far inside the spacelike region for both the pion and kaon form factors. It is worthwhile to note that these analytic continuations are performed across energy squared distances which can be as large as 1 GeV². For instance, the kaon form factor displayed here is the analytic continuation of the charged kaon form factor fitted in the ϕ mass region, *i.e.* the curve shown on the rightmost panel of Figure 5. Such a property is rare enough to be underlined.

Figure 6 gives the opportunity to comment on the representation of spectra affected by a normalization (scale) uncertainty; the NA7 spacelike data are a quite simple illustration of handling the rescaling effects. When a scale uncertainty affects a spectrum, there are obviously

two possible ways to display the result : Either rescaling the data, keeping the fit/prediction untouched or performing the converse.

So, in Figure 6 one has chosen to display the NA7 data rescaled, keeping unmodified the fit (and prediction) function(s), the plotted uncertainties being the statistical ones. As for the Fermilab data samples, taking into account their low accuracy, no rescaling has been performed and the plotted uncertainties are just the reported total errors.

One can, for once, go into a few plotting details in simple wording. Following the method given in [27], the scale correction is given by :

$$\lambda = \frac{f_i V_{ij}^{-1} [m_j - f_j]}{f_k V_{kl}^{-1} f_l + \frac{1}{\sigma^2}}, \quad (98)$$

where (NA7) $\sigma = 0.9\%$ or 1.0% , $f_i = |F_P(s_i)|^2$ ($P = \pi^\pm, K^\pm$), V is the statistical error covariance matrix and m_i is the measured datum at $s = s_i$. The plotted NA7 data m' are related with the original ones m by :

$$m_i \rightarrow m'_i = m_i - \lambda f_i (\simeq [1 - \lambda] m_i).$$

Looking at Figure 6, the precise data (NA7 pion form factor) are indeed observed to tightly follow the fit function, *once the normalization correction is applied*.

It is relevant to provide the precise values for the λ 's derived from the fitted parameters. One thus finds :

$$\text{NA pion form factor : } \lambda_\pi = (1.18 \pm 0.02_{\text{sys}} \pm 0.03_{\text{fit}})\%$$

$$\text{NA kaon form factor : } \lambda_K = (1.05 \pm 0.03_{\text{sys}} \pm 0.02_{\text{fit}})\%$$

which exhibit noticeable accuracies. Subsection 18.3 below – and Figure 8 – illustrates that the predicted scale correction for the pion form factor is supported by the LQCD data which should be intrinsically free of scale uncertainties.

18.2 The Pion Form Factor : The Model-Dependent Data

As one cannot measure the pion form factor in a model-independent way for photon virtualities $Q^2 = -s > 0.3 \text{ GeV}^2$, this physics is performed using the scattering process $pe \rightarrow e\pi^+n$, referred to in the literature as $^1\text{H}(e, e'\pi^+)n$. In this approach, two questions should be addressed :

i/ Separating out the longitudinal cross section σ_L ,

ii/ Extracting F_π from σ_L .

One can refer to [97, 98, 99] for comprehensive accounts of the issues. As for item **i/**, the method has evolved and improved in the course of time from the early experiments (also reported in [95]) to the more recent ones [100, 101, 96]. Item **ii/** addresses more deeply the nuclear physics content of the process in order to account at best for the π^+pn vertex and for the off-shell character of the intermediate π^+ . Presently, the favored approach is the Regge Model developed by Vanderhaeghen, Guidal and Laget [109, 110]. The data extracted for $F_\pi(s < 0)$ have thus improved in time but remain unavoidably model-dependent. These data samples have

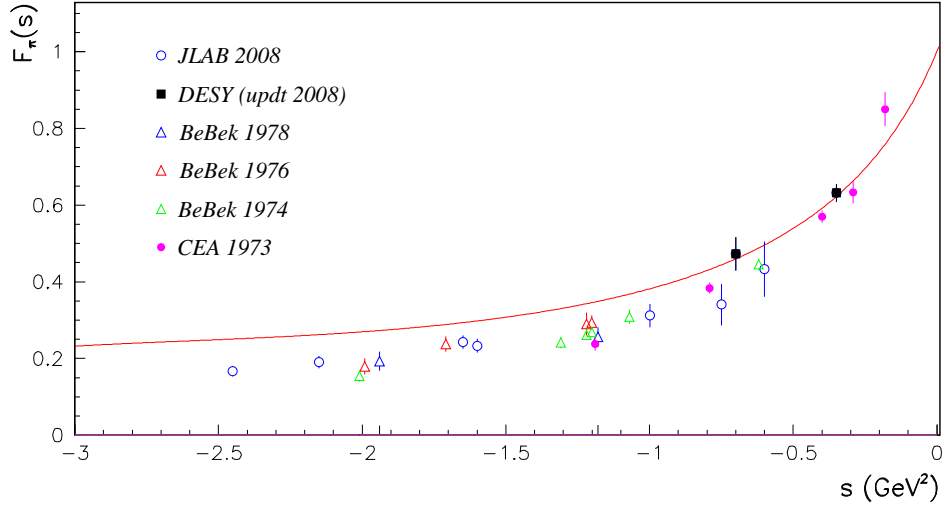


Figure 7: The pion form factor in the spacelike region; the curve displays the function $F_\pi(s)$ coming from our global fit of the timelike data and of the spacelike data from NA7 [47] and Fermilab [93]. The (unfitted) data flagged by JLAB and DESY are extracted from [99], the other can be found in [95]. See also Figure 6.

not been included in our fitting approach, but simply compared with the extrapolation of our fit function at $s < 0$, a pure prediction below $s \simeq -0.25 \text{ GeV}^2$.

In Figure 6, besides the fitted data from NA7 and Fermilab, one has displayed the (*unfitted*) data from the DESY experiments [100, 101] and the lowest photon virtuality data collected at Jefferson Lab by the F_π Collaboration. The data points flagged by JLAB 2008 and DESY have been extracted from the latest – to our knowledge – publication of the F_π Collaboration [99]. One can observe that the updated [99] DESY data points fall exactly on the $F_\pi(s)$ function derived from a fit using also the NA7 [47] and Fermilab [93] data. The three JLab plotted data points are found systematically below the fit function; however, most of these JLab data points can also be found in a previous JLab publication [96]. The difference between the values in [99] and [96] seems mostly coming from using different extraction methods of $\sigma_L(Q^2)$ [97]. The data points from [96] seem in closer agreement with the continuation of our $F_\pi(s)$ than the estimates given in [99]. They are also in better agreement with what can be expected from the DESY data points as updated in [99]; this updating seems to deal with the extraction of F_π from the longitudinal cross section σ_L . The behavior of (the extrapolated) $F_\pi(s)$ beyond -1 GeV^2 is shown in Figure 7 together with the other reported data.

The content of Figure 6 gives a hint that the extrapolation of the BHLS₂ $F_\pi(s)$ could well be valid down to $s \simeq -1 \text{ GeV}^2$. This also reflects a ρ dominance well inside the non-perturbative spacelike region. This dominance is illustrated by fit properties : When fitting the pion space-like data, beside the ρ contribution, the fit function contains also those from the ω and ϕ mesons; the fit returns $\langle \chi^2 \rangle / N = 55/59$; however, computing the χ^2 distance of the fit function

amputated from the ω and ϕ contributions to the *pion* data from NA7 and Fermilab, one obtains $\langle \chi^2 \rangle / N = 56/59$. This indicates that the (tiny) contributions of the ω and ϕ mesons introduce a (tiny) noise and that nothing else than the ρ contribution is actually required.

This ρ dominance phenomenon does not happen for the kaon form factor as, truncating the prediction for $F_K(s)$ from its ω and ϕ contributions returns a disastrous χ^2 distance; for instance, the full χ^2 distance of the NA7 kaon data to $F_K(s)$ which is $\simeq 14$, becomes $\simeq 2300$ when $F_K(s)$ is amputated from its ω and ϕ contributions. Such property is quite unexpected as the parametrization for the ω and ϕ [25], reminded in Section 9, is nothing but a Breit-Wigner lineshape modified in such a way that the inverse propagators fulfill $D_V(0) = -m_V^2$, these HK masses being those in Equations (26). That the analytic continuation, over more than $\simeq 1$ GeV^2 , of such a simple parametrization, with parameter values fixed at the ϕ mass, can provide a good description of the existing kaon spacelike data may look quite amazing.

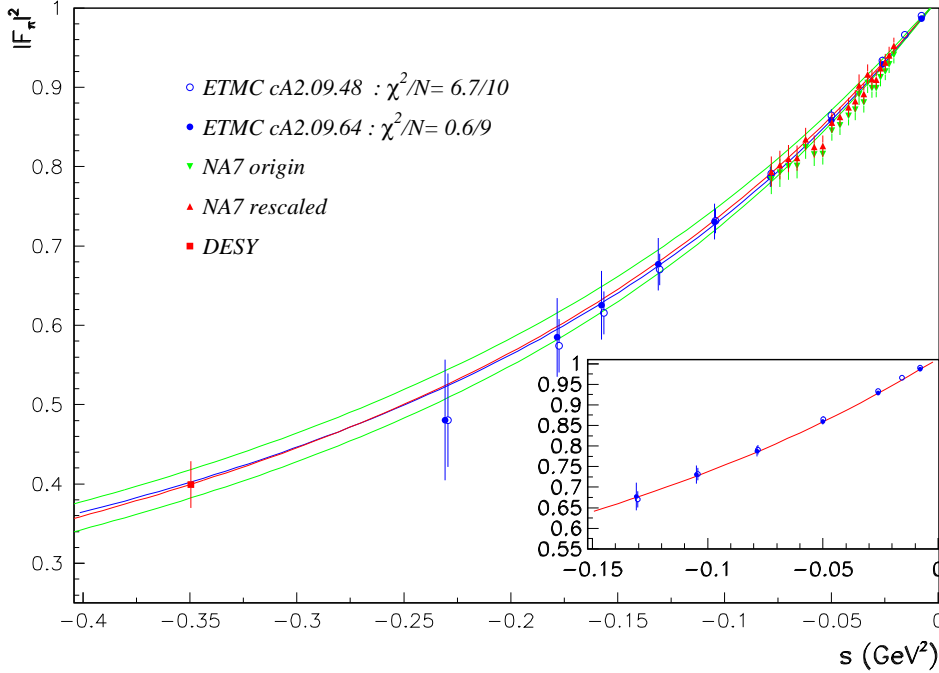


Figure 8: The red curve is $|F_\pi(s)|^2$ derived from our global fit, the blue curve is the HPQCD parametrization and the green curves display this parametrization at $\pm 1\sigma$ of the central value for their $\langle r_\pi^2 \rangle$. The LQCD spectra from ETMC and the experimental data shown are commented in Subsection 18.3; the LQCD spectra and the data point from DESY is not fitted. The inset magnifies the threshold behavior of the predicted form factor with the ETMC data *superimposed* (not fitted).

18.3 The Pion Form Factor : The Lattice QCD Data

Some Collaborations have published information on the pion form factor derived from Lattice QCD (LQCD) data at pion masses close to the physical pion mass value [3]. We compare these LQCD form factors to our fit function $F_\pi(s < 0)$ which, already, fairly well describes the accurate NA7 experimental data as obvious from Figure 6 and Tables 3 or 4.

The HPQCD Collaboration has thus produced a parametrization³⁶ of the pion form factor [111] $F_\pi(Q^2)$ for virtualities in the range $Q^2 \in [-0.1, 0.0]$ GeV². In order to perform a numerical comparison with our fit $F_\pi(s < 0)$, we have plotted their pole parametrization, setting the lattice spacing a at zero and using their pion radius squared $\langle r_\pi^2 \rangle = 0.403(18)(6)$ fm². In Figure 8, our fit function for $F_\pi(s < 0)$ is shown by the red curve; the blue curve is the HPQCD parametrization at the central value for $\langle r_\pi^2 \rangle$. The red and blue curves are clearly very close to each other, if not overlapping. The green curves display the HPQCD parametrization with $\langle r_\pi^2 \rangle$ at $\pm 1\sigma$ from its central value. This indicates that the LQCD parametrization [111] is in fair agreement with the BHLS₂ fit function $F_\pi(s < 0)$ much beyond the expected HPQCD range of validity and validated by the DESY data points [100, 101]; Figure 8 clearly shows that the agreement between HPQCD [111] and BHLS₂ extends to the *prediction*, shown in this Figure by the green curve, derived when fitting with discarding the spacelike data.

Six spectra for $F_\pi(Q^2)$ have been published by the ETM Collaboration [112]; two of them correspond to a pion mass close to its physical value, namely the gauge ensembles *cA2.09.48* and *cA2.09.64*. These spectra are given by the form factor values $F_\pi(Q^2)$ and uncertainties as functions of Q^2/M_π^2 . In order to compare with phenomenology and experimental data, one has to restore the values for Q^2 from the provided values for Q^2/M_π^2 . Ref. [113], which sketches the generation of these ensembles, indicates that, numerically, $M_\pi \simeq 134.98$ MeV, almost identical to the RPP π^0 mass.

Figure 8 shows the $|F_\pi(Q^2)|^2$ spectra derived from the *cA2.09.48* and *cA2.09.64* ensembles in [112]. They are displayed with their reported statistical errors³⁷. The χ^2 distances³⁸ of *cA2.09.48* and *cA2.09.64* to the BHLS₂ form factor squared $|F_\pi(s)|^2$ have been computed, assuming the systematics negligible compared to the statistical errors [112]; they are displayed inside Figure 8. One can remark that the average χ^2 distance per datum is 0.67 for *cA2.09.48*, quite a good value for data outside the fit procedure; it is only 0.06 for the *cA2.09.64* form factor. This can be considered as an independent confirmation concerning the smallness of the systematics versus the statistical errors for the considered ETM spectra.

Stated otherwise, the data points of the *cA2.09.64* form factor are almost exactly on the fit function. Out of curiosity, we have redone the fit in the RS variant of BHLS₂ discarding the spacelike experimental data in order to get, online, the predicted form factor for any $s < 0$ *using only timelike data*; the average χ^2 distances become 0.59 and 0.10 for resp. *cA2.09.48*

³⁶We thank L. Lellouch for having drawn our attention to this paper.

³⁷It is worth noting that the original (unscaled) NA7 stay *below* the ETM data in the spectrum range where they are the most precise; this should be compared with Figure 6 in [112], especially its right panel, which exhibits the same trend.

³⁸Reference [112] does not give special information about systematics and performs its own fits using uncorrelated χ^2 's. So, following this line, we define the χ^2 distance of the ETM data to our prediction by the sum of squared terms d_i^2 where : $d_i = (F_{ETM}(Q_i^2) - F_{BHLS_2}(Q_i^2))/\sigma_{ETM}(Q_i^2)$, using obvious notations. The quantity $\sum d_i^2$ is *not* submitted to the minimization procedure.

and $cA2.09.64$. So, the χ^2 distance of the ETM samples to the $BHLS_2$ prediction indicates that the form factor lineshape is quite consistent with LQCD expectations; the inset in Figure 8, by magnifying the energy region close to the chiral point, illustrates the tight agreement of the prediction and of the ETM data. In other words, the ETM spectra provide strong support to the $BHLS_2$ fits; this $BHLS_2$ model spectrum is also intimately related to the dealing with the reported correlated systematics as promoted in [27].

For illustration, one has also displayed in Figure 8 the closest among the two data points from DESY and a part of the NA7 spectrum rescaled *and* not rescaled. As expected from their χ^2 distances to the fit function, the ETM spectra are observed closer to the rescaled NA7 spectrum than to the original one.

18.4 The Neutral Kaon Form Factor at $s < 0$

As seen in the previous Subsections, $BHLS_2$ predicts the charged pion and kaon form factors in the close spacelike region with fair accuracy. Likewise, $BHLS_2$ also predicts the neutral kaon form factor $F_{K0}(s)$; it is displayed in Figure 9. This is the analytic continuation of the form factor given in Subsection 11.4 and numerically determined within the fit procedure by the $e^+e^- \rightarrow K_L K_S$ annihilation data. One clearly observes a behavior quite different of those for $F_{K^\pm}(s)$, with a negative slope down to almost $s = 0$, when coming from the spacelike region.

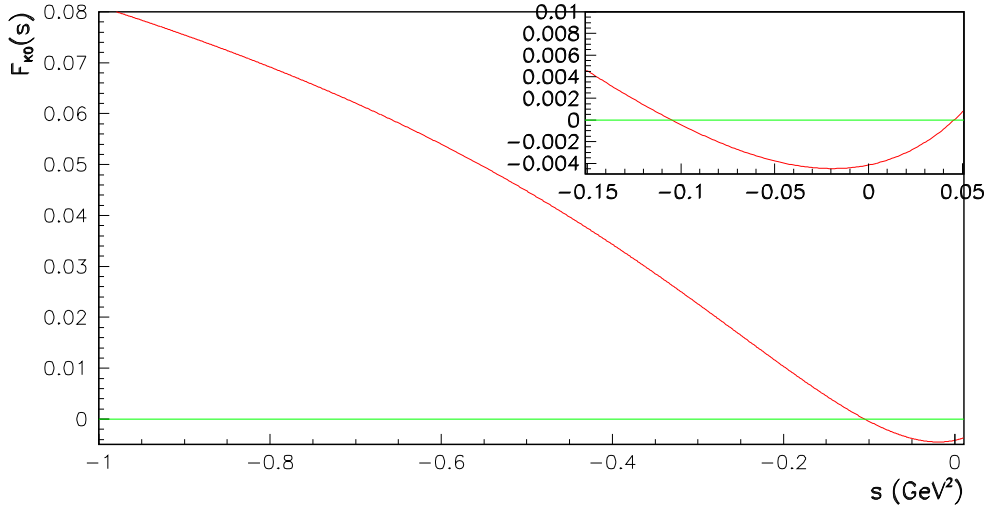


Figure 9: The neutral kaon electromagnetic form factor predicted by $BHLS_2$: The function is computed at the central value of the fit parameters.

Actually, as already stated in Section 9 one has $F_{K0}(s = 0) = 0$ up to contributions of second order in breaking parameters. What is displayed in Figure 9 is $F_{K0}(s)$ computed at the fitted

central value of the fit parameters³⁹. To take into account their uncertainties, a Gaussian Monte-Carlo has been run which returns the averaged central value $F_{K^0}(0) \simeq 10^{-6}$ or less, depending on the fit conditions. This indicates that the negative excursion close to zero observed in Figure 9 could well be a numerical artifact.

	$\langle r_{\pi^\pm}^2 \rangle$	$\langle r_{K^\pm}^2 \rangle$
BHLS ₂ fit	$0.430 \pm 0.002_{\text{mod}} \pm 0.001_{\text{fit}}$	$0.268 \pm 0.004_{\text{mod}} \pm 0.001_{\text{fit}}$
NA7 [47, 48]	0.439 ± 0.008	0.40 ± 0.11
Fermilab [93, 94]	0.439 ± 0.030	0.28 ± 0.05
CHS [114]	$0.429 \pm 0.001_{\text{stat}} \pm 0.004_{\text{syst}}$	—
ACD [115]	0.432 ± 0.004	—
ChPT 2 flavors [116]	0.437 ± 0.016	—
ChPT 3 flavors [117]	0.452 ± 0.013	0.363 ± 0.072
HPQCD [111]	$0.403 \pm 0.018_{\text{stat}} \pm 0.006_{\text{syst}}$	—
ETM [113]	$0.443 \pm 0.021_{\text{stat}} \pm 0.020_{\text{syst}}$	—

Table 5: Pion and kaon charged radii in units of fm². See also [118] for additional LQCD evaluations of $\langle r_{\pi^\pm}^2 \rangle$.

As for the charge radius squared of the neutral kaon, both BS and RS variants of BHLS₂ return an average value :

$$\langle r^2 \rangle_{K^0} = 0.00 \pm 0.10 \text{ fm}^2 \quad (99)$$

consistent with all reported measurements, in particular, those of the NA48 Collaboration [102] ($\langle r^2 \rangle_{K^0} = -0.090 \pm 0.021 \text{ fm}^2$), or those of KTeV [103] ($\langle r^2 \rangle_{K^0} = -0.077 \pm 0.007_{\text{stat}} \pm 0.011_{\text{syst}} \text{ fm}^2$). It also agrees with the ChPT result obtained by Bijmens and Talavera [117] ($\langle r^2 \rangle_{K^0} = -0.042 \pm 0.012 \text{ fm}^2$) and with the former measurements collected in the Review of Particle Properties [3]. We don't know about predictions for $F_{K^0}(s < 0)$ at larger virtualities to which one could compare.

18.5 Pion and Kaon Charge Radii

The fit parameter central values and the parameter error covariance matrix can serve to generate several samplings ($\alpha = 1, \dots, n$) and, for each, the corresponding pion and kaon form factors $F_P^\alpha(s)$. These can be used to evaluate derived physics quantities by computing

³⁹This is equivalent to performing only one sampling on the multidimensional error covariance matrix of the fitted parameters.

the average and the r.m.s. values of the various estimates obtained from the set $\{F_P^\alpha(s), \alpha = 1, \dots, n\}$.

Among the relevant physical properties of the pion and kaon form factors, their behavior close to $s = 0$ deserves special interest. As clear from Section 11, the charged pion and kaon vector form factors are analytic functions of s and, so, can be expanded in Taylor series around the origin. Neglecting terms of degree higher than 2 in s , one can write :

$$F_P(s) = a_P + b_P s + c_P s^2, \quad P = \pi^\pm, K^\pm, \quad (100)$$

where the a_P 's are expected equal to 1 (up to second order terms in breakings) and the b_P 's are related with the so-called charged radii by $b_P = \langle r_P^2 \rangle / 6$ for which several values have been reported.

In order to have a reasonable lever arm, one has chosen a s interval extending on both sides of $s = 0$ and bounded⁴⁰ by $\pm 0.05 \text{ GeV}^2$. Using the values of each $F_P^\alpha(s)$ at three s values $(0, \pm 0.05) \text{ GeV}^2$, one constructs the sets $\{[a_P^\alpha, b_P^\alpha, c_P^\alpha], \alpha = 1, \dots, n\}$, and derives their averages and r.m.s.'s. Working within the RS variant of BHLS₂ and using the largest set of experimental data samples, one derives :

$$b_\pi = [1.840 \pm 0.003] \text{ GeV}^{-2}, \quad c_\pi = [4.155 \pm 0.054] \text{ GeV}^{-4}, \quad (101)$$

and :

$$b_K = [1.159 \pm 0.005] \text{ GeV}^{-2}, \quad c_K = [1.15 \pm 0.24] \text{ GeV}^{-4}. \quad (102)$$

As it is more customary to express the slope term in units of fm^2 , one displays our values together with external information in Table 5. Our results are given with two uncertainties; one is derived from the sampling on the error covariance matrix and is indexed by "fit". One has also varied the content of the data sample set submitted to the global fit and compared the results to those derived with the maximal sample set. It is observed that the central values for $\langle r_{\pi^\pm}^2 \rangle$ and $\langle r_{K^\pm}^2 \rangle$ get shifted while the uncertainties are almost unchanged. One has also switched from the RS to the BS variant of BHLS₂; in this case, the central values get marginally shifted. Merged together, these shifts contribute an uncertainty denoted "mod" for "model" which, however, reflects as much the (weak) tensions between the various data samples of the largest sample set – defined in Section 17 – than the model properties by themselves.

As for $\langle r_{\pi^\pm}^2 \rangle$, Table 5 shows an agreement of our result with the experimental data from NA7 and Fermilab at the 1σ level or better. The result of G. Colangelo *et al.* [114] (CHS) is derived from a global fit of the timelike and spacelike pion form factor data based on a parametrization through the Omnès representation of $F_\pi(s)$ taking into account isospin breaking effects (ω) and prescriptions for the asymptotics of the $\pi\pi$ P -wave phase shift; this estimate is in perfect agreement with our own fit result. Using an elaborate method mixing the low energy $\pi\pi$ phase information and some form factor modulus information, B. Ananthanarayan *et al.* [115] recently derived the value flagged by ACD in Table 5 which is very close to ours. The two flavor result of J. Bijnens *et al.* [116] flagged as "ChPT 2 flavors" as well as the three flavor evaluation in [116] and the most recent Lattice QCD derivations of the HPQCD [111] and ETM [113] Collaborations are also in good correspondence with ours. Former LQCD evaluations for $\langle r_{\pi^\pm}^2 \rangle$ can also be found in Table 22 of [118].

⁴⁰ Considering the real part of $F_P(s)$ permits to avoid (minor) issues with the $\pi^0\gamma$ threshold effects.

As for the curvature term, varying the fit conditions as just indicated for $\langle r_{\pi^\pm}^2 \rangle$, one can assess the effects observed when switching from the RS to the BS variant of BHLS₂ and when modifying the set of data samples submitted to fit. Altogether, this leads to our final result :

$$c_\pi = [4.155 \pm 0.040_{\text{mod}} \pm 0.054_{\text{fit}}] \text{ GeV}^{-4} . \quad (103)$$

The 2 flavor ChPT estimate based on all data samples available at that time (1998), [116] reports $c_\pi = 3.85 \pm 0.60 \text{ GeV}^2$ and the 3 flavor evaluation [117] ($c_\pi = 4.49 \pm 0.28 \text{ GeV}^2$) look in fair agreement with the BHLS₂ evaluation given in Equation (103).

As the pion and kaon form factors, in the close spacelike region, are frequently parametrized by a pole expression :

$$F_P(s) = \frac{1}{1 - b_P s} , \quad P = \pi^\pm, K^\pm , \quad (104)$$

we performed alike without, however, introducing additional normalization factors as commonly done as indeed we believe in the relevance of the absolute scale of the $F_P(s)$'s returned by the BHLS₂ fits. Such a parametrization turns out to impose the constraint $c_P = b_P^2$ to the curvature term. This leads to : $\langle r_{\pi^\pm}^2 \rangle = 0.424 \pm 0.002_{\text{mod}} \pm 0.001_{\text{fit}}$ and $\langle r_{K^\pm}^2 \rangle = 0.268 \pm 0.003_{\text{mod}} \pm 0.001_{\text{fit}}$.

For what concerns $\langle r_{K^\pm}^2 \rangle$, the numbers reported in Table 5, show that our evaluation is at 1σ from the NA7 measurement [48] and coincides with those from [94]. As for the ChPT prediction from Bijmens and Talavera [117], it differs from the value returned by BHLS₂ at the 1σ level. There is no reported evaluation of the curvature term of the kaon form factor to which one could compare our own evaluation in Equations (102).

Therefore, concerning the low energy behavior of the pion and kaon form factors, the overall picture is a fair agreement of BHLS₂ with the corresponding experimental measurements as well as with the existing LQCD and ChPT evaluations.

19 The Isospin 1 P -wave $\pi\pi$ Phase Shift

Another relevant piece of information is the $I = 1$ dipion P -wave phase shift δ_{11} . This physics has not been included within our HLS frameworks⁴¹; nevertheless, a comparison of the P -wave $\pi\pi$ phase shift extracted from BHLS/BHLS₂ with other sources provides an additional cross check.

Both panels of Figure 10 display the experimental data collected by the CERN-Munich Collaboration [119], the phase shift derived using the Roy Equations [120] and the phase shift derived in [43] in the context of a common fit of the $e^+e^- \rightarrow \pi^+\pi^-$ cross-section and of the dipion spectrum in the τ decay⁴². The phase shift coming from BHLS₂ is displayed in the top panel while the phase shift from the previous BHLS [25] is displayed in the bottom panel. Both

⁴¹A relative energy scale calibration issue between phase shift and annihilation data may have been identified [114], probably amplified by the steep rise of the phase in the interesting region, combined with a 20 MeV binning size for what concerns the CERN-Munich data [119].

⁴²Plots including other data [121] and the ChPT predictions [122] can be found in Figure 5 of [27]; they are not shown here in order to avoid overburdening Figure 10.

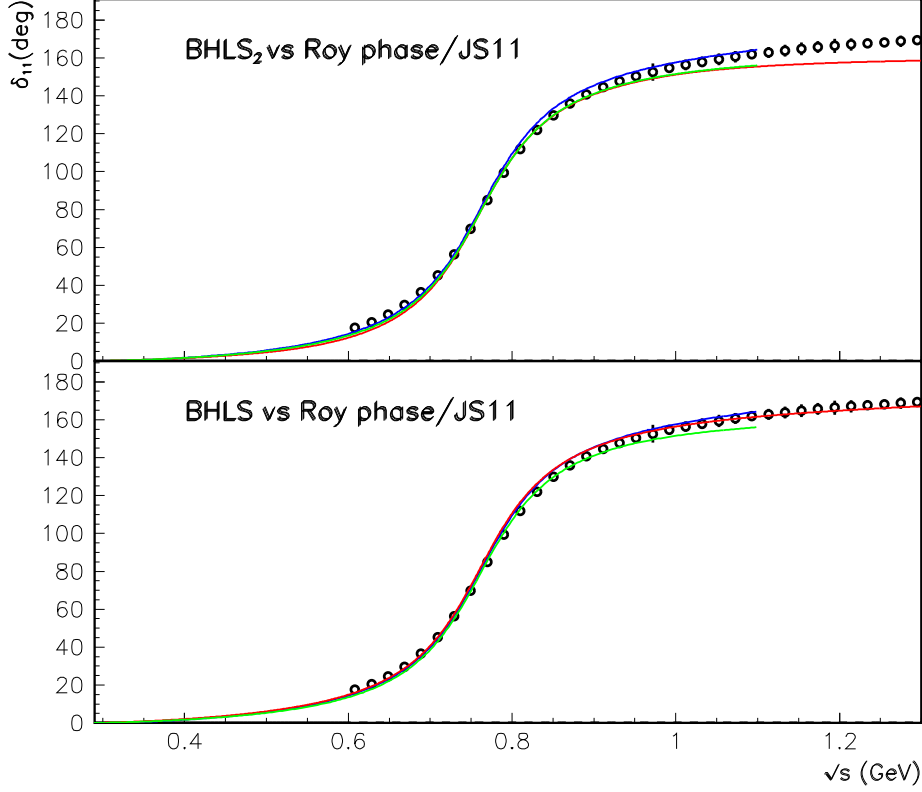


Figure 10: The δ_{11} $\pi\pi$ phase shift : In both panels, one displays the CERN-Munich data [119], the phase shift from [43] (JS11) is shown by the green curves and the blue curves are the phase shift from [120] based on the Roy Equations. The red curves display the predictions from BHLS₂ (top panel) and from BHLS [25, 27] (bottom panel) using the pion form factor amplitude amputated from its ω and ϕ contributions.

HLS based phase shifts displayed correspond to the phase of the pion form factor amplitude amputated from the ω and ϕ terms (see Equation (57)) to meet the usual definition of the $I = 1$ P -wave $\pi\pi$ phase shift [120, 43]. The full (*i.e.* non amputated) BHLS/BHLS₂ pion form factor phases are visually identical to the ones displayed in Figure 10 except for additional tiny blips in the ω and ϕ energy regions as can also be seen in Figure 5 of [27].

In the case of BHLS₂ (red curve in the top panel of Figure 10), the phase shift superimposes almost exactly on the data points [119] and onto the JS11 curve up to the ϕ mass region. For this comparison with the external theoretical expectations [120, 43], one should cancel out the ω and ϕ terms from the pion form factor $F_\pi^e(s)$ given in Equation (57) as, indeed, these expectations do not carry such signals; one should remind that, within the BHLS/BHLS₂ frameworks, these signals are generated via the mixing angles $\alpha(s)$ and $\beta(s)$ (see Equations (58)) which are

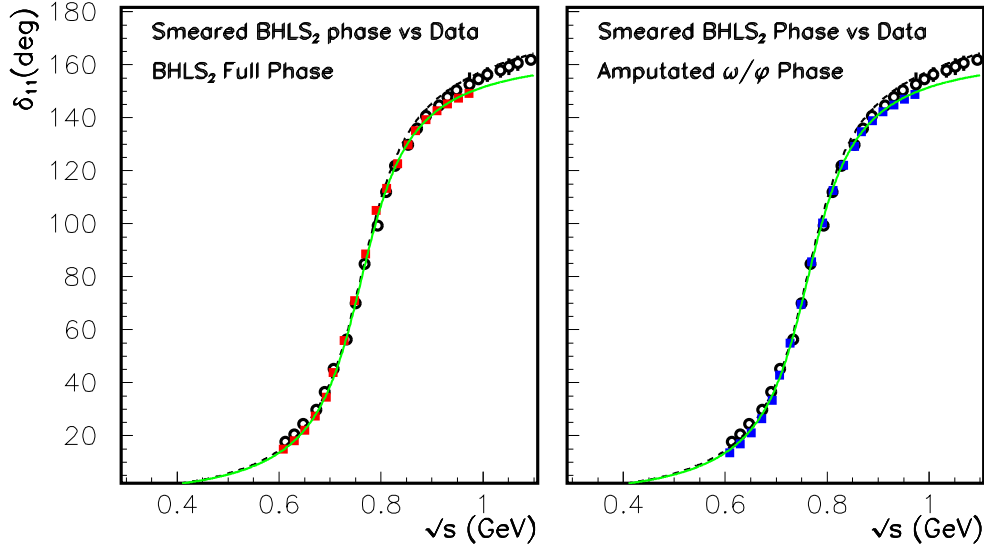


Figure 11: BHLS_2 δ_{11} $\pi\pi$ phase shift versus data [119] : The empty black circles display the experimental data points, the red (left panel) and blue (right panel) square symbols show the smeared BHLS_2 phase as indicated in the respective panels. The green full line represents the JS11 phase shift [43] while the black dashed line is the classical phase shift from [120].

proportional to the charged and neutral kaon loop difference and this vanishes in the isospin symmetry limit of equal kaon masses.

This argument might not fully apply when comparing the BHLS_2 phase to the experimental data [119]. However, the CERN–Munich Collaboration reported [123] a tiny $\rho^0 - \omega$ mixing effect – actually insignificant (see Table 1 in this Reference) – in the [119] phase shift data. Nevertheless, let us quickly consider this aspect of the experimental phase shift for completeness.

For a well-grounded comparison between the BHLS_2 phase and the CERN–Munich data, one should rather use the BHLS_2 phase smeared out over the experimental (20 MeV) bin width. The purpose of Figure 11 is to display the smeared BHLS_2 phase together with the CERN–Munich data [119]. In its leftmost panel the smeared BHLS_2 phase plotted is those of the full pion form factor $F_\pi^e(s)$ just as given in Equation (57); in the rightmost panel, the smeared BHLS_2 phase is those of the (ω/ϕ) -amputated $F_\pi^e(s)$. In both panels, the CERN–Munich data points are also plotted but their symbols generally vanish underneath those for the smeared BHLS_2 data. One clearly observes a good agreement between BHLS_2 and the CERN–Munich data up to the ϕ mass region. Comparing the phase shift of the full and amputated BHLS_2 pion form factors as displayed in Figure 11 clearly shows that the effects of the ω and ϕ signals on δ_{11} is quite marginal as expected from the [123] analysis.

In a large energy interval (about $\simeq 200$ MeV wide) centered on the ω mass, the 3 curves for

the BHLS/BHLS₂, Roy and JS11 phase shifts overlap within the thickness of the curves and, so, it is impossible to distinguish any one from each other. Then, both JS11 and BHLS₂ start to depart from the data increasingly with increasing energies. Put together with the remarks already stated about the behavior of the dikaon cross sections slightly above the ϕ mass, this gives a hint for an onset of higher mass vector mesons presently not accounted for in the HLS framework.

Thus, the agreement between the BHLS/BHLS₂ predictions on the one hand and the theoretical expectations [120, 43] and the CERN-Munich data on the other hand, looks quite satisfactory⁴³.

One should also note that the bottom panel in Figure 10 exhibits a fair agreement with the data much above the validity range of the BHLS model (the ϕ mass region); this can be traced back to having allowed the pion loop in the $V - \gamma$ transition amplitude F_ρ^e and in the ρ self-mass amplitude to carry different subtraction polynomials (see Subsection 11 above). This clearly accounts for the onset of the high mass vector mesons as the agreement remains valid up to 1.3 GeV and somewhat above.

20 Lagrangian Parameter Values in BHLS and BHLS₂

Table 6 reports on the Lagrangian parameter values⁴⁴ derived when running BHLS with updated kaon data (first data column). Running the basic variant BS of BHLS₂ with τ data discarded gives parameters values displayed in the second data column, while the third data column reports on the numerical results from the BHLS₂ Reference Solution (RS) using the largest set of consistent data samples.

Clearly, the Lagrangian parameters common to the various modelings cover a wide range of values; this does not prevent the fit properties (reminded in the last two data lines) to always exhibit a fairly good description of the data.

20.1 The $(z_V \div a)$ and $(\Sigma_V \div a)$ Anticorrelations within BHLS₂

The value obtained for z_V from fitting with the RS variant of BHLS₂ may raise questions – see Section 8 – as $z_V - 1$ is numerically large⁴⁵, even larger than $z_A - 1$. For this purpose, it has been worthwhile to explore the RS variant behavior in fits performed discarding the 3π final state data; this has revealed a numerical anticorrelation between the HLS parameter a and the BKY breaking parameter z_V , undetectable in the parameter error correlation matrix as $\langle \delta a \delta z_V \rangle \simeq -0.24$. Likewise, but of less concern, one observes a similar numerical anticorrelation between a and Σ_V as $\langle \delta a \delta \Sigma_V \rangle \simeq -0.18$. Several solutions with comparable total χ^2 were found and the most striking difference among them just concerns the values for

⁴³As illustrated in Figure 2 of [124] the solution of the Roy equation requires a normalization of the energy scale at about 1 GeV. In the BHLS approach, one could adjust $g_{\rho\pi\pi}$ to get a better agreement for the high energy tail of the Roy solution.

⁴⁴The full list of parameter values and uncertainties, especially the subtraction polynomial coefficients, are not given; they can be provided upon request.

⁴⁵ Even if only a 2.4ϵ effect, referring to the numerical estimate for generic ϵ 's given in Footnote 6.

Channels	BHLS [25] (model B)	BHLS ₂ (BS) (no τ)	BHLS ₂ (RS) (z_V free)	BHLS ₂ (RS) ($z_V \equiv 1$)
a_{HLS}	2.620 ± 0.001	1.970 ± 0.002	1.590 ± 0.001	2.658 ± 0.002
g	5.570 ± 0.001	6.855 ± 0.003	6.707 ± 0.002	6.702 ± 0.003
$(c_3 + c_4)/2$	0.886 ± 0.003	0.762 ± 0.003	0.756 ± 0.003	0.755 ± 0.003
$c_1 - c_2$	1.130 ± 0.022	0.771 ± 0.020	0.833 ± 0.021	0.789 ± 0.018
$10^2 \times z_3$	\times	-0.373 ± 0.004	-0.424 ± 0.003	-0.428 ± 0.003
z_A	1.57 ± 0.01	1.55 ± 0.01	$1.55 \pm .01$	$1.48 \pm .01$
z_V	1.204 ± 0.001	1.403 ± 0.002	1.674 ± 0.002	1.00
$10^2 \times \Delta_A$	1.955 ± 0.517	0.11 ± 0.51	0.83 ± 0.51	0.82 ± 0.50
$10^2 \times \Sigma_V$	-15.63 ± 0.06	-7.69 ± 14.8	10.42 ± 0.15	-34.53 ± 0.09
$10^2 \times \xi_0$	\times	-6.40 ± 0.04	-3.60 ± 0.03	-1.85 ± 0.04
$10^2 \times \xi_3$	\times	2.34 ± 0.16	2.92 ± 0.15	2.02 ± 0.080
$10^2 \times \psi_0$	\times	\times	-3.91 ± 0.27	-4.24 ± 0.24
$10^2 \times \psi_\phi$	\times	\times	-0.80 ± 0.09	-0.63 ± 0.09
$10^2 \times \psi_\omega$	\times	\times	-3.20 ± 0.11	-3.39 ± 0.12
χ^2/N_{pts}	949.1/1056	1054/1152	1133/1237	1137/1237
Probability	96.7%	93.9 %	93.3%	92.4%

Table 6: Model parameter values in BHLS and in the BS and RS variants of BHLS₂ ; second line in the Table title indicates the running conditions for what concerns the data samples submitted to fit. The last lines display the χ^2 , N_{pts} and the probability of the fits.

a , z_V and Σ_V . This is well illustrated by the three following parameter sets :

$$\left\{ \begin{array}{l} a = 2.340 \pm 0.003, \quad z_V = 1.122 \pm 0.003, \quad \Sigma_V = -0.272 \pm 0.001, \quad \chi^2/N_{\text{pts}} = 981.2/1079 \\ a = 2.083 \pm 0.003, \quad z_V = 1.266 \pm 0.005, \quad \Sigma_V = -0.182 \pm 0.001, \quad \chi^2/N_{\text{pts}} = 981.5/1079 \\ a = 1.606 \pm 0.001, \quad z_V = 1.653 \pm 0.002, \quad \Sigma_V = +0.068 \pm 0.002, \quad \chi^2/N_{\text{pts}} = 983.5/1079 \end{array} \right. \quad (105)$$

which exhibit clear anticorrelations between the numerical values for a and z_V on the one hand and for a and Σ_V on the other hand. Despite the large variations of each of a , z_V and Σ_V , the ranges covered by the central values for az_V and $a(1 + \Sigma_V)$ are much narrower than those for a , z_V and Σ_V ; indeed, one obtains $az_V = (2.63 \div 2.66)$ and $a(1 + \Sigma_V) = (1.70 \div 1.72)$, *i.e.* both products exhibit spreads at not more than the percent level.

In order to track back the source of these anticorrelations, it is worth considering the $\rho^0\pi^+\pi^-$ and $\phi K\bar{K}$ couplings. These are given by (see Appendix A) :

$$g_{K\bar{K}}^\phi = \mp [az_V] \frac{g\sqrt{2}}{4z_A} \left(1 \pm \frac{\Delta_A}{4}\right) (1 + \xi_0) \quad \text{and} \quad g_{\pi^+\pi^-}^{\rho^0} = [a(1 + \Sigma_V)] \frac{g}{2} (1 + \xi_3). \quad (106)$$

which exhibit the dependences upon $[az_V]$ and $[a(1 + \Sigma_V)]$.

On the other hand, given the measured cross sections for $e^+e^- \rightarrow \pi^+\pi^-$ and $e^+e^- \rightarrow K\bar{K}$, the observables $\Gamma(\rho^0 \rightarrow e^+e^-) \times \Gamma(\rho^0 \rightarrow \pi^+\pi^-)$ and $\Gamma(\phi \rightarrow e^+e^-) \times \Gamma(\phi \rightarrow K\bar{K})$ should be weakly model/parameter dependent within *successful* (global) fits. Substantially, these products are the squares of $H_\rho = |F_{\rho\gamma}^e(m_{\rho^0}^2) g_{\pi^+\pi^-}^{\rho^0}|$ and $H_\phi = |F_{\phi\gamma}^e(m_\phi^2) g_{K\bar{K}}^\phi|$, the $F_{V\gamma}^e(s)$'s being given by Equation (61); these quantities stretch ranges of the order $\pm 3\%$ only : $H_\rho = 0.753 \div 0.803$ and $H_\phi = 0.124 \div 0.136$. So, as the fits reported by Equations (105) are successful, they all reproduce successfully the resonance peak values for the $e^+e^- \rightarrow \pi^+\pi^-$ and $e^+e^- \rightarrow K\bar{K}$ cross sections, which implies that the products az_V and $a(1 + \Sigma_V)$ weakly vary within different fits, even if each of these parameters scans a wider interval⁴⁶.

One has also run the BHLS₂ RS variant by fixing $z_V = 1$ and found the results shown in the last data column of Table 6. The 6 units difference between the minimum χ^2 obtained fixing $z_V = 1$ and the best fit leaving z_V free is almost entirely concentrated in $\chi^2(e^+e^- \rightarrow 3\pi)$ which becomes 146.3 (compared to 140.4 for 158 data points). Running also the BHLS₂ RS variant imposing via MINUIT, a lower bound $a \geq 2$ returns :

$$a = 2.0 \pm 0.001, \quad z_V = 1.330 \pm 0.001, \quad \Sigma_V = -0.128 \pm 0.001, \quad \chi^2/N_{\text{pts}} = 1133.2/1237. \quad (107)$$

This fit also returns $az_V \simeq 2.66$ and $a(1 + \Sigma_V) \simeq 1.75$ and shows fairly good quality (93.6% probability). Moreover, all solutions return consistent information about the physics observables as will be exemplified below. Therefore, the relatively large value for $z_V - 1$ obtained in the best fit with the (unconstrained) RS variant of BHLS₂ is not a real issue. One should also note that the multiplicity of solutions reflected by Equations (105) reduces to a single one once the 3-pion data are accounted for.

⁴⁶ The other parameters involved in the expressions for $g_{K\bar{K}}^\phi$ and $g_{\pi^+\pi^-}^{\rho^0}$ – *i.e.* g, Δ_A, z_A and the ξ 's – undergo variations at the percent level or better.

20.2 A Remark on the HLS Parameter a

Correlated with the remark on z_V , one should note the value for the standard HLS model parameter a coming out of the best RS fit : 1.590 ± 0.001 . This is much smaller than any of its previous determinations. One should also note the unexpected value for a naturally returned by the BS variant fit : $a = 1.970 \pm 0.002$, very close to 2 (see Table 6). Therefore, one may conclude that, within the BS variant of BHLS₂, breaking parameters supply the needed $\gamma\pi^+\pi^-$, γK^+K^- and $\gamma K_L K_S$ couplings which, otherwise, would vanish when the $a = 2$ constraint is imposed.

20.3 The $\mathcal{O}(p^4)$ HLS Lagrangian : Effects of the Parameter z_3

The present work is the first one where a manifest and thorough use of the z_3 term from the $\mathcal{O}(p^4)$ HLS Lagrangian is performed; Appendix A.3 displays its full expression in the BHLS₂ context in terms of the ideal combinations of the vector fields. Actually, the existence of such a term was implicitly accounted for in the former BHLS [25] by disconnecting the subtraction polynomial for the $\gamma \rightarrow V$ transitions from the subtraction polynomials accompanying the pion and kaon loops occurring elsewhere – notably inside the ρ propagators.

Within the BHLS₂ framework, the loop corrections to the $\gamma \rightarrow V$ transition amplitudes and to the ρ^0 self-mass are tightly related⁴⁷ and additional terms of the form $c_{V\gamma} z_3 s$ come into play – see Equations (63).

Table 6 shows that z_3 is small but significant. As the $\gamma \rightarrow V$ transition amplitudes, where solely z_3 occurs, affect all the cross sections considered, the most appropriate way to examine its effects is to compare fits where z_3 is let free and fits performed by fixing $z_3 = 0$.

The overall picture coming from these fits is reported just below. To be concise, one denotes here by BHLS₂(z_3) and BHLS₂($z_3 = 0$) the RS based fitting framework running with resp. z_3 free and $z_3 = 0$.

- When all data and channels considered in this paper are used (the 3–pion channel is discarded, for simplicity), one gets $\chi^2(\text{BHLS}_2(z_3)/N_{data}) = 982/1079$ (93.1% probability), whereas $\chi^2(\text{BHLS}_2(z_3 = 0)/N_{data}) = 1049/1079$ (50.6% probability), a significant degradation.

A careful comparison of the fit results obtained in both cases shows that the partial χ^2 for the e^+e^- annihilation channels ($\pi^+\pi^-$, K^+K^- , $K_L K_S$, $\pi^0\gamma$, $\eta\gamma$ and even the τ dipion spectra) are comparable⁴⁸.

- The bulk of the degradation when going from BHLS₂(z_3) to BHLS₂($z_3 = 0$) is located in the account by the latter of the spacelike sector where the NA7 data impose accurate constraints, hardly absorbed by BHLS₂($z_3 = 0$).

Indeed, for the spacelike experimental data, the fit performed with BHLS₂($z_3 = 0$) returns $\chi^2(\text{spacelike } \pi)/N_{data} = 78/59$ and $\chi^2(\text{spacelike } K)/N_{data} = 29/25$, whereas the corresponding numbers in the (standard) BHLS₂(z_3) framework are resp. 56/59 and 18/25, in perfect agreement with the information already reported in Table 4.

⁴⁷ Compare Subsection 11.3 and Appendix A.5.

⁴⁸ BHLS₂(z_3) remains, nevertheless, favored against BHLS₂($z_3 = 0$) in these channels.

To fully compare with the information reported in Table 4, a $\text{BHLS}_2(z_3 = 0)$ fit, based on only the timelike data (*i.e.* discarding the spacelike data), is useful as it provides the corresponding $\text{BHLS}_2(z_3 = 0)$ *predictions* for the spacelike sector.

This $\text{BHLS}_2(z_3 = 0)$ global fit has been performed and displays an improved fit quality, as $\chi^2(\text{BHLS}_2(z_3 = 0)/N_{\text{data}} = 939/995)$ (72.6% probability), nevertheless lower than those for $\text{BHLS}_2(z_3)$. The χ^2 distances of the π and K spacelike data to the corresponding $\text{BHLS}_2(z_3 = 0)$ *predictions* are $\chi^2(\text{spacelike } \pi)/N_{\text{data}} = 85/59$ and $\chi^2(\text{spacelike } K)/N_{\text{data}} = 30/25$.

These two numbers should be compared with the first data column in Table 4. So, the nice feature of $\text{BHLS}_2(z_3)$ which predicts accurately the spacelike data is lost with $\text{BHLS}_2(z_3 = 0)$.

One should note that, when $z_3 = 0$ is imposed, the effects accounted for by $z_3 \neq 0$ are absorbed by the vector mesons propagators⁴⁹; this is what degrades the continuation of the form factors to the spacelike region and, fitting the spacelike data, does not solve the issue.

Stated otherwise, a non-zero z_3 is the best way to treat simultaneously the spacelike and timelike data with high accuracy and comfortable fit probabilities. This may be considered as an evidence pointing toward the relevance of the $\mathcal{O}(p^4)$ terms; a range for z_3 can be proposed $z_3 = -([0.37 \div 0.42] \pm 0.003_{\text{fit}}) \times 10^{-2}$ for its first experimental determination.

20.4 Other Physics Results

As for other model parameters, focusing on BHLS and the RS variant of BHLS_2 :

- One may wonder that the value for the vector coupling g increases by more than 20% when going from BHLS to BHLS_2 , keeping good fit qualities. However, the relevant piece of information, closer to observables, being the coupling $g_{\pi\pi}^{\rho^0} = ag(1 + \Sigma_V)(1 + \xi_3)/2$, it is interesting to compare BHLS to the RS variant of BHLS_2 : BHLS returns $g_{\pi\pi}^{\rho^0} = 6.156 \pm 0.005$ while the full BHLS_2 fits gets $g_{\pi\pi}^{\rho^0} = 6.06 \pm 0.013$ in reasonable correspondence with each other.
- The parameters associated with the anomalous sectors show that⁵⁰ $(c_3 + c_4)/2$ yields comparable values with BHL and with BHLS_2 . However, for $c_1 - c_2$, the difference is large; in this case, however, one should remind that the so-called "model B" variant of BHLS excludes from the fit the 3π data in the ϕ mass region while the whole 3π spectra are considered within BHLS_2 and are well fitted.
- The values for z_A are also interesting as they are related with f_K . Indeed, one knows that [25] :

$$r = \frac{f_{K^\pm}}{f_{\pi^\pm}} = \sqrt{z_A} \left[1 + \frac{\Delta_A}{4} \right] .$$

⁴⁹For instance g jumps from $\simeq 7$ to $\simeq 10$ and the pion and kaon loop subtraction polynomials are severely modified.

⁵⁰In the present work, one assumes $c_3 = c_4$.

is still valid within the BHLS₂ framework. For this ratio, BHLS returns $r = 1.257 \pm 0.003_{fit}$, while the RS variant of BHLS₂ finds $r = 1.247 \pm 0.003_{fit}$. The systematic uncertainty has been estimated to ± 0.020 by varying the running conditions of the BHLS₂ fitting code⁵¹.

This result should be compared with the Review of Particle Properties [125] which recommends $r = 1.197 \pm 0.002 \pm 0.006 \pm 0.001$ and with the LQCD determination for $N_f = 2 + 1 + 1$ flavors [118] $r = 1.195 \pm 0.005$.

- The additional parameters introduced by the CD breaking and the Primordial Mixing are all found at the few percent level. The difference for ξ_0 and ξ_3 between the (full) RS variant and the BS variant should be noted; it may have to be revisited later on, when a complementary mechanism may allow one to absorb satisfactorily the τ data within the BS global fit procedure. This may also influence the 3π sector.

21 The muon LO-HVP Evaluation

BHLS₂ (or BHLS) fits provide the contributions of the various hadronic channels⁵² it covers to $a_\mu(\sqrt{s} \leq 1.05 \text{ GeV})$. An overview of the main results, obtained in different running conditions is given in Table 7. These have been derived by submitting to fit most of the data samples commented in Section 13 which define a set of consistent samples covering the six annihilations considered; altogether, these 6 channels and the 10 radiative meson decay partial widths represent 1237 data points.

21.1 Comparison of BHLS₂ Estimates for $a_\mu^{\text{HVP-LO}}$ with Others

Without going lengthily into detailed comparisons, it looks worthwhile to provide some elements. For instance, one can extract from Figure 3 in [27], values for $G = a_\mu^{\pi\pi}(0.630 < \sqrt{s} < 0.958 \text{ GeV})$; our updated estimate for G is $G(\text{BHLS}) = (355.59 \pm 0.58) \times 10^{-10}$, very close to its former evaluation (see Fig. 3 in [27]) while the numerical integration of the NSK+KLOE data was estimated $G(\text{exp}) = (356.67 \pm 1.69) \times 10^{-10}$; BHLS₂ gives⁵³ $G(\text{BHLS}_2) = (356.50 \pm 0.75) \times 10^{-10}$.

In a quite different theoretical context, the recent analysis [114], provides the estimate $G = a_\mu^{\pi\pi}(\sqrt{s} < 0.630 \text{ GeV}) = (132.5 \pm 0.4_{\text{stat}} \pm 1.0_{\text{syst}}) \times 10^{-10}$ while the BHLS gives $G(\text{BHLS}) = a_\mu^{\pi\pi}(\sqrt{s} < 0.630 \text{ GeV}) = (130.80 \pm 0.22_{\text{fit}}) \times 10^{-10}$. In the same region one also gets $G(\text{BHLS}_2) = a_\mu^{\pi\pi}(\sqrt{s} < 0.630 \text{ GeV}) = (130.03 \pm 0.18_{\text{fit}} + [{}^{+0.25}_{-0.15}]_{\text{syst}}) \times 10^{-10}$.

Reference [114] also provides $H = a_\mu^{\pi\pi}(\sqrt{s} < 1.0 \text{ GeV}) = (494.7 \pm 1.5_{\text{stat}} \pm 2.0_{\text{syst}}) \times 10^{-10}$ while the updated BHLS gives $H(\text{BHLS}) = (490.65 \pm 0.84_{\text{fit}}) \times 10^{-10}$ and BHLS₂ leads to $H(\text{BHLS}_2) = (490.75 \pm 0.90_{\text{fit}} + [{}^{+0.31}_{-0.26}]_{\text{syst}}) \times 10^{-10}$. The method in [114] and ours

⁵¹We made additional runs fixing $z_V = 1$ (see Table 6), including the CMD-3 dikaon data and, finally, varying also the running of α_{em} .

⁵²All along this Section, one may use interchangeably $a_\mu^{\text{HVP-LO}}$ or, preferably, a_μ to lighten writing; the context will be unambiguous.

⁵³As the $(0.630 < \sqrt{s} < 0.958) \text{ GeV}$ interval is relatively far from both the threshold and the ϕ mass regions, one could indeed expect similar results from BHLS and BHLS₂.

are different, but more importantly for this energy range, the dipion BaBar data included in the study [114] and discarded in ours, certainly contribute to the difference.

One may also compare the BHLS₂ results with others for the contribution to $a_\mu^{\text{HVP-LO}}(\pi^+\pi^-)$ from the energy region $(0.6 \leq \sqrt{s} \leq 0.9)$ GeV. KNT18 [71] gets $(369.41 \pm 1.32) \times 10^{-10}$ and CHS [114] $(369.8 \pm 1.3_{\text{fit}} \pm 1.3_{\text{syst}}) \times 10^{-10}$ using BaBar data at low energies. BHLS2 running with KLOE10/12, CMD-2, SND, BESIII and Cleo-c data in the $\pi^+\pi^-$ channel yields $(367.81 \pm 0.77) \times 10^{-10}$; replacing the KLOE10/12 data by the KLOE85 combination [70], one gets $(367.61 \pm 0.64) \times 10^{-10}$. So the observed effect from BaBar in this energy region amounts to $\simeq 2 \times 10^{-10}$. One also observes the gain on accuracy by using BHLS₂: A factor of 2 compared to [71], a factor of 3 compared to [114].

21.2 Estimates for $a_\mu^{\text{HVP-LO}}(\sqrt{s} \leq 1.05 \text{ GeV})$

In order to get the full contribution to $a_\mu^{\text{HVP-LO}}$ of the energy region up to 1.05 GeV, one should complement the contribution from the channels covered by BHLS/BHLS₂ by those of the channels presently outside this framework (4π , $2\pi\eta$, ...). The most recent evaluation of this quantity, estimated by direct numerical integration of data is :

$$10^{10} \times a_\mu(\text{non HLS}, \sqrt{s} \leq 1.05 \text{ GeV}) = 1.28 \pm 0.17 .$$

In view of model effect studies, it has been found motivated to update and correct the data samples submitted to the BHLS fit in the way stated in Section 13. One has thus derived the updated BHLS evaluations given in the first data column of Table 7; this supersedes the BHLS results formerly given in Table 4 of [27]. Differences between BHLS and the RS BHLS₂ variant for some channel contributions are observed and, *in fine*, $a_\mu(\text{HLS}, \sqrt{s} \leq 1.05 \text{ GeV})$ only increases by $\simeq 1 \times 10^{-10}$ while its uncertainty slightly decreases ($1.03 \rightarrow 0.92$, in units of 10^{-10}). An evaluation of possible additional systematics, specific of the BHLS modeling, has been performed and summarizes by [27] :

$$10^{10} \times \delta_{\text{syst}} a_\mu(\text{BHLS}) = \left[\begin{smallmatrix} +1.3 \\ -0.6 \end{smallmatrix} \right]_\phi + \left[\begin{smallmatrix} +1.4 \\ -0.0 \end{smallmatrix} \right]_{VNSB} + \left[\begin{smallmatrix} +0.0 \\ -0.9 \end{smallmatrix} \right]_\tau . \quad (108)$$

Each piece shown here was found to act by shifting the central value for a_μ rather than enlarging its uncertainty. The first term refers to the uncertainty in the treatment of the ϕ mass region in the 3-pion spectra, the second term takes into account the uncertainty on the $\pi\pi$ threshold behavior within BHLS (see Subsection 10.3 above and, especially, Figure 1); finally, the third piece reflects differences observed by running the BHLS fit procedure [25, 26] with the τ data included and excluded.

As already stated, the BHLS₂ modeling has been motivated by the aim to cancel out the first two sources of uncertainties reported in Equation (108) by a better understanding of the $s = 0$ region and a full account of the 3-pion data up to the ϕ region.

For this purpose, the three data columns in Table 7 referring to BHLS₂ show that :

- The evaluation for the various contributions to $a_\mu(\sqrt{s} \leq 1.05 \text{ GeV})$ derived using the BS and both RS variants of BHLS₂ carries differences at a few 10^{-12} level.
- Using the τ data has some effect. Indeed, Table 7 shows that running the RS variant of BHLS₂ including the τ data improves the uncertainty in the dipion channel by $\simeq 10\%$

while leaving the central value almost unchanged. This illustrates that the e^+e^- and τ data are not conflicting within the RS variant of BHLS₂.

Another property exhibited in Table 7 should be noted :

- Whereas the sum of the various contributions to a_μ derived using several variants of the BHLS₂ fit almost coincides with the estimate derived by direct integration of the data, the $\pi^+\pi^-$ contributions differ by 3.72 in units of 10^{-10} , a significant difference.

In the direct integration method, the normalization of each sample is the nominal one and *all* uncertainties participate to the definition of its weight in the combination with the other samples involved. Instead, in the global fit method, the absolute normalization uncertainty is treated specifically and in consistency for all the data samples involved in all the annihilation channels considered ($\pi\pi$, $K\bar{K}$, $\pi\pi\pi$ and $(\pi^0/\eta)\gamma$). It has been shown [27] that the iterative method which underlies the HLS global fit procedures gives unbiased results ⁵⁴.

Therefore, that values of definite contributions to a_μ may significantly depend on the method used to derive them is not totally unexpected. That the sum of them may almost coincide is, however, accidental⁵⁵.

The data update having been performed, BHLS and BHLS₂ have been run on the same data and, thus, the differences between their respective evaluations reflect modeling effects. One can also compare these differences to the numbers listed in Equation (108).

As shown by the various topics examined in Section 18, one can legitimately consider the $\pi^+\pi^-$ threshold region accurately treated. Therefore, the difference $494.08 - 493.73 = 0.35$ between the BHLS₂ and BHLS estimates for $a_\mu(\pi^+\pi^-, \sqrt{s} \leq 1.05 \text{ GeV})$ is a fairly well motivated evaluation of the unaccounted for nonet symmetry breaking effects within the BHLS framework; it is therefore justified to replace the former +1.4 estimate in Equation (108) by +0.35.

Table 3 shows that all variants of BHLS₂ take well into account the 3π annihilation data over the whole energy domain up to the ϕ mass region, the fit quality of the RS variant being noticeable. The difference between BHLS₂ and BHLS for this channel $\simeq 0.5 \times 10^{-10}$ is in the range expected from the estimate [27] reported by the first term in Equation (108). Nevertheless, the 0.06×10^{-10} difference for the 3π entry between the RS variant of BHLS₂ runnings including and excluding the τ data might be considered as additional systematics⁵⁶.

It is interesting to compare the outcomes from fits to the values derived by the direct integration of the same data sample set treated in the BHLS₂ framework. One may note that the sum of all HLS channel contributions differs from the fit expectations by only $\simeq 0.6 \times 10^{-10}$; however, this hides the fact that the dipion channel is fitted 3.7×10^{-10} smaller and the 3-pion channel is fitted 1.70×10^{-10} larger.

⁵⁴This is well reflected, in the present work, by the nice matching observed between the predicted pion form factor in the spacelike region and the NA7 and ETMC data.

⁵⁵ In this respect, it is worth noting that a quite similar behavior is observed in the comparison of the KNT18 and DHMZ17 data reported in [71]. Indeed, Table 5 herein shows that the estimated dipion contributions (based on the same data) differ by 3.40×10^{-10} , whereas the total sums giving the HVP-LO's differ by only 0.2×10^{-10} .

⁵⁶There might be a numerical effect reflecting the physics correlation between the $\pi^+\pi^-\pi^0$ annihilation channel and the τ spectrum due to their common ρ^\pm exchanges taking place in their intermediate states.

In summary :

$$10^{10} \times a_\mu(\text{HLS}, \sqrt{s} \leq 1.05 \text{ GeV}) = 571.98 \pm 1.20_{fit} \quad (109)$$

is the most conservative final BHLS₂ answer, where the uncertainty collects statistical and systematic errors as reported by the various experiments. The remarks just stated concerning the 3-pion channel allows to keep an additional uncertainty of -0.06×10^{-10} , playing as a bias.

The issue is to examine whether more significant additional sources of systematics are not at work. For this purpose, the consequence on $a_\mu(\text{HLS})$ of the various fits referred to in the previous Section carry a relevant piece of information, as also for the fits underlying the results given in Equations (105) and (107) or those displayed in the last data column in Table 6. These fits, covering a wide range of parameter values, are relevant for systematics estimates.

Channel	BHLS	BHLS ₂ (BS) (excl. τ)	BHLS ₂ (RS) (incl. τ)	BHLS ₂ (RS) (excl. τ)	Data Direct Integration
$\pi^+\pi^-$	493.73 ± 0.70	494.04 ± 0.76	494.08 ± 0.90	494.10 ± 1.0	497.82 ± 2.80
$\pi^0\gamma$	4.42 ± 0.03	4.46 ± 0.03	4.45 ± 0.03	4.45 ± 0.03	3.47 ± 0.11
$\eta\gamma$	0.63 ± 0.01	0.63 ± 0.01	0.64 ± 0.01	0.64 ± 0.01	0.55 ± 0.02
$\pi^+\pi^-\pi^0$	42.56 ± 0.54	42.97 ± 0.53	43.02 ± 0.54	43.08 ± 0.48	41.38 ± 1.28
K^+K^-	18.10 ± 0.14	18.04 ± 0.14	18.01 ± 0.14	17.99 ± 0.14	17.37 ± 0.55
$K_L K_S$	11.53 ± 0.08	11.70 ± 0.08	11.71 ± 0.08	11.72 ± 0.09	11.98 ± 0.36
HLS Sum	570.97 ± 0.92	571.84 ± 1.06	571.90 ± 1.10	571.98 ± 1.20	572.57 ± 3.15
χ^2/N_{pts}	949/1056	1054/1152	1133/1237	1052/1152	×
Probability	96.7%	93.9 %	93.3 %	93.6 %	×

Table 7: HLS contributions to $10^{10} \times a^{\text{HVP-LO}}$ integrated up to 1.05 GeV, including FSR. The first data column displays the results using the former BHLS [25, 27] and, the second one, those derived from the Basic Solution for BHLS₂, the τ decay data being discarded. The next two data columns refer to the results obtained using the Reference Solution for BHLS₂ using the largest set of data samples, keeping or discarding the τ data. The last data column refers to the numerical integration for each channel of the same set of data which are used in the BHLS/BHLS₂ fits.

The runs leaving aside the 3-pion data briefly reported in Equations (105), show that the dominant $\pi\pi$ contribution can be as low as $(493.80 \pm 0.89) \times 10^{-10}$, *i.e.* 0.30 units of 10^{-10} smaller than the corresponding reference entry in Table 7. Nevertheless, the middle entry line in Equations (105) is very close to Equations (107), where the 3-pion data have been included and exhibits negligible differences with respect to our reference in Table 7. Finally, the fit

corresponding to the last data column in Table 6 has also been analyzed and returns a value for $a_\mu(\pi^+\pi^-, \sqrt{s} \leq 1.05 \text{ GeV}) = (494.32 \pm 0.90) \times 10^{-10}$. This may indicate another additional systematic able to shift the central value by, at most, 0.22×10^{-10} affecting our estimate for $a_\mu^{\text{HVP-LO}}(\sqrt{s} \leq 1.05 \text{ GeV})$ given in Equation (109).

The possible sources of additional systematics just emphasized can be considered as a model uncertainty bounded by $(+0.22, -0.36) \times 10^{-10}$. On the other hand, running the fitting code using the available parametrizations for $\alpha_{em}(s)$, returns differences for the estimates for $a_\mu(\text{HLS})$ of $\simeq 0.4 \times 10^{-10}$, mostly located in the ϕ mass region.

Finally, the question of using the CMD-3 data can be raised. We have run our code using the CMD-3 data [77, 79] for both $K\bar{K}$ decay channels, discarding the kaon data from BaBar, CMD-2 and SND and using only the diagonal part of their error covariance matrices (see Section 16 above). In total, the change for $a_\mu(\sqrt{s} \leq 1.05 \text{ GeV})$ is noticeable $(572.52 \pm 1.12) \times 10^{-10}$, 0.54×10^{-10} larger than our reference in Equation (109), essentially coming from the K^+K^- and $K^0\bar{K}^0$ channels. On the other hand, combining CMD-3, BaBar, (corrected) CMD-2 [75] and SND, leads to $a_\mu(\sqrt{s} \leq 1.05 \text{ GeV}) = (572.52 \pm 1.04) \times 10^{-10}$. This leads us to complete our estimate Equation (109) :

$$10^{10} \times a_\mu(\text{BHLS}_2, \sqrt{s} \leq 1.05 \text{ GeV}) = 571.98 \pm 1.20_{\text{fit}} + \left[\begin{smallmatrix} +1.16 \\ -0.75 \end{smallmatrix} \right]_{\text{syst}} , \quad (110)$$

where the additional systematics come from model variations, α_{em} parametrizations, and data sample consistency issues. The model uncertainties include the marginal effect attributable to the τ data, as this could reflect some (marginal) isospin breaking shortcoming. We have chosen conservatively as reference the RS variant fit excluding the τ data. One should also note that the tension between dikaon data samples introduces non-negligible systematics which contribute a bias. This may have to be revisited when new data will arise.

Taking into account the data upgrade, the corresponding quantity for BHLS is :

$$10^{10} \times a_\mu(\text{BHLS}, \sqrt{s} \leq 1.05 \text{ GeV}) = 570.97 \pm 0.92_{\text{fit}} + \left[\begin{smallmatrix} +1.16 \\ -0.75 \end{smallmatrix} \right]_{\text{syst}} + \left[\begin{smallmatrix} +0.0 \\ -0.9 \end{smallmatrix} \right]_{\tau} , \quad (111)$$

using the present findings to go beyond the former systematics evaluation reminded in Equation (108). The various additional uncertainties just estimated represent conservative upper bounds.

21.3 Dispersive vs LQCD Methods : Additional Systematics

Experimental $e^+e^- \rightarrow \text{hadrons}$ data are dressed by photon radiative corrections and disentangling strong interaction from the electromagnetic effects is a non-trivial task. What is ideally needed as input to the dispersion integrals is the one-particle irreducible (1PI) hadronic part. It is given in QCD by the correlator between two hadronic currents, and this is what is primarily calculated as the LO part of order $O(\alpha^2)$ in lattice QCD. We remind that the bare cross-section undressed from photon radiation effects is not an observable by itself. It requires some theory input, primarily the photon radiative corrections, for its extraction from the physical dressed data. Mandatorily, one has to drop out the photon vacuum polarization effects to get the undressed bare cross-section. By convention, one also includes final state radiation (FSR) in the dipion channel by adopting scalar QED (sQED) for its calculation. Similarly, the radiative decay channels $\pi^0\gamma$ and $\eta\gamma$ are included in our evaluation. Like FSR, they are related to light-by-light scattering insertions.

However, there are other important QED effects like the $\rho^0 - \gamma$ interference which is substantial in the dipion channel because this QED effect is magnified by the resonance enhancement in the ρ region. In the standard dispersive approach, $\rho^0 - \gamma$ mixing effects – inherent in the e^+e^- data – are treated as part of the LO-HVP contribution and are included as well in the calculations of the higher-order contributions. An updated e^+e^- data-based evaluation of the LO and the NLO parts yields the results shown in Table 8⁵⁷.

		$a_\mu \times 10^{-10}$	stat	syst	tot
LO		690.93	0.71	3.83	[3.90]
NLO	diagram a	-20.71	0.03	0.13	[0.13]
NLO	b	10.39	0.01	0.06	[0.06]
NLO	c	0.34	0.00	0.01	[0.01]
NLO	sum	-9.98	0.03	0.07	[0.08]
LO+NLO		680.95	-	-	[3.82]

Table 8: LO- and NLO-HVP results in the standard dispersive approach based on e^+e^- data. The NLO diagrams are shown in Fig. 12.

Here we have to remind that, in contrast to the usual dispersive estimations, LQCD calculations are based on the hadronic current correlator such that $\rho^0 - \gamma$ mixing is not included in the leading order LQCD results (unless it is added by hand from phenomenological analyses, if not calculated separately).

So the question of how to disentangle the QCD effects from QED ones, has to be reconsidered under this aspect. One possibility is to apply effective field theory methods like the resonance Lagrangian approach, the other is lattice QCD, the only method which can answer the question from first principles. In fact, to disentangle better QCD from QED effects in the e^+e^- data-based dispersive approach, one has to subtract the $\rho^0 - \gamma$ interference from the $e^+e^- \rightarrow \pi^+\pi^-$ data⁵⁸, expecting to get the effect back as a part of the higher-order contributions.

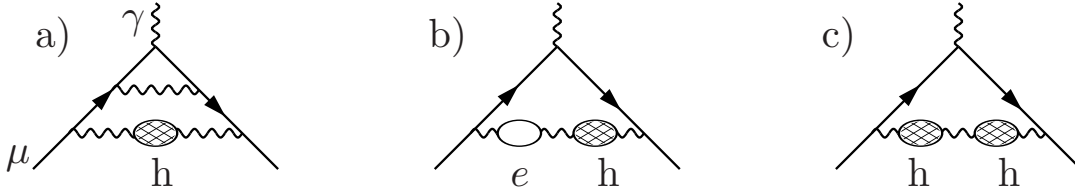


Figure 12: Higher order contributions to the hadronic VP; the shaded blob depicts the LO hadronic VP, the empty blob the LO leptonic VP.

Here is the place to remind that the $\rho^0 - \gamma$ mixing is responsible for the discrepancy between the isospin rotated isospin breaking corrected τ spectral-function and the e^+e^- spectral-function [126, 127, 40]; this has been shown in a straightforward “VMD-II+sQED” simple

⁵⁷For the present exercise, the BaBar dipion data have been taken into account

⁵⁸The similar $\omega - \gamma$ and $\phi - \gamma$ effects are much smaller and can be neglected.

effective resonance Lagrangian model [43] as well as in the BHLS approach [29, 25] as utilized in the present analysis. By convention, to bring τ data closer to e^+e^- -data, it looked natural to correct the τ -data to conform with the commonly adopted dispersive approach based on the e^+e^- data.

In fact, the measured τ -decay dipion spectra are devoid of photon interference effects. According to what we just have been arguing, one should actually not apply this mixing correction to the τ -decay data, as it has been done within our BHLS global fit framework or in the much simpler model applied in [43]. One should better subtract the $\rho^0 - \gamma$ mixing from the e^+e^- data, to get an object closer to a pure hadronic “blob” and then proceed as usual. As a possible subtlety, this requires to work in the “VMD-I” basis where the $\rho^0 - \gamma$ system is parametrized in terms of fields where a direct lepton- ρ coupling is absent. This is the basis of the BHLS Lagrangian formulation. Being proportional to the hadronic production cross-section, the hadronic 1PI amplitude and the corresponding $R(s)$ (see Eq. (1)) do not depend on rotations in the (γ, ρ^0) field space.

The field rotation invariance has been directly confirmed by comparing, on the one hand, the “VMD-II + sQED” modeling adopted in [43], which uses the mass eigenstate basis where a direct ρ -lepton coupling is induced by the necessary field rotation [128] and, on the other hand, our BHLS modeling where a direct ρ -lepton coupling is absent. One thus can apply the standard diagrammatic expansion of Fig. 12 with the modified effective $R(s)$ -function and obtains the results presented in Table 9 :

		$a_\mu \times 10^{-10}$	stat	syst	tot	shift
LO		694.11	0.71	3.86	[3.93]	+3.18
NLO	diagram a	-20.85	0.03	0.13	[0.13]	-0.14
NLO	b	10.45	0.01	0.06	[0.06]	+0.05
NLO	c	0.34	0.00	0.01	[0.01]	+0.00
NLO	sum	-10.06	0.03	0.07	[0.08]	-0.09
LO+NLO		684.05	-	-	[3.85]	3.10

Table 9: LO- and NLO-HVP results in the dispersive approach based on e^+e^- data, after having removed the $\rho^0 - \gamma$ mixing from the hadronic blob.

which corresponds to what, in principle, lattice QCD is doing.

The LQCD results displayed in Fig. 13 are full HVP results, which include ud light quark, strange and charm contributions including the connected and disconnected parts as well as isospin breaking contributions either calculated on the lattice or adopted from phenomenological estimates in terms of data. They do not include $\gamma - \rho$ mixing to our knowledge, however. In lattice QCD this effect is counted as a NLO effect, which has to be evaluated separately⁵⁹.

According to our Tables, the commonly adopted dispersive set up gets a shift⁶⁰ of $\delta a_\mu[\pi\pi]_{\rho\gamma} \simeq +(3.10 \pm 0.03) \times 10^{-10}$ at NLO, *i.e.* a 1 σ increase. See also the results presented in Table 3 of [129] where a $\rho^0 - \gamma$ mixing shift of 2.74×10^{-10} on the I=1 component at LO has been reported as a difference between LQCD data and the phenomenological dispersive approach. The

⁵⁹ Contributions from FSR and radiative decays should have been added in a consistent comparison with data-based dispersive results.

⁶⁰The systematic uncertainties in Tables 8 and 9 are 100% correlated, except for the sub-dominant diagram c.

upgraded result for $\delta a_\mu[\pi\pi]_{\rho\gamma}$ is based on an actualized data compilation, with mixing correction applied to the full vector form-factor and including NLO corrections.

More or less surprisingly, the sum of LO+NLO differs in the two settings, *i.e.* the mixing effect subtracted from the LO result does not show up as a higher-order effect of comparable magnitude. It is actually not surprising because the $\rho^0 - \gamma$ mixing effect, if included in the LO dispersion integral, is larger than if taken into account in higher-order diagrams where the effect is weighted by the higher-order kernel functions. Our result based on correcting the e^+e^- dipion channel in the range up to 1 GeV, where sQED estimates can be trusted, indirectly compares with the deviation $(9.1 \pm 5.0) \times 10^{-10} (1.8\sigma)$ between the τ -based hadronic contribution to a_μ and the e^+e^- -based one reported in [130]. Our result does not include τ data while the τ based result of [130] includes τ data up to 1.8 GeV which are combined with e^+e^- data which still include $\rho^0 - \gamma$ mixing. That the results are increasing in both cases is as expected, but there is no reason why the numerical results should agree.

Our suggestion to base the standard bookkeeping such as Figure 12 on a purer QCD $\gamma - \rho$ undressed hadronic blob is motivated by the fact that lattice QCD does not include any QED effects if not taken into account as an extra contribution and also by the fact that τ -data are free of similar mixing effects, and it looks somewhat artificial to add effects to τ -decay spectral data that are absent in the corresponding measurements. Nevertheless, as already said, surprisingly we subtract a non-negligible contribution, which we do not get back in higher orders. It is important to note that the shift $\delta a_\mu[\pi\pi]_{\rho\gamma}$ is real as it derives from the manifest discrepancy observed between τ and e^+e^- spectral-function data in the corresponding time-like $\pi\pi$ production processes. As mentioned before, the $\gamma - \rho$ interference is substantial because of the manifest resonance enhancement in the time-like regime. Lattice QCD is taking advantage of the fact that, for the calculation of a_μ^{had} , only the space-like VP-function is needed. However, there is no ρ -resonance peak in the Euclidean region which could enhance a photon-exchange interference effect; the ρ -resonance is completely smeared out and a resonance-enhancement cannot be localized there in any obvious way. Because of a model-independent clean separation of QCD is only possible in lattice QCD, one has to wait for the relevant LQCD results to get a better understanding of QED-QCD interference effects.

One may conclude that *all* standard dispersive evaluations should either be upgraded by adding $+(3.10 \pm 0.31) \times 10^{-10}$ to the LO+NLO results⁶¹, or accounted for in the systematic errors by adding there the amount of this shift. For the time being, we have adopted this second solution.

21.4 BHLS₂ Evaluation of $a_\mu^{\text{HVP-LO}}$

With the BHLS₂ and BHLS evaluations of $a_\mu^{\text{HVP-LO}}(\text{HLS}, \sqrt{s} \leq 1.05 \text{ GeV})$ displayed in Equations (110) and (111) and the information given in the left part of Table 10, one can derive

⁶¹Concerning the model dependence of the prediction for the $\rho^0 - \gamma$ interference, we remind that this effect depends on only one extra parameter, the well known leptonic width of the ρ^0 or, equivalently, on the coupling $g_{\rho ee}$, also well known experimentally. Since the effect is small, a few units in 10^{-10} , we can generously assign a very conservative 10% model uncertainty, without substantially increasing the overall uncertainties coming with the $e^+e^- \rightarrow \pi^+\pi^-$ data.

the corresponding values for the full $a_\mu^{\text{HVP-LO}}$. One thus gets :

$$\begin{cases} 10^{10} \times a_\mu(\text{BHLS}_2) = 686.65 \pm 3.01_{\text{fit}} + \left[\begin{smallmatrix} +1.16 \\ -0.75 \end{smallmatrix} \right]_{\text{syst}} + \left[\begin{smallmatrix} +3.10 \\ -0.0 \end{smallmatrix} \right]_{\rho\gamma} , \\ 10^{10} \times a_\mu(\text{BHLS}) = 685.64 \pm 2.91_{\text{fit}} + \left[\begin{smallmatrix} +1.16 \\ -1.65 \end{smallmatrix} \right]_{\text{syst}} + \left[\begin{smallmatrix} +3.10 \\ -0.0 \end{smallmatrix} \right]_{\rho\gamma} . \end{cases} \quad (112)$$

In the case of BHLS, due to the inclusion of τ channel within the global fit procedure, the corresponding systematics have been added linearly to the others. Indeed, as stated several times for BHLS and BHLS₂, the observed systematics rather come as biases and so, should be treated separately from the fit error which fully absorbs the reported statistical and systematics from the various experiments encompassed inside each of our HLS frameworks.

The additional systematics absorb uncertainties which can be attributed to the model workings *and* to the (marginal) tension observed between some of the selected experimental data samples. For clarity, the error coming from the $\rho^0 - \gamma$ interference effect discussed just above is given separately.

Our evaluations for $a_\mu^{\text{HVP-LO}}$, given by Equations (112), are shown in Figure 13 together with some other recent results derived in different phenomenological contexts [4, 130, 71] or via LQCD data samples with $N_f = 2 + 1 + 1$. As for their specific HLS modeling parts, the corresponding fit probabilities shown by the down-most entries in Table 7 are always fairly good.

As for modeling effects, the central values for BHLS and BHLS₂ – running on the same set of data samples – are shifted apart by $\simeq 1.5 \times 10^{-10}$; however, if one takes into account the magnitude of the additional systematics, Figure 13 clearly indicates that this shift is not significant and so no noticeable modeling effect shows up. Moreover, Figure 13 clearly shows that both HLS based estimates for $a_\mu^{\text{HVP-LO}}$ are consistent with the evaluation derived by numerical integration of the data⁶².

Actually, the estimates for the muon HVP-LO derived by the various dispersive methods (the five data points displayed in the bottom part of Figure 13) are quite comparable with each other as they use as input to evaluate $a_\mu^{\text{HVP-LO}}$ the e^+e^- annihilation cross sections as derived from the data or as reconstructed from fit. Therefore, the results thus provided do not split out the electromagnetic corrections; in particular the $\gamma - \rho^0$ mixing effects is merged in the plotted systematics only for the BHLS/BHLS₂ entries, not for the other dispersive results plotted.

21.5 BHLS₂ Evaluation of Muon Anomalous Magnetic Moment

Having at hand our estimate Equation (110), one can derive the BHLS₂ evaluation for $a_\mu = (g - 2)/2$, the muon anomalous magnetic moment. The left part of Table 10 collects the pieces to add up with $a_\mu(\text{BHLS}_2)$ to get the full leading order HVP, its value is shown as the top entry in the right-hand part of Table 10 where the other contributions are included. The value for $\Delta a_\mu = a_\mu(\text{exp}) - a_\mu(\text{th})$ and its statistical significance are the bottom entries there. Taking into account all additional systematics, one thus gets :

$$10^{10} \times a_\mu = 11\,659\,175.96 \pm 4.17_{\text{th}} + \left[\begin{smallmatrix} +1.16 \\ -0.75 \end{smallmatrix} \right]_{\text{syst}} + \left[\begin{smallmatrix} +3.10 \\ -0.0 \end{smallmatrix} \right]_{\rho\gamma} \quad (113)$$

⁶²See the top point in Figure 13, derived by excluding the BaBar dipion sample for a consistent comparison with the BHLS entries.

Contribution from	Energy Range	$10^{10} \times a_\mu^{\text{HVP-LO}}$	Contribution from	$10^{10} \times a_\mu$
missing channels	$\sqrt{s} \leq 1.05$	1.28 ± 0.17	LO-HVP	$686.65 \pm 3.01 + \left[\begin{smallmatrix} +1.16 \\ -0.75 \end{smallmatrix} \right]_{\text{syst}} + \left[\begin{smallmatrix} +3.10 \\ -0.0 \end{smallmatrix} \right]_{\rho\gamma}$
J/ψ		8.94 ± 0.59	NLO HVP[43]	-9.927 ± 0.072
Υ		0.11 ± 0.01	NNLO HVP [131]	1.24 ± 0.01
hadronic	(1.05, 2.00)	62.21 ± 2.53	LBL [132]	10.34 ± 2.88
hadronic	(2.00, 3.20)	21.63 ± 0.93	NLO-LBL [133]	0.3 ± 0.2
hadronic	(3.20, 3.60)	3.81 ± 0.07	QED [134, 135]	$11\,658\,471.8851 \pm 0.0036$
hadronic	(3.60, 5.20)	7.59 ± 0.07	EW [136]	15.36 ± 0.11
pQCD	(5.20, 9.46)	6.27 ± 0.01	Total Theor.	$11\,659\,175.96 \pm 4.17 + \left[\begin{smallmatrix} +1.16 \\ -0.75 \end{smallmatrix} \right]_{\text{syst}} + \left[\begin{smallmatrix} +3.10 \\ -0.0 \end{smallmatrix} \right]_{\rho\gamma}$
hadronic	(9.46, 11.50)	0.87 ± 0.05	Exper. Aver.	$11\,659\,209.1 \pm 6.3$
pQCD	(11.50, ∞)	1.96 ± 0.00	$10^{10} \times \Delta a_\mu$	$33.14 \pm 7.56 - \left[\begin{smallmatrix} +1.16 \\ -0.75 \end{smallmatrix} \right]_{\text{syst}} - \left[\begin{smallmatrix} +3.10 \\ -0.0 \end{smallmatrix} \right]_{\rho\gamma}$
Total	$1.05 \rightarrow \infty$ + missing chann.	114.67 ± 2.76	Significance ($n\sigma$)	4.38σ

Table 10: The left-side Table displays the contributions to $a_\mu^{\text{HVP-LO}}$ from the various energy regions, including the contribution of the non-HLS channels from the $\sqrt{s} < 1.05$ GeV region; only total errors are shown. The right-side Table provides the various contributions to a_μ and information for $\Delta a_\mu = a_\mu(\text{exp}) - a_\mu(\text{th})$ for the case of the RS variant of BHLS₂. The statistical significance of Δa_μ is given at central value (see text).

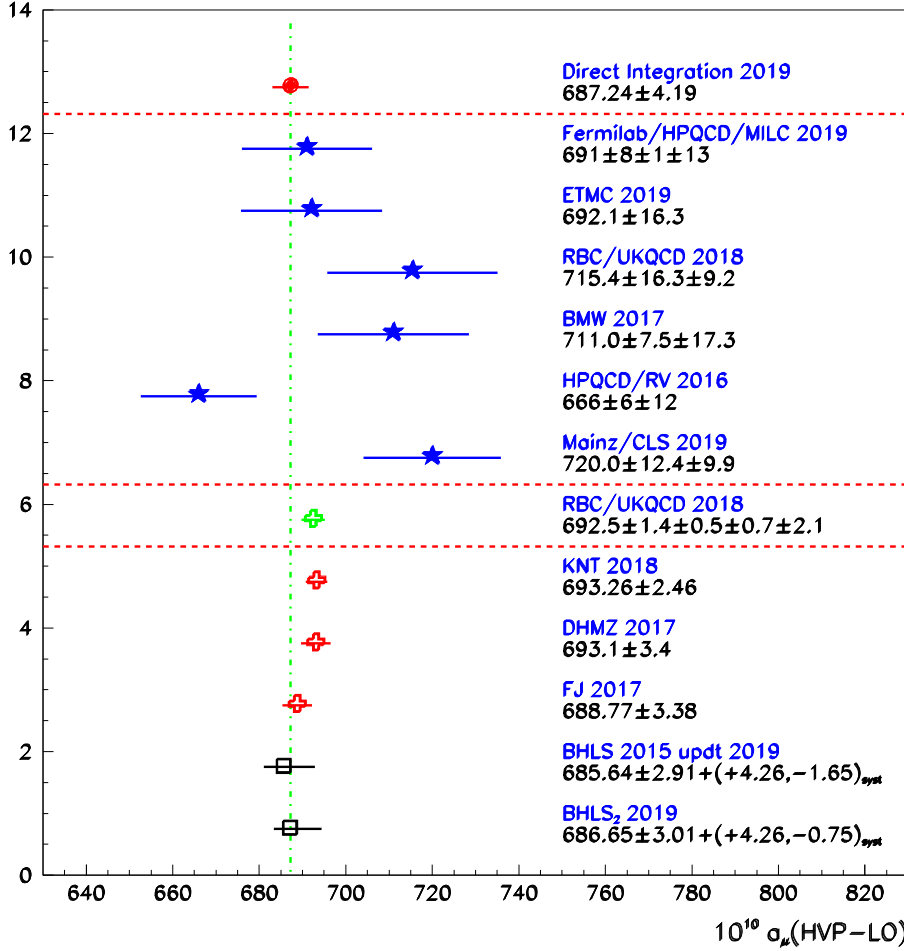


Figure 13: Recent evaluations of $10^{10} \times a_{\mu}^{\text{HVP-LO}}$: On top, the result derived by direct integration of the data combined with perturbative QCD; the next six points display some recent evaluations derived by LQCD methods and reported in resp. [137], [138], [139], [140], [11] and [141] with $N_f = 2 + 1 + 1$. The second point from [139] displayed has been derived by supplementing lattice data with some phenomenological information. These are followed by the evaluations from [71],[130] and [4]. The value derived using BHLS [27] – updated with the presently available data – and the evaluation from BHLS₂ are given with their full systematic uncertainties, including the $\rho^0 - \gamma$ mixing effect (see text).

and, taking into account the shifts produced by all systematics, one gets :

$$28.88 \pm 4.17 \leq 10^{10} \times \Delta a_\mu (= a_\mu^{exp.} - a_\mu^{theor.}) \leq 33.89 \pm 4.17 , \quad (114)$$

which means that the statistical significance of Δa_μ is predicted greater than 3.82σ . The shift just reported is partly due to the estimates of the various modeling effects involved, partly due to somewhat conflicting aspects of some data samples and partly due to the identified $\gamma - \rho^0$ mixing effects which add up linearly.

Our estimate for a_μ given in Equation (113) relies on a variant of the traditional estimate [132] for the Light-by-Light (LBL) contribution $((10.34 \pm 2.88) \times 10^{-10})$. Danilkin, Redmer and Vanderhaegen (DRV) have quite recently published a comprehensive analysis of all ingredients participating to the LBL term and proposed for it the much more precise value [142] $(8.7 \pm 1.3) \times 10^{-10}$ which leads to :

$$10^{10} \times a_\mu^{DRV} = 11\,659\,174.78 \pm 3.28_{\text{th}} + \left[\begin{smallmatrix} +1.16 \\ -0.75 \end{smallmatrix} \right]_{\text{syst}} + \left[\begin{smallmatrix} +3.10 \\ -0.0 \end{smallmatrix} \right]_{\rho\gamma}$$

and to $\Delta a_\mu^{DRV} = (34.32 \pm 7.10) \times 10^{-10}$. This makes the significance for Δa_μ jumping from $(3.8 \div 4.5) \sigma$ to $(4.2 \div 4.7) \sigma$.

22 Summary and Conclusions

The present paper has addressed several topics covering modeling, phenomenology and the evaluation of the muon anomalous magnetic moment which puts forward, as well known, a hint for a physics effect beyond the Standard Model expectations. For the sake of clarity, each of these topics is considered separately.

From BHLS to BHLS₂

The BHLS framework [25], although quite successful [26, 27, 143], has been shown to exhibit a non-optimum behavior in limited and well identified kinematical regions : The threshold region and some aspects of the ϕ mass region; the former issue renders delicate the continuation of form factors across the chiral point, the latter has led to discard the ϕ mass region for 3-pion final state – the so-called Model B [25].

In order to cure these diseases, one has initiated a new breaking procedure of the general HLS framework [18]. For this purpose, besides the BKY mechanism [28, 34, 35], one has introduced a breaking mechanism taking place at the level of the covariant derivative (CD) itself, *i.e.* inside the basic ingredient of the HLS Model. This (seemingly novel) CD breaking mechanism allows naturally the ρ^0 , ω and ρ^\pm fields to carry different Higgs-Kibble masses. This takes its importance when going to loop corrections to the vector meson mass matrix [29, 25] which generate a dynamical mixing of the vector mesons calling for an s -dependent redefinition of the vector meson fields to recover mass eigenstates.

Thanks to its nonet symmetry breaking piece, the CD breaking scheme generates a non-zero $m_{\rho^0} - m_\omega$ difference which naturally makes the three s -dependent mixing angles to vanish at the chiral point. In this way, the timelike to spacelike analytic continuations become smooth without any *ad hoc* trick.

Relying on BKY and the CD breaking, the Basic Solution (BS) is defined and represents the first variant of BHLS₂. Another mechanism can also be invoked which turns out to state that the neutral vector fields involved in physical processes are not their ideal combinations but mixtures of these, constructed via a rotation. This Primordial Mixing (PM) mechanism⁶³ of vector mesons assumes a $1 + \mathcal{O}(\epsilon)$ rotation. Working at first order in breaking parameters, the merging of the BKY and CD breakings together with the PM mechanism define our Reference Solution (RS), the second variant of BHLS₂ covering the full HLS scope more easily than the BS variant (as it stands presently).

In both variants of BHLS₂, the \mathcal{L}_V piece of the non-anomalous Lagrangian is modified while its \mathcal{L}_A piece remains unchanged⁶⁴ compared to the former BHLS [25].

The e^+e^- Annihilation Phenomenology

The BKY and CD breaking schemes, together with the Primordial Mixing, allow to construct the non-anomalous and anomalous pieces of BHLS₂, a new (broken) HLS Lagrangian. This allows for a simultaneous study of the e^+e^- annihilation into 6 final states ($\pi^+\pi^-$, $\pi^0\gamma$, $\eta\gamma$, $\pi^+\pi^-\pi^0$, K^+K^- , K_LK_S) within a unified framework where global fits can be worked out.

The fits have been performed by taking into account the fact that most of the data samples carry normalization uncertainties, frequently dominant; these are appropriately considered in order to avoid biased results for physics quantities. The iterative method developed in [27] is thus intensively used in the global fits reported here; the convergence criterion chosen to stop the iteration at order $n + 1$ was $\delta\chi^2 = |\chi_{\text{tot}}^2(n + 1) - \chi_{\text{tot}}^2(n)| < (0.3 \div 0.5)$. As $\chi_{\text{tot}}^2 \simeq 1000 \div 1200$ for $\simeq 1150 \div 1240$ data points, this convergence criterion is clearly constraining.

The fitting procedure has allowed to detect (and discard) a very few data samples which hardly accommodate the global framework fed with almost all the existing data samples. Beside the already identified [27] two $\pi^+\pi^-$ samples, one also found that, out of the 7 available $\pi^+\pi^-\pi^0$ data samples, one [87] hardly fits the global context, as also reported by others [92]. Figures 2, 3 and 4 together with Table 3 prove the fairly good quality of the global description for the $\pi^+\pi^-$, $(\pi^0/\eta)\gamma$ and $\pi^+\pi^-\pi^0$ channels. As for the 3-pion channel, one should note that BHLS₂ encompasses easily the samples collected in the ϕ mass region and so, solves the difficulty encountered there by the former BHLS.

A thorough study of the available data samples has been performed concerning both the K^+K^- and K_LK_S channels for which some tension is expected, as reported in [77]. The analysis in Section 16 has shown that the SND, BaBar [76] and the updated [75] CMD-2 data are in fairly good agreement with each other and accommodate easily the HLS context where all other kinds of data are encompassed. Tension has indeed been observed between the CMD-3 data [77, 79] and the other samples. This tension has been traced back to the off-diagonal part of the CMD-3 error covariance matrices for both the K^+K^- and K_LK_S spectra; this analysis is summarized by Table 2. In order to include the BaBar (and/or CMD-3 data) within the global framework, energy shifts relative to the CMD-2/SND energy scale (chosen as energy scale reference) are mandatory and have been fitted at values consistent with the

⁶³The Primordial Mixing of neutral vector mesons resembles the mixing scheme for the neutral pseudoscalar mesons developed in [144].

⁶⁴This might have to be revisited in order to improve the working of BS in the τ and $\pi^+\pi^-\pi^0$ sectors of the broken HLS Lagrangian.

reported expectations [76, 77]. To perform this exercise, when using the CMD-3 data, the error covariance matrices of these (only) have been amputated from their off-diagonal part.

One can finally remark that, once the energy scales of the CMD-3 and BaBar [76] data relative to CMD-2/SND are applied, one does not observe a visible tension among them any longer as illustrated by Figure 5, where all data samples are nicely superimposing onto the same fit function.

Meson Form Factors in the Spacelike Region

The BHLS₂ form factors supplied with the parameter values derived from global fits to the *timelike region data only* have been shown to nicely predict the behavior of the π^\pm and K^\pm form factors *in the close spacelike region*, as they can be expected from NA7 and Fermilab data. Moreover, including these (model-independent) spacelike data within the BHLS₂ fit procedure does not exhibit any gain in the description of the spacelike region as obvious from Table 4 and from Figure 6.

Our derived π^\pm and K^\pm form factors, which perform fairly well simultaneously in the spacelike and timelike regions, strongly supports the validity of the BHLS₂ predictions in the s -region located in between. If the fairly good continuation of $F_{\pi^\pm}(s)$ is actually performed over a limited gap in s to reach the spacelike region, one may wonder about the so successful continuation of $F_{K^\pm}(s)$ over an s -gap greater than 1 GeV². This indicates that our modified Breit-Wigner formulas are performing (unexpectedly) well far beyond the ϕ energy region where their parameters are determined.

The LQCD Collaborations HPQCD and ETM have provided $F_{\pi^\pm}(s)$, the former as a parametrization, the latter by corresponding spectra, covering the same space-like s -region as the NA7 experiment. Figure 8 shows the superposition of the BHLS₂ prediction (without any free parameter) together with the parametrization provided by HPQCD and the two ETM spectra; the accord is very good for HPQCD and simply perfect for both the ETM spectra. There is, unfortunately, no reported LQCD data for the kaon form factors to which one could compare.

The success just emphasized for the BHLS₂ π^\pm and K^\pm form factors compared to spacelike experimental or LQCD data gives confidence in other physics information involving the chiral point region. Let us limit oneself, in this Subsection, to briefly comment on the neutral kaon electromagnetic form factor. As reminded in the main text, the slope for the $F_{K^0}(s < 0)$ form factor at $s \rightarrow 0$ is reported negative. This is qualitatively consistent with the BHLS₂ finding for $F_{K^0}(s)$ shown in Figure 9, as it is found to carry a negative slope at negative s and a positive slope at positive s . However, the effects of the neglected $\mathcal{O}(\epsilon^2)$ corrections actually prevent to provide confidently accurate slope predictions in the neighborhood of $s = 0$ which is a delicate region for our $\mathcal{O}(\epsilon)$ approximations.

The pion form factor measured by the NA7 and Fermilab Collaborations are model independent and, actually, it cannot be measured in a model-independent way above $|s| \simeq 0.25$ GeV². To go beyond, one should accept to consider data where the extraction of $F_{\pi^\pm}(s)$ is model-dependent. Figure 6 already indicates that the two *unfitted* DESY measurements fall (almost) exactly onto the fitting curve together with the model-independent NA7 and Fermilab measurements. The JLAB data points are more or less closer to the BHLS₂ expectation depending on the method used to extract $F_{\pi^\pm}(s)$. Nevertheless, our analysis indicates that the BHLS₂ prediction could well be valid down to $\simeq -1$ GeV², possibly slightly beyond.

In summary, our analysis clearly indicates that, *inherently*, BHLS₂ only supplied with consistent e^+e^- annihilation data, leads precisely to the spacelike expectations supported by the precise NA7 data or the available LQCD input as well. Nevertheless, LQCD information on $F_{K^\pm}(s)$ (and $F_{K^0}(s)$) would be welcome to better check the open strangeness sector.

Physical Quantities and Model Dependence Effects

BHLS₂ has derived evaluations of several physics quantities (see Sections 18, 19 and 20) and some deserve special emphasis. As shown in Table 5, one reaches precise values for the charged pion and kaon charge radii (fm²) :

$$\langle r_{\pi^\pm}^2 \rangle = 0.430 \pm 0.002_{\text{mod}} \pm 0.001_{\text{fit}} \quad , \quad \langle r_{K^\pm}^2 \rangle = 0.268 \pm 0.004_{\text{mod}} \pm 0.001_{\text{fit}} \quad ,$$

our estimate for $\langle r_{\pi^\pm}^2 \rangle$ is in fairly good agreement with the most recent evaluations [114, 115]. Our evaluation for $\langle r_{K^\pm}^2 \rangle$ is in accord with the reported values shown in Table 5 and is more precise. The Reference Solution of BHLS₂ also leads to :

$$\frac{f_{K^\pm}}{f_{\pi^\pm}} = 1.247 \pm 0.020_{\text{syst}} \pm 0.003_{\text{fit}} \quad ,$$

where the quoted systematic error reflects different variants of the modeling.

Table 6 collects the values of the BHLS₂ model parameters obtained under several fit conditions and discussed in Section 20. An interesting numerical correlation is observed between the fundamental HLS parameter a and the BKY breaking parameter z_V within the BHLS₂ framework. This can be approximated by $az_V \simeq 2.6$; good fit qualities are thus observed with a varying over a large interval, namely from 1.6 to 2.6. The rightmost two data columns in Table 6, which collect the fit values of a large sample of breaking parameters in two extreme cases ($a \simeq 1.6$ and $a \simeq 2.6$), also show correlatedly important changes in some of the other breaking parameter values. Table 6 also shows that the fit qualities reached in all cases are almost identical.

One can herefrom conclude that the various model parameter sets efficiently conspire to provide almost identical cross-sections and form factors which are, actually, the real observables feeding BHLS₂. This has been substantiated by comparing the running of BHLS₂ fed with our consistent set of data samples under the various conditions underlying the fits reported in Table 6.

A motivated piece of information to detect parametrization effects are the integrals $a_\mu(\sqrt{s} \leq 1.05 \text{ GeV})$ given in Table 7. Running the BS variant (excluding the τ data) provides $a_\mu(BS, \sqrt{s} \leq 1.05 \text{ GeV}) = (571.84 \pm 1.06) \times 10^{-10}$, while running the RS variant running on the same data (with the Primordial Mixing angles free) returns $a_\mu(RS, \sqrt{s} \leq 1.05 \text{ GeV}) = (571.98 \pm 1.20) \times 10^{-10}$. So the difference between the various parametrizations happens indeed to be marginal and quite comparable in magnitude to the uncertainties generated by using somewhat conflicting data samples. Nevertheless, external information constraining or relating some of the model parameters could be useful in order to reduce the parameter freedom in fits and so the parameter correlations.

As for the important muon HVP topic : Complementing the BHLS₂ contribution by the whole hadronic contribution not covered by the (BHLS₂) model and reported in the left-hand side part of Table 10, one gets :

$$10^{10} \times a_{\mu}^{\text{HVP-LO}} = 686.65 \pm 3.01 + \left[\begin{smallmatrix} +1.16 \\ -0.75 \end{smallmatrix} \right]_{\text{syst}} + \left[\begin{smallmatrix} +3.10 \\ -0.0 \end{smallmatrix} \right]_{\rho\gamma} .$$

Its (statistical + model) uncertainty (3.01) is sharply dominated by those of the whole non-HLS contribution : 2.76×10^{-10} – reported in Table 10 – versus the BHLS₂ uncertainty $(1.06 \div 1.20) \times 10^{-10}$ (see Table 7).

So, a significant improvement of the uncertainty for $a_{\mu}^{\text{HVP-LO}}$ can only follow from an improved accuracy of the hadronic contributions of higher energies, especially those from the (1.05 – 2.00) GeV region. Therefore, presently, as global fit methods like BHLS₂ constrain the central value for $a_{\mu}^{\text{HVP-LO}}(\text{HLS})$, they do alike for $a_{\mu}^{\text{HVP-LO}}(\text{HLS+non-HLS})$. The effect of the $\rho^0 - \gamma$ mixing vs LQCD is shown separately for clarity.

Our estimate for the full muon anomalous moment is :

$$10^{10} \times a_{\mu} = 11\,659\,175.96 \pm 4.17_{\text{th}} + \left[\begin{smallmatrix} +1.16 \\ -0.75 \end{smallmatrix} \right]_{\text{syst}} + \left[\begin{smallmatrix} +3.10 \\ -0.0 \end{smallmatrix} \right]_{\rho\gamma} ,$$

which is, at least, at 3.8σ from the BNL measurement. The systematics are actually upper bounds to a possible bias affecting a_{μ} .

Appendices

A The Full HLS Non-Anomalous Lagrangian in the New Scheme

For clarity, the full non-anomalous HLS Lagrangian is written :

$$\mathcal{L}_{\text{HLS}} = \mathcal{L}_A + a\mathcal{L}_V + \mathcal{L}_\tau + \mathcal{L}_{p^4} \quad (115)$$

and the various pieces will be given just below.

A.1 The $\mathcal{L}_A + a\mathcal{L}_V$ Lagrangian Piece

First, one displays the part of $\mathcal{L}_{\text{VMD}} = \mathcal{L}_A + a\mathcal{L}_V$ relevant for the physics we address, especially e^+e^- annihilations. This is :

$$\begin{aligned} \mathcal{L}_{\text{VMD}} = & \partial\pi^+ \cdot \partial\pi^- + \frac{1}{2}\partial\pi^0 \cdot \partial\pi^0 + \partial K^+ \cdot \partial K^- + \partial K^0 \cdot \partial\bar{K}^0 \\ & + ie \left[1 - \frac{a}{2}(1 + \Sigma_V + \frac{\Delta_V}{3}) \right] A \cdot \pi^- \overleftrightarrow{\partial} \pi^+ \\ & + ie \frac{a}{6z_A} (1 + \frac{\Delta_A}{2})(z_V - 1 - \Sigma_V + \Delta_V) A \cdot K^0 \overleftrightarrow{\partial} \bar{K}^0 \\ & + ie \left[1 - \frac{a}{6z_A} \{2 + z_V + 2\Sigma_V + 2\Delta_V\} (1 - \frac{\Delta_A}{2}) \right] A \cdot K^- \overleftrightarrow{\partial} K^+ \\ & + \frac{1}{2} \left[m_{\rho^0}^2 (\rho_I^0)^2 + m_\omega^2 \omega_I^2 + m_\phi^2 \phi_I^2 \right] - e \left[f_{\rho\gamma}^I \rho_I^0 + f_{\omega\gamma}^I \omega_I + f_{\phi\gamma}^I \phi_I \right] \cdot A \\ & + \frac{ia g}{2} (1 + \Sigma_V) \left\{ [1 + \xi_3] \rho_I^0 + \Delta_V \omega_I \right\} \cdot \pi^- \overleftrightarrow{\partial} \pi^+ \\ & + \frac{ia g}{4z_A} \left[1 - \frac{\Delta_A}{2} \right] [1 + \Sigma_V + \Delta_V + \xi_3] \rho_I^0 \cdot K^- \overleftrightarrow{\partial} K^+ \\ & + \frac{ia g}{4z_A} \left[1 - \frac{\Delta_A}{2} \right] \left[1 + \Sigma_V + \Delta_V + \frac{2}{3}(1 - z_V)\xi_0 + \frac{1}{3}(1 + 2z_V)\xi_8 \right] \omega_I \cdot K^- \overleftrightarrow{\partial} K^+ \\ & + \frac{ia g}{4z_A} \left[1 + \frac{\Delta_A}{2} \right] [1 + \Sigma_V - \Delta_V + \xi_3] \rho_I^0 \cdot K^0 \overleftrightarrow{\partial} \bar{K}^0 \\ & - \frac{ia g}{4z_A} \left[1 + \frac{\Delta_A}{2} \right] \left[1 + \Sigma_V - \Delta_V + \frac{2}{3}(1 - z_V)\xi_0 + \frac{1}{3}(1 + 2z_V)\xi_8 \right] \omega_I \cdot K^0 \overleftrightarrow{\partial} \bar{K}^0 \\ & - \frac{ia g \sqrt{2}}{4z_A} (1 - \frac{\Delta_A}{2}) \left[z_V - \frac{1}{3}(1 - z_V)\xi_0 + \frac{1}{3}(1 + 2z_V)\xi_8 \right] \phi_I \cdot K^- \overleftrightarrow{\partial} K^+ \\ & + \frac{ia g \sqrt{2}}{4z_A} (1 + \frac{\Delta_A}{2}) \left[z_V - \frac{1}{3}(1 - z_V)\xi_0 + \frac{1}{3}(1 + 2z_V)\xi_8 \right] \phi_I \cdot K^0 \overleftrightarrow{\partial} \bar{K}^0. \end{aligned} \quad (116)$$

The pseudoscalar fields occurring there are the renormalized ones defined exactly as in [25]. For simplicity, we use ideal vector fields. The $V - \gamma$ couplings are :

$$\begin{cases} f_{\gamma\rho}^I &= \frac{m^2}{g} \left[1 + \Sigma_V + \frac{\Delta_V}{3} + \xi_3 \right], \\ f_{\gamma\omega}^I &= \frac{m^2}{3g} \left[1 + \Sigma_V + 3\Delta_V + \frac{2}{3}(1 - z_V) \xi_0 + \frac{(1 + 2z_V)}{3} \xi_8 \right], \\ f_{\gamma\phi}^I &= -\frac{\sqrt{2}m^2}{3g} \left[z_V - \frac{\xi_0}{3}(1 - z_V) + \frac{(1 + 2z_V)}{3} \xi_8 \right]. \end{cases} \quad (117)$$

One has discarded the (irrelevant) photon mass term. The vector meson masses are given in Eq. (26). Δ_V and Σ_V have been defined in Section 3.

In practical use, one should perform the change of field given in Eq. (27) and collect the terms corresponding to each (neutral) vector meson coupling.

A.2 The \mathcal{L}_τ Lagrangian Piece

The new \mathcal{L}_τ is given below (after performing an integration by parts to remove the terms with $\partial W^\pm (= 0)$) :

$$\begin{aligned} \mathcal{L}_\tau &= ag^2 f_\pi^2 (1 + \Sigma_V) \rho^+ \cdot \rho^- - \frac{iV_{ud} g_2}{2\sqrt{2}} W^+ \cdot \left[1 - \frac{a}{2z_A} (1 + \Sigma_V) \right] K^0 \overset{\leftrightarrow}{\partial} K^- \\ &\quad - \frac{1}{2} agg_2 f_\pi^2 (1 + \Sigma_V) \left[V_{ud} W^+ \cdot \rho^- + \bar{V}_{ud} W^- \cdot \rho^+ \right] - \frac{ia g}{2\sqrt{2}z_A} (1 + \Sigma_V) \rho^+ \cdot K^0 \overset{\leftrightarrow}{\partial} K^- \\ &\quad + \frac{iV_{ud} g_2}{2} W^+ \cdot \left[1 - \frac{a}{2} (1 + \Sigma_V) \right] \left[\pi^0 - \left(\epsilon_1 - \frac{\Delta_A}{2} \sin \delta_P \right) \eta - \left(\epsilon_2 - \frac{\Delta_A}{2} \cos \delta_P \right) \eta' \right] \overset{\leftrightarrow}{\partial} \pi^- \\ &\quad - i\Delta_A \frac{V_{ud} g_2}{2} W^+ \left[\sin \delta_P \eta - \cos \delta_P \eta' \right] \overset{\leftrightarrow}{\partial} \pi^- - \frac{f_\pi g_2}{4} W^+ \left[V_{ud} \partial \pi^- + V_{us} \sqrt{z_A} \left(1 + \frac{\Delta_A}{4} \right) \partial K^- \right] \\ &\quad - \frac{ia g}{2} \rho^+ \cdot \left[(1 + \Sigma_V) \pi^- \overset{\leftrightarrow}{\partial} \pi^0 - \left(\epsilon_1 - \frac{\Delta_A}{2} \sin \delta_P \right) \pi^- \overset{\leftrightarrow}{\partial} \eta - \left(\epsilon_2 - \frac{\Delta_A}{2} \cos \delta_P \right) \pi^- \overset{\leftrightarrow}{\partial} \eta' \right], \end{aligned} \quad (118)$$

where all fields are renormalized. δ_P is related with the PS mixing in the one angle mixing scheme [31]; its definition is reminded in Appendix B below together with those for the ϵ_i .

The appearance of $W^\pm(\pi^0/\eta/\eta')\pi^\pm$ couplings should be noted; one should also note, about the $W^\pm(\eta/\eta')\pi^\pm$ couplings, that the contributions from \mathcal{L}_A and \mathcal{L}_V are not proportional in contrast with the $W^\pm\pi^0\pi^\pm$ case. Finally, it is also worth noting that the $\rho^\pm(\eta/\eta')\pi^\pm$ couplings in Equation (118) are needed in the transitions amplitudes for $\eta/\eta' \rightarrow \pi^+\pi^-\gamma$ in order to yield the right behavior at the chiral point.

A.3 The \mathcal{L}_{p^4} Lagrangian Piece \mathcal{L}_{z_3}

As for the \mathcal{L}_{z_3} Lagrangian, it writes in terms of ideal fields :

$$\begin{aligned} \mathcal{L}_{z_3} = & egz_3 s A_\mu \left[(1 + \xi_3) \rho_I^0{}^\mu + \frac{1}{3}(1 + \xi_8) \omega_I^\mu - \frac{\sqrt{2}}{3}(1 + \xi_8) \phi_I^\mu \right] \\ & + \frac{g_2 g z_3 s}{2} \left[\bar{V}_{ud} \rho_\mu^+ W_\mu^- + V_{ud} \rho_\mu^- W_\mu^+ \right] . \end{aligned} \quad (119)$$

It clearly allows for different $V\gamma$ and WV couplings, especially for the ρ meson.

A.4 The Renormalized Couplings of Vector Mesons to $K\bar{K}$

Let us first remind the coupling of the fully renormalized vector mesons to $\pi^+\pi^-$; having defined these as $g_{\pi^\pm}^V = ag\tilde{g}_{\pi^\pm}/2$, one has :

$$\tilde{g}_{\pi^\pm}^\rho = [1 + \Sigma_V + \xi_3] , \quad \tilde{g}_{\pi^\pm}^\omega = -[\psi_\omega + \alpha(s)] , \quad \tilde{g}_{\pi^\pm}^\phi = [\psi_\phi + \beta(s)] . \quad (120)$$

Using the Lagrangian in Section A.1 and Eq. (38) one can derive the renormalized coupling of vector mesons to $K\bar{K}$ pairs. Defining:

$$\begin{cases} \tilde{g}_{K^\pm}^\rho = \left(1 - \frac{\Delta_A}{2}\right) \left\{ 1 + \Sigma_V + \xi_3 + [\psi_\omega + \alpha(s)] + \sqrt{2}z_V[\psi_\phi + \beta(s)] \right\} , \\ \tilde{g}_{K^\pm}^\omega = \left(1 - \frac{\Delta_A}{2}\right) \left\{ 1 + \Sigma_V + \frac{2}{3}(1 - z_V)\xi_0 + \frac{1 + 2z_V}{3}\xi_8 - [\psi_\omega + \alpha(s)] + \sqrt{2}z_V[\psi_0 + \gamma(s)] \right\} , \\ \tilde{g}_{K^\pm}^\phi = \left(1 - \frac{\Delta_A}{2}\right) \left\{ -\sqrt{2} \left[z_V - \frac{1}{3}(1 - z_V)\xi_0 + \frac{1 + 2z_V}{3}\xi_8 \right] + [\psi_\phi + \beta(s)] + [\psi_0 + \gamma(s)] \right\} , \end{cases} \quad (121)$$

the couplings involved in form factors and cross-sections are given by $G_{K^+K^-}^V = ag/[4z_A] \tilde{g}_{K^\pm}^V$. One also has :

$$\begin{cases} \tilde{g}_{K^0}^\rho = \left(1 + \frac{\Delta_A}{2}\right) \left\{ 1 + \Sigma_V + \xi_3 - [\psi_\omega + \alpha(s)] - \sqrt{2}z_V[\psi_\phi + \beta(s)] \right\} , \\ \tilde{g}_{K^0}^\omega = -\left(1 + \frac{\Delta_A}{2}\right) \left\{ 1 + \Sigma_V + \frac{2}{3}(1 - z_V)\xi_0 + \frac{1 + 2z_V}{3}\xi_8 + [\psi_\omega + \alpha(s)] + \sqrt{2}z_V[\psi_0 + \gamma(s)] \right\} , \\ \tilde{g}_{K^0}^\phi = \left(1 + \frac{\Delta_A}{2}\right) \left\{ \sqrt{2} \left[z_V - \frac{1}{3}(1 - z_V)\xi_0 + \frac{1 + 2z_V}{3}\xi_8 \right] + [\psi_\phi + \beta(s)] - [\psi_0 + \gamma(s)] \right\} , \end{cases} \quad (122)$$

and the full couplings are given by $G_{K^0\bar{K}^0}^V = ag/[4z_A] \tilde{g}_{K^0}^V$. One cancels out here and in the following the dependence upon Δ_V . One should also note that all these couplings depend on s , the square energy flowing through the relevant vector line.

A.5 The $V - \gamma$ Transition Loop Terms

As seen in the main text, the $V - \gamma$ transitions amplitudes write :

$$F_{V\gamma}^e(s) = f_{V\gamma} - c_{V\gamma} z_3 s - \Pi_{V\gamma}(s)$$

for each of $V = \rho_R^0, \omega_R, \phi_R$. In this Section, one displays the expression for the loop terms $\Pi_{V\gamma}(s)$ in terms of the basic loop functions denoted $\Pi_\pi^e(s)$, $\Pi_{K^\pm}^e(s)$ and $\Pi_{K^0}^e(s)$ and defined in Subsection 11.2. For the sake of conciseness, it is convenient to define :

$$\begin{aligned}\tilde{g}_{\pi^\pm}^\gamma &= \left[1 - \frac{a}{2}[1 + \Sigma_V]\right] , \\ \tilde{g}_{K^\pm}^\gamma &= \left[1 - \frac{a}{6z_A}\left[2 + z_V + 2\Sigma_V - \frac{3}{2}\Delta_A\right]\right] , \quad \tilde{g}_{K^0}^\gamma = -\frac{a}{6z_A}(1 - z_V + \Sigma_V) ,\end{aligned}\tag{123}$$

neglecting the $\mathcal{O}(\epsilon^2)$ terms. These couplings do not depend on the "angles" $\alpha(s)$, $\beta(s)$ and $\gamma(s)$.

Using these definitions and those displayed in the Subsection just above, one finds :

$$\left\{ \begin{array}{l} \Pi_{\rho\gamma} = \frac{\tilde{g}_{\pi^\pm}^\gamma \tilde{g}_{\pi^\pm}^\rho}{G_\pi} \Pi_\pi^e(s) + \frac{\tilde{g}_{K^\pm}^\gamma \tilde{g}_{K^\pm}^\rho}{G_K} \Pi_{K^\pm}^e(s) + \frac{\tilde{g}_{K^0}^\gamma \tilde{g}_{K^0}^\rho}{G_K} \Pi_{K^0}^e(s) , \\ \Pi_{\omega\gamma} = \frac{\tilde{g}_{\pi^\pm}^\gamma \tilde{g}_{\pi^\pm}^\omega}{G_\pi} \Pi_\pi^e(s) + \frac{\tilde{g}_{K^\pm}^\gamma \tilde{g}_{K^\pm}^\omega}{G_K} \Pi_{K^\pm}^e(s) + \frac{\tilde{g}_{K^0}^\gamma \tilde{g}_{K^0}^\omega}{G_K} \Pi_{K^0}^e(s) , \\ \Pi_{\phi\gamma} = \frac{\tilde{g}_{\pi^\pm}^\gamma \tilde{g}_{\pi^\pm}^\phi}{G_\pi} \Pi_\pi^e(s) + \frac{\tilde{g}_{K^\pm}^\gamma \tilde{g}_{K^\pm}^\phi}{G_K} \Pi_{K^\pm}^e(s) + \frac{\tilde{g}_{K^0}^\gamma \tilde{g}_{K^0}^\phi}{G_K} \Pi_{K^0}^e(s) . \end{array} \right.\tag{124}$$

Expanding Equations (124) in order to rather parametrize in terms of $\Pi_{K^\pm}^e$ and $\Pi_{K^0}^e$ (see Subsection 11.2) allows to exhibit the terms of order $\mathcal{O}(\epsilon^2)$ in breakings which can be dropped out.

B Pseudoscalar Field Renormalization : A Brief Reminder

As already stated, one goes on using unchanged the breaking procedure in the \mathcal{L}_A sector of the HLS model as defined in [25]. The broken \mathcal{L}_A Lagrangian displayed in Eq. (8) implies a first step field redefinition in order to make the pseudoscalar kinetic energy term canonical. Additionally, as BHLS and BHLS₂ also include the 't Hooft determinant terms [32], the pseudoscalar kinetic energy receives an additional piece :

$$\mathcal{L}'_{\text{tHooft}} = \frac{1}{2} \lambda \partial_\mu \eta_0 \partial^\mu \eta_0 + \dots ,\tag{125}$$

where η_0 is the singlet PS field and λ is a parameter to be fixed. This term imposes a second step renormalization [31] of the (π^0, η, η') sector.

The first step renormalization turns out to define the (step one) renormalized pseudoscalar field matrix P^{R_1} in term of the bare one P by [25] :

$$P^{R_1} = X_A^{1/2} P X_A^{1/2} , \quad \text{where } X_A = \text{Diag}\left(1 + \frac{\Delta_A}{2}, 1 - \frac{\Delta_A}{2}, z_A\right) .\tag{126}$$

Some pseudoscalar (PS) fields happen to be fully renormalized after this first step; they are

related to their bare partners by :

$$\begin{cases} \pi_{\text{bare}}^{\pm} = \pi^{\pm}, \\ K_{\text{bare}}^{\pm} = \frac{1}{\sqrt{z_A}}(1 - \frac{\Delta_A}{4})K^{\pm}, \\ K_{\text{bare}}^0 = \frac{1}{\sqrt{z_A}}(1 + \frac{\Delta_A}{4})K^0. \end{cases} \quad (127)$$

These renormalized fields have already been used to derive the Lagrangians given in Appendix A. As for the other PS fields, the first step renormalization leads to the $R1$ renormalized PS fields :

$$\begin{cases} \pi_0^{\text{bare}} = \pi_0^{R1} - \frac{\Delta_A}{2\sqrt{3}}\eta_8^{R1} - \frac{\Delta_A}{\sqrt{6}}\eta_0^{R1}, \\ \eta_0^{\text{bare}} = -\frac{\Delta_A}{\sqrt{6}}\pi_0^{R1} + \frac{\sqrt{2}}{3}\frac{z_A - 1}{z_A}\eta_8^{R1} + \frac{1}{3}\frac{2z_A + 1}{z_A}\eta_0^{R1}, \\ \eta_8^{\text{bare}} = -\frac{\Delta_A}{2\sqrt{3}}\pi_0^{R1} + \frac{1}{3}\frac{z_A + 2}{z_A}\eta_8^{R1} + \frac{\sqrt{2}}{3}\frac{z_A - 1}{z_A}\eta_0^{R1}. \end{cases} \quad (128)$$

The second step renormalization required by the 't Hooft term gives the R renormalized fields [31] :

$$\begin{cases} \pi_0^{R1} = \pi_0^R, \\ \eta_8^{R1} = \frac{1 + v \cos^2 \beta}{1 + v}\eta_8^R - \frac{v \sin \beta \cos \beta}{1 + v}\eta_0^R, \\ \eta_0^{R1} = -\frac{v \sin \beta \cos \beta}{1 + v}\eta_8^R + \frac{1 + v \sin^2 \beta}{1 + v}\eta_0^R, \end{cases} \quad (129)$$

where :

$$\begin{cases} \cos \beta = \frac{2z_A + 1}{\sqrt{3(2z_A^2 + 1)}}, \quad \sin \beta = \frac{\sqrt{2}(z_A - 1)}{\sqrt{3(2z_A^2 + 1)}} \\ v = \sqrt{1 + \lambda \frac{(2z_A^2 + 1)}{3z_A^2}} - 1 \simeq \frac{\lambda}{2} \frac{(2z_A^2 + 1)}{3z_A^2}. \end{cases} \quad (130)$$

The parameters affecting the PS fields submitted to fit are thus Δ_A , z_A and λ (or alternatively v).

The $\pi^0 - \eta - \eta'$ mixing is supplemented by defining the physically observable PS fields in terms of their R renormalized partners by [144, 25] :

$$\begin{cases} \pi_R^0 = \pi^0 - \epsilon_1 \eta - \epsilon_2 \eta', \\ \eta_R^8 = \cos \theta_P(\eta + \epsilon_1 \pi^0) + \sin \theta_P(\eta' + \epsilon_2 \pi^0), \\ \eta_R^0 = -\sin \theta_P(\eta + \epsilon_1 \pi^0) + \cos \theta_P(\eta' + \epsilon_2 \pi^0), \end{cases} \quad (131)$$

which exhibits three more parameters to be determined by fit. The singlet-octet mixing angle θ_P occurring here is expected in the range $(-10^\circ \div -15^\circ)$ and is also algebraically related to

the usual θ_8 [31]. In order to express the forthcoming VVP and AVP coupling constants, the mixing angle δ_P defined by [25] :

$$\begin{cases} \sin \theta_P = \frac{1}{\sqrt{3}}(\cos \delta_P + \sqrt{2} \sin \delta_P), \\ \cos \theta_P = \frac{1}{\sqrt{3}}(\sqrt{2} \cos \delta_P - \sin \delta_P), \end{cases} \quad (132)$$

happens to be more appropriate than θ_P . On the other hand, it is also useful to define the combinations [25] :

$$\begin{cases} x = 1 - \frac{3z_A^2}{2z_A^2 + 1}v, \\ x' = 1 - \frac{3z_A}{2z_A^2 + 1}v, \\ x'' = 1 - \frac{3}{2z_A^2 + 1}v, \end{cases} \quad (133)$$

where v is the nonet symmetry breaking parameter defined in Equations(130). x , x' and x'' reflect the various ways by which nonet symmetry breaking occurs in the PS sector of broken HLS Lagrangians.

C The VVP Lagrangian in Terms of Ideal Vector Fields

The π^0 , η and η' pieces of the \mathcal{L}_{VVP} Lagrangian are given separately just below. If the PS fields occurring in this Appendix are renormalized by the procedure reminded in Appendix B, it is simpler to express the various VVP Lagrangian pieces in terms of the ideal vector fields. The derivation of the couplings involving the renormalized fields is given in the main text.

We split up the VVP Lagrangian into the pieces involving the renormalized π^0 , π^\pm , η and η' pieces, below. As for the π^0 , we have :

$$\begin{aligned} \mathcal{L}_{VVP}(\pi^0) = & \frac{C}{2} \epsilon^{\mu\nu\alpha\beta} \left\{ \left[\left(1 + \frac{2\xi_0}{3} + \frac{\xi_8}{3} \right) \partial_\mu \omega_\nu^I + \frac{\sqrt{2}}{3} (\xi_0 - \xi_8) \partial_\mu \phi_\nu^I \right] \times \right. \\ & \left. \left[\partial_\alpha \rho_\beta^+ \pi^- + \partial_\alpha \rho_\beta^- \pi^+ + (1 + \xi_3) \partial_\alpha \rho_\beta^I \pi^0 \right] \right. \\ & \left. + \left[\tilde{g}_{\omega\pi^0} \partial_\mu \omega_\nu^I \partial_\alpha \omega_\beta^I + \tilde{g}_{\rho\pi^0} \partial_\mu \rho_\nu^I \partial_\alpha \rho_\beta^I + \tilde{g}_{\phi\pi^0} \partial_\mu \phi_\nu^I \partial_\alpha \phi_\beta^I + \tilde{g}_{\rho^\pm\pi^0} \partial_\mu \rho_\nu^\pm \partial_\alpha \rho_\beta^\mp \right] \pi^0 \right\}, \end{aligned} \quad (134)$$

where :

$$\left\{ \begin{array}{l} C = -\frac{N_c g^2 c_3}{4\pi^2 f_\pi}, \\ \tilde{g}_{\rho^\pm \pi^0}^0 = 2\tilde{g}_{\rho\pi^0}^0 = \epsilon_2 \cos \delta_P - \epsilon_1 \sin \delta_P - \frac{\Delta_A}{2}, \\ \tilde{g}_{\omega\pi^0}^0 = \frac{1}{2} \left[\epsilon_2 \cos \delta_P - \epsilon_1 \sin \delta_P - \frac{\Delta_A}{2} \right], \\ \tilde{g}_{\phi\pi^0}^0 = -\frac{1}{z_A \sqrt{2}} [\epsilon_1 \cos \delta_P + \epsilon_2 \sin \delta_P]. \end{array} \right. \quad (135)$$

The $VV\eta$ Lagrangian is given by :

$$\begin{aligned} \mathcal{L}_{VVP}(\eta) = & \frac{C}{2} \epsilon^{\mu\nu\alpha\beta} \left\{ \tilde{g}_{\omega\phi\eta}^0 \partial_\mu \omega_\nu^I \partial_\alpha \phi_\beta^I + \tilde{g}_{\rho\omega\eta}^0 \partial_\mu \omega_\nu^I \partial_\alpha \rho_\beta^I + \tilde{g}_{\rho^\pm \eta} \partial_\mu \rho_\nu^+ \partial_\alpha \rho_\beta^- \right. \\ & \left. + \tilde{g}_{\omega\eta} \partial_\mu \omega_\nu^I \partial_\alpha \omega_\beta^I + \tilde{g}_{\rho\eta} \partial_\mu \rho_\nu^I \partial_\alpha \rho_\beta^I + \tilde{g}_{\phi\eta} \partial_\mu \phi_\nu^I \partial_\alpha \phi_\beta^I \right\} \eta, \end{aligned} \quad (136)$$

with :

$$\left\{ \begin{array}{l} \tilde{g}_{\omega\phi\eta}^0 = \frac{1}{3z_A} [2 \cos \delta_P + z_A \sqrt{2} \sin \delta_P] (\xi_8 - \xi_0), \\ \tilde{g}_{\rho\omega\eta}^0 = \left[\frac{\Delta_A}{2} \sin \delta_P - \epsilon_1 \right], \\ \tilde{g}_{\rho^\pm \eta}^0 = \frac{1}{3} [\sqrt{2}(1-x') \cos \delta_P - (1+2x) \sin \delta_P], \\ \tilde{g}_{\rho\eta}^0 = \frac{1}{6} [\sqrt{2}(1-x') \cos \delta_P - (1+2x) \sin \delta_P - 6\xi_3 \sin \delta_P], \\ \tilde{g}_{\omega\eta}^0 = \frac{1}{6} [\sqrt{2}(1-x') \cos \delta_P - (1+2x+4\xi_0+2\xi_8) \sin \delta_P], \\ \tilde{g}_{\phi\eta}^0 = -\frac{1}{6z_A} [\sqrt{2}(2+x''+2\xi_0+4\xi_8) \cos \delta_P - 2(1-x') \sin \delta_P]. \end{array} \right. \quad (137)$$

The $VV\eta'$ Lagrangian is given by :

$$\begin{aligned} \mathcal{L}_{VVP}(\eta') = & \frac{C}{2} \epsilon^{\mu\nu\alpha\beta} \left\{ \tilde{g}_{\omega\phi\eta'}^0 \partial_\mu \omega_\nu^I \partial_\alpha \phi_\beta^I + \tilde{g}_{\rho\omega\eta'}^0 \partial_\mu \omega_\nu^I \partial_\alpha \rho_\beta^I + \tilde{g}_{\rho^\pm \eta'} \partial_\mu \rho_\nu^+ \partial_\alpha \rho_\beta^- \right. \\ & \left. + \tilde{g}_{\omega\eta'} \partial_\mu \omega_\nu^I \partial_\alpha \omega_\beta^I + \tilde{g}_{\rho\eta'} \partial_\mu \rho_\nu^I \partial_\alpha \rho_\beta^I + \tilde{g}_{\phi\eta'} \partial_\mu \phi_\nu^I \partial_\alpha \phi_\beta^I \right\} \eta', \end{aligned} \quad (138)$$

with :

$$\left\{ \begin{array}{l} \tilde{g}_{\omega\phi\eta'}^0 = \frac{1}{3z_A} \left[2 \sin \delta_P - z_A \sqrt{2} \cos \delta_P \right] (\xi_8 - \xi_0) , \\ \tilde{g}_{\rho\omega\eta'}^0 = - \left[\frac{\Delta_A}{2} \cos \delta_P + \epsilon_2 \right] , \\ \tilde{g}_{\rho^\pm\eta'}^0 = \frac{1}{3} \left[\sqrt{2}(1 - x') \sin \delta_P + (1 + 2x) \cos \delta_P \right] , \\ \tilde{g}_{\rho\eta'}^0 = \frac{1}{6} \left[\sqrt{2}(1 - x') \sin \delta_P + (1 + 2x) \cos \delta_P + 6\xi_3 \cos \delta_P \right] , \\ \tilde{g}_{\omega\eta'}^0 = \frac{1}{6} \left[\sqrt{2}(1 - x') \sin \delta_P + (1 + 2x + 4\xi_0 + 2\xi_8) \cos \delta_P \right] , \\ \tilde{g}_{\phi\eta'}^0 = -\frac{1}{6z_A} \left[\sqrt{2}(2 + x'' + 2\xi_0 + 4\xi_8) \sin \delta_P + 2(1 - x') \cos \delta_P \right] . \end{array} \right. \quad (139)$$

Finally, it is worth extracting out from Eq. (135) the part involving a charged ρ meson for illustrative purposes. This write :

$$\mathcal{L}_{VVP}(\rho^\pm, \pi^0) = \frac{C}{2} \epsilon^{\mu\nu\alpha\beta} \left[\tilde{g}_{\omega\rho^\pm}^\pm \partial_\mu \omega_\nu^I + \tilde{g}_{\phi\rho^\pm}^\pm \partial_\mu \phi_\nu^I \right] \left[\partial_\alpha \rho_\beta^+ \pi^- + \partial_\alpha \rho_\beta^- \pi^+ \right] , \quad (140)$$

with :

$$\tilde{g}_{\omega\rho^\pm}^\pm = \left(1 + \frac{2\xi_0}{3} + \frac{\xi_8}{3} \right) , \quad \tilde{g}_{\phi\rho^\pm}^\pm = \frac{\sqrt{2}}{3} (\xi_0 - \xi_8) . \quad (141)$$

D The *AAP* and *APPP* Lagrangians in the HLS Framework

For the reader's convenience, we have found appropriate to remind the expressions for the *AAP* Lagrangian and for the part of the *APPP* Lagrangian relevant for the annihilation process $e^+e^- \rightarrow \pi^0\pi^+\pi^-$. These have been derived in [25]. One first have :

$$\mathcal{L}_{AAP} = -\frac{3\alpha_{\text{em}}}{\pi f_\pi} (1 - c_4) \epsilon^{\alpha\beta\mu\nu} \partial_\alpha A_\beta \partial_\mu A_\nu \left[g_{\pi^0\gamma\gamma} \frac{\pi^0}{6} + g_{\eta\gamma\gamma} \frac{\eta}{2\sqrt{3}} + g_{\eta'\gamma\gamma} \frac{\eta'}{2\sqrt{3}} \right] , \quad (142)$$

with :

$$\left\{ \begin{array}{l} g_{\pi^0\gamma\gamma} = 1 - \frac{5\Delta_A}{6} + \frac{\epsilon_1}{\sqrt{3}} \left\{ \frac{5z_A - 2}{3z_A} \cos \theta_P - \sqrt{2} \frac{5z_A + 1}{3z_A} \sin \theta_P \right\} \\ \quad + \frac{\epsilon_2}{\sqrt{3}} \left\{ \frac{5z_A - 2}{3z_A} \sin \theta_P + \sqrt{2} \frac{5z_A + 1}{3z_A} \cos \theta_P \right\} , \\ g_{\eta\gamma\gamma} = \frac{\cos \theta_P}{3} \left\{ \frac{5z_A - 2}{3z_A(1+v)} + v \frac{1 + 2z_A}{1 + 2z_A^2} - \frac{\Delta_A}{2} \right\} \\ \quad - \sqrt{2} \frac{\sin \theta_P}{3} \left\{ \frac{5z_A + 1}{3z_A(1+v)} + v \frac{1 - z_A}{1 + 2z_A^2} - \frac{\Delta_A}{2} \right\} - \frac{\epsilon_1}{\sqrt{3}} , \\ g_{\eta'\gamma\gamma} = \frac{\sin \theta_P}{3} \left\{ \frac{5z_A - 2}{3z_A(1+v)} + v \frac{1 + 2z_A}{1 + 2z_A^2} - \frac{\Delta_A}{2} \right\} \\ \quad + \sqrt{2} \frac{\cos \theta_P}{3} \left\{ \frac{5z_A + 1}{3z_A(1+v)} + v \frac{1 - z_A}{1 + 2z_A^2} - \frac{\Delta_A}{2} \right\} - \frac{\epsilon_2}{\sqrt{3}} , \end{array} \right. \quad (143)$$

using the renormalized PS fields defined in Appendix B and their specific parameters.

The pion sector of the $APPP$ Lagrangian is [25] :

$$\mathcal{L}_{APPP} = -iE g_{\pi^0\pi^+\pi^-\gamma} \epsilon^{\mu\nu\alpha\beta} A_\mu \partial_\nu \pi^0 \partial_\alpha \pi^- \partial_\beta \pi^+ , \quad (144)$$

with

$$E = -\frac{e}{\pi^2 f_\pi^3} \left[1 - \frac{3}{4}(c_1 - c_2 + c_4) \right] \quad (145)$$

and :

$$g_{\pi^0\pi^+\pi^-\gamma} = \frac{1}{4} \left[1 - \frac{\Delta_A}{2} + \frac{\cos \theta_P}{\sqrt{3}} \{ \epsilon_1 + \sqrt{2}\epsilon_2 \} - \frac{\sin \theta_P}{\sqrt{3}} \{ \sqrt{2}\epsilon_1 - \epsilon_2 \} \right] . \quad (146)$$

One may prefer reexpressing this formula by :

$$g_{\pi^0\pi^+\pi^-\gamma} = \frac{1}{4} \left[1 - \frac{\Delta_A}{2} + \epsilon_2 \cos \delta_P - \epsilon_1 \sin \delta_P \right] , \quad (147)$$

using the angle δ_P defined by Equations (132).

E The $VPPP$ Lagrangian and its Renormalization

The $VPPP$ anomalous Lagrangian in terms of *ideal* vector fields can be written :

$$\left\{ \begin{array}{l} \mathcal{L}_{VPPP} = iD \epsilon^{\mu\nu\alpha\beta} \left\{ \left[g_{\rho\pi}^0 \partial_\nu \pi^0 + g_{\rho\eta}^0 \partial_\nu \eta + g_{\rho\eta'}^0 \partial_\nu \eta' \right] \rho_\mu^I , \right. \\ \quad \left. + \left[g_{\omega\pi}^0 \partial_\nu \pi^0 + g_{\omega\eta}^0 \partial_\nu \eta + g_{\omega\eta'}^0 \partial_\nu \eta' \right] \omega_\mu^I + g_{\phi\pi}^0 \partial_\nu \pi^0 \phi_\mu^I \right\} \partial_\alpha \pi^- \partial_\beta \pi^+ , \\ \text{with } D = -\frac{3g(c_1 - c_2 - c_3)}{4\pi^2 f_\pi^3} , \end{array} \right. \quad (148)$$

where one has limited oneself to display the $P_0\pi^+\pi^-$ sector. The leading terms of these couplings are :

$$\begin{cases} g_{\rho\pi^0}^0 = \frac{1}{4} \left[\frac{\Delta_A}{2} + \epsilon_1 \sin \delta_P - \epsilon_2 \cos \delta_P \right] , \\ g_{\omega\pi^0}^0 = -\frac{3}{4} \left[1 + \frac{2\xi_0 + \xi_8}{3} \right] , \\ g_{\phi\pi^0}^0 = -\frac{\sqrt{2}}{4} [\xi_0 - \xi_8] , \end{cases} \quad (149)$$

$$\begin{cases} g_{\rho\eta}^0 = -\frac{1}{12} \left[(1 - x') \sqrt{2} \cos \delta_P - \{(1 + 2x) + 3\xi_3\} \sin \delta_P \right] , \\ g_{\omega\eta}^0 = -\frac{3}{4} \left[\frac{\Delta_A}{2} \sin \delta_P - \epsilon_1 \right] , \\ g_{\phi\eta}^0 = 0 , \end{cases} \quad (150)$$

$$\begin{cases} g_{\rho\eta'}^0 = -\frac{1}{12} \left[(1 - x') \sqrt{2} \sin \delta_P + \{(1 + 2x) + 3\xi_3\} \cos \delta_P \right] , \\ g_{\omega\eta'}^0 = \frac{3}{4} \left[\frac{\Delta_A}{2} \cos \delta_P + \epsilon_2 \right] , \\ g_{\phi\eta'}^0 = 0 . \end{cases} \quad (151)$$

One may note, once again the clarity reached by using δ_P instead of θ_P .

The couplings to the renormalized fields can be derived from those to the ideal fields by means of the $\mathcal{R}(s)$ matrix defined in the body of the text :

$$g_P^R = \widetilde{\mathcal{R}}(s) g_{P_0}^0 \quad (152)$$

the elements of the $g_{P_0}^0$ vectors being defined in Equations (149), Equations (150) or Equations (151) for resp. the $P_0 = \pi^0$ or η, η' mesons.

For the couplings of the ϕ meson, at leading order in breaking, one gets :

$$g_{\phi\pi^0}^R(s) = -\frac{3}{4} \left\{ [\psi_0 + \gamma(s)] - \frac{\sqrt{2}}{3} [\xi_0 - \xi_8] \right\} . \quad (153)$$

One clearly sees that, at the ϕ mass, one obtains a non-vanishing direct coupling of the ϕ to 3 pions, additionally s -dependent.

References

- [1] V. V. Anashin *et al.*, Phys. Lett. **B770**, 174 (2017), 1610.02827, Measurement of R between 1.84 and 3.05 GeV at the KEDR detector.
- [2] V. V. Anashin *et al.*, Phys. Lett. **B753**, 533 (2016), 1510.02667, Measurement of R_{uds} and R between 3.12 and 3.72 GeV at the KEDR detector.

- [3] Particle Data Group, C. Patrignani *et al.*, Chin..Phys. **C40**, 010001 (2016), Review of Particle Physics (RPP).
- [4] F. Jegerlehner, EPJ Web Conf. **166**, 00022 (2018), 1705.00263, Muon $g - 2$ theory: The hadronic part.
- [5] F. Jegerlehner, Springer Tracts Mod. Phys. **274**, pp.1 (2017), The Anomalous Magnetic Moment of the Muon.
- [6] J. Gasser and H. Leutwyler, Annals Phys. **158**, 142 (1984), Chiral Perturbation Theory to One Loop.
- [7] J. Gasser and H. Leutwyler, Nucl. Phys. **B250**, 465 (1985), Chiral Perturbation Theory: Expansions in the Mass of the Strange Quark.
- [8] S. Aoki *et al.*, Eur. Phys. J. **C74**, 2890 (2014), 1310.8555, Review of lattice results concerning low-energy particle physics.
- [9] ETM, F. Burger *et al.*, JHEP **1402**, 099 (2014), 1308.4327, Four-Flavour Leading-Order Hadronic Contribution To The Muon Anomalous Magnetic Moment.
- [10] F. Burger, G. Hotzel, K. Jansen, and M. Petschlies, (2015), 1501.05110, Leading-order hadronic contributions to the electron and tau anomalous magnetic moments.
- [11] B. Chakraborty *et al.*, Phys. Rev. **D96**, 034516 (2017), 1601.03071, The hadronic vacuum polarization contribution to a_μ from full lattice QCD.
- [12] M. Della Morte *et al.*, (2017), 1705.01775, The hadronic vacuum polarization contribution to the muon $g - 2$ from lattice QCD.
- [13] Muon G-2, G. W. Bennett *et al.*, Phys. Rev. **D73**, 072003 (2006), hep-ex/0602035, Final report of the muon E821 anomalous magnetic moment measurement at BNL.
- [14] B. L. Roberts, Chin. Phys. **C34**, 741 (2010), 1001.2898, Status of the Fermilab Muon ($g - 2$) Experiment.
- [15] Fermilab P989 Collaboration, B. Lee Roberts, Nucl.Phys.Proc.Suppl. **218**, 237 (2011), The Fermilab muon ($g-2$) project.
- [16] Muon $g-2$ Collaboration, J. Grange *et al.*, (2015), 1501.06858, Muon ($g-2$) Technical Design Report.
- [17] J-PARC New $g-2$ /EDM experiment Collaboration, H. Iinuma, J.Phys.Conf.Ser. **295**, 012032 (2011), New approach to the muon $g-2$ and EDM experiment at J-PARC.
- [18] M. Harada and K. Yamawaki, Phys. Rept. **381**, 1 (2003), hep-ph/0302103, Hidden local symmetry at loop: A new perspective of composite gauge boson and chiral phase transition.
- [19] G. Ecker, J. Gasser, A. Pich, and E. de Rafael, Nucl.Phys. **B321**, 311 (1989), The Role of Resonances in Chiral Perturbation Theory.

- [20] G. Ecker, J. Gasser, H. Leutwyler, A. Pich, and E. de Rafael, Phys.Lett. **B223**, 425 (1989), Chiral Lagrangians for Massive Spin 1 Fields.
- [21] M. Bando, T. Kugo, and K. Yamawaki, Phys. Rept. **164**, 217 (1988), Nonlinear Realization and Hidden Local Symmetries.
- [22] T. Fujiwara, T. Kugo, H. Terao, S. Uehara, and K. Yamawaki, Prog. Theor. Phys. **73**, 926 (1985), Nonabelian Anomaly and Vector Mesons as Dynamical Gauge Bosons of Hidden Local Symmetries.
- [23] M. Benayoun, P. David, L. DelBuono, and O. Leitner, Eur. Phys. J. **C65**, 211 (2010), 0907.4047, A Global Treatment Of VMD Physics Up To The ϕ : I. e^+e^- Annihilations, Anomalies And Vector Meson Partial Widths.
- [24] M. Benayoun, P. David, L. DelBuono, and O. Leitner, Eur. Phys. J. **C68**, 355 (2010), 0907.5603, A Global Treatment Of VMD Physics Up To The ϕ : II. τ Decay and Hadronic Contributions To $g-2$.
- [25] M. Benayoun, P. David, L. DelBuono, and F. Jegerlehner, Eur.Phys. J. **C72**, 1848 (2012), 1106.1315, Upgraded Breaking Of The HLS Model: A Full Solution to the $\tau^- \rightarrow e^+e^-$ and ϕ Decay Issues And Its Consequences On $g-2$ VMD Estimates.
- [26] M. Benayoun, P. David, L. DelBuono, and F. Jegerlehner, Eur.Phys. J. **C73**, 2453 (2013), 1210.7184, An Update of the HLS Estimate of the Muon $g-2$.
- [27] M. Benayoun, P. David, L. DelBuono, and F. Jegerlehner, Eur. Phys. J. **C75**, 613 (2015), 1507.02943, Muon $g - 2$ estimates: can one trust effective Lagrangians and global fits?
- [28] M. Bando, T. Kugo, and K. Yamawaki, Nucl. Phys. **B259**, 493 (1985), On the Vector Mesons as Dynamical Gauge Bosons of Hidden Local Symmetries.
- [29] M. Benayoun, P. David, L. DelBuono, O. Leitner, and H. B. O'Connell, Eur. Phys. J. **C55**, 199 (2008), hep-ph/0711.4482, The Dipion Mass Spectrum In e^+e^- Annihilation and tau Decay: A Dynamical (ρ^0 , ω , ϕ) Mixing Approach.
- [30] M. Benayoun, H. B. O'Connell, and A. G. Williams, Phys. Rev. **D59**, 074020 (1999), hep-ph/9807537, Vector meson dominance and the ρ meson.
- [31] M. Benayoun, L. DelBuono, and H. B. O'Connell, Eur. Phys. J. **C17**, 593 (2000), hep-ph/9905350, VMD, the WZW Lagrangian and ChPT: The third mixing angle.
- [32] G. 't Hooft, Phys. Rept. **142**, 357 (1986), How Instantons Solve the U(1) Problem.
- [33] A. Bramon, A. Grau, and G. Pancheri, Phys. Lett. **B345**, 263 (1995), hep-ph/9411269, Effective chiral lagrangians with an SU(3) broken vector meson sector.
- [34] M. Benayoun and H. B. O'Connell, Phys. Rev. **D58**, 074006 (1998), hep-ph/9804391, SU(3) breaking and hidden local symmetry.

- [35] M. Hashimoto, Phys. Rev. **D54**, 5611 (1996), hep-ph/9605422, Hidden local symmetry for anomalous processes with isospin/SU(3) breaking effects.
- [36] BESIII, M. Ablikim *et al.*, Phys. Rev. Lett. **120**, 242003 (2018), 1712.01525, Precision Study of $\eta' \rightarrow \gamma \pi^+ \pi^-$ Decay Dynamics.
- [37] L.-Y. Dai, X.-W. Kang, U.-G. Meiner, X.-Y. Song, and D.-L. Yao, Phys. Rev. **D97**, 036012 (2018), 1712.02119, Amplitude analysis of the anomalous decay $\eta' \rightarrow \pi^+ \pi^- \gamma$.
- [38] G. J. Hung and J. J. Sakurai, Nucl. Phys. **B143**, 81 (1978), γW_0 mixing as an alternative to unified weak electromagnetic gauge theories.
- [39] F. Klingl, N. Kaiser, and W. Weise, Z. Phys. **A356**, 193 (1996), hep-ph/9607431, Effective Lagrangian approach to vector mesons, their structure and decays.
- [40] M. Davier *et al.*, Eur. Phys. J. **C66**, 127 (2010), 0906.5443, The Discrepancy Between τ and e^+e^- Spectral Functions Revisited and the Consequences for the Muon Magnetic Anomaly.
- [41] M. Davier, A. Hoecker, B. Malaescu, and Z. Zhang, Eur. Phys. J. **C71**, 1515 (2011), 1010.4180, Reevaluation of the Hadronic Contributions to the Muon g-2 and to $\alpha(MZ)$.
- [42] M. Benayoun, EPJ Web Conf. **118**, 01001 (2016), 1511.01329, The HLS approach to $(g-2)_\mu$: A Solution to the τ versus e^+e^- Puzzle.
- [43] F. Jegerlehner and R. Szafron, Eur. Phys. J. **C71**, 1632 (2011), 1101.2872, $\rho^0 - \gamma$ mixing in the neutral channel pion form factor $|F_\pi|^2$ and its role in comparing e^+e^- with τ spectral functions.
- [44] M. Benayoun, L. DelBuono, P. Leruste, and H. B. O'Connell, Eur. Phys. J. **C17**, 303 (2000), nucl-th/0004005, An effective approach to VMD at one loop order and the departures from ideal mixing for vector mesons.
- [45] G. J. Gounaris and J. J. Sakurai, Phys. Rev. Lett. **21**, 244 (1968), Finite width corrections to the vector meson dominance prediction for $\rho \rightarrow e^+e^-$.
- [46] Belle, M. Fujikawa *et al.*, Phys. Rev. **D78**, 072006 (2008), 0805.3773, High-Statistics Study of the $\tau^- \rightarrow \pi^- \pi^0 \nu_\tau$ Decay.
- [47] NA7, S. R. Amendolia *et al.*, Nucl. Phys. **B277**, 168 (1986), A Measurement of the Space - Like Pion Electromagnetic Form-Factor.
- [48] NA7, S. R. Amendolia *et al.*, Phys. Lett. **B178**, 435 (1986), A Measurement of the Kaon Charge Radius.
- [49] E. Cremmer and M. Gourdin, Nucl. Phys. **B9**, 451 (1969), Radiative corrections to $\phi \rightarrow K^+ K^-$ decay.

- [50] A. Bramon, R. Escribano, J. L. L. M., and G. Pancheri, Phys. Lett. **B486**, 406 (2000), hep-ph/0003273, The ratio $\phi \rightarrow K^+ K^- / K^0 \bar{K}^0$.
- [51] J. Gluza, A. Hoefer, S. Jadach, and F. Jegerlehner, Eur. Phys. J. **C28**, 261 (2003), hep-ph/0212386, Measuring the FSR-inclusive $\pi^+ \pi^-$ cross section.
- [52] J. Wess and B. Zumino, Phys. Lett. **B37**, 95 (1971), Consequences of anomalous Ward identities.
- [53] E. Witten, Nucl. Phys. **B223**, 422 (1983), Global Aspects of Current Algebra.
- [54] E. A. Kuraev and Z. K. Silagadze, Phys. Atom. Nucl. **58**, 1589 (1995), hep-ph/9502406, Once more about the $\omega \rightarrow \pi \pi \pi$ contact term.
- [55] A. Quenzer *et al.*, Phys. Lett. **B76**, 512 (1978), Pion Form-Factor from 480-MeV to 1100-MeV.
- [56] L. M. Barkov *et al.*, Nucl. Phys. **B256**, 365 (1985), Electromagnetic Pion Form-Factor in the Timelike Region.
- [57] CMD-2, R. R. Akhmetshin *et al.*, Phys. Lett. **B578**, 285 (2004), hep-ex/0308008, Re-analysis of hadronic cross section measurements at CMD-2.
- [58] CMD-2, R. R. Akhmetshin *et al.*, Phys. Lett. **B648**, 28 (2007), hep-ex/0610021, High-statistics measurement of the pion form factor in the rho-meson energy range with the CMD-2 detector.
- [59] R. R. Akhmetshin *et al.*, JETP Lett. **84**, 413 (2006), hep-ex/0610016, Measurement of the $e^+ e^- \rightarrow \pi^+ \pi^-$ cross section with the CMD-2 detector in the 370-MeV - 520-MeV cm energy range.
- [60] M. N. Achasov *et al.*, J. Exp. Theor. Phys. **103**, 380 (2006), hep-ex/0605013, Update of the $e^+ e^- \rightarrow \pi^+ \pi^-$ cross section measured by SND detector in the energy region $400\text{-MeV} < \sqrt{s} < 1000\text{-MeV}$.
- [61] M. Benayoun, S. Eidelman, V. Ivanchenko, and Z. Silagadze, Mod.Phys.Lett. **A14**, 2605 (1999), hep-ph/9910523, Spectroscopy at B factories using hard photon emission.
- [62] KLOE, G. Venanzoni *et al.*, AIP Conf. Proc. **1182**, 665 (2009), 0906.4331, A precise new KLOE measurement of $|F_\pi|^2$ with ISR events and determination of $\pi\pi$ contribution to a_μ for $0.592 < M_{\pi\pi} < 0.975$ GeV.
- [63] KLOE, F. Ambrosino *et al.*, Phys.Lett. **B700**, 102 (2011), 1006.5313, Measurement of $\sigma(e^+ e^- \rightarrow \pi^+ \pi^-)$ from threshold to 0.85 GeV^2 using Initial State Radiation with the KLOE detector.
- [64] KLOE Collaboration, D. Babusci *et al.*, Phys.Lett. **B720**, 336 (2013), 1212.4524, Precision measurement of $\sigma(e^+ e^- \rightarrow \pi^+ \pi^- \gamma) / \sigma(e^+ e^- \rightarrow \mu^+ \mu^- \gamma)$ and determination of the $\pi^+ \pi^-$ contribution to the muon anomaly with the KLOE detector.

- [65] BABAR, B. Aubert *et al.*, Phys. Rev. Lett. **103**, 231801 (2009), 0908.3589, Precise measurement of the $e^+e^- \rightarrow \pi^+\pi^-(\gamma)$ cross section with the Initial State Radiation method at BABAR.
- [66] BABAR Collaboration, J. Lees *et al.*, Phys.Rev. **D86**, 032013 (2012), 1205.2228, Precise Measurement of the $e^+e^- \rightarrow \pi^+\pi^-(\gamma)$ Cross Section with the Initial-State Radiation Method at BABAR.
- [67] BESSIII, M. Ablikim *et al.*, (2015), 1507.08188, Measurement of the $e^+e^- \rightarrow \pi^+\pi^-$ Cross Section between 600 and 900 MeV Using Initial State Radiation.
- [68] T. Xiao, S. Dobbs, A. Tomaradze, K. K. Seth, and G. Bonvicini, (2017), 1712.04530, Precision Measurement of the Hadronic Contribution to the Muon Anomalous Magnetic Moment.
- [69] C. Hanhart *et al.*, Eur. Phys. J. **C77**, 98 (2017), 1611.09359, The branching ratio $\omega \rightarrow \pi^+\pi^-$ revisited.
- [70] KLOE-2, A. Anastasi *et al.*, JHEP **03**, 173 (2018), 1711.03085, Combination of KLOE $\sigma(e^+e^- \rightarrow \pi^+\pi^-\gamma(\gamma))$ measurements and determination of $a_\mu^{\pi^+\pi^-}$ in the energy range $0.10 < s < 0.95 \text{ GeV}^2$.
- [71] A. Keshavarzi, D. Nomura, and T. Teubner, (2018), 1802.02995, The muon $g - 2$ and $\alpha(M_Z^2)$: a new data-based analysis.
- [72] R. R. Akhmetshin *et al.*, Phys. Lett. **B364**, 199 (1995), Measurement of phi meson parameters with CMD-2 detector at VEPP-2M collider.
- [73] CMD-2, R. R. Akhmetshin *et al.*, Phys. Lett. **B669**, 217 (2008), 0804.0178, Measurement of $e^+e^- \rightarrow \phi \rightarrow K^+K^-$ cross section with the CMD-2 detector at VEPP-2M Collider.
- [74] M. N. Achasov *et al.*, Phys. Rev. **D63**, 072002 (2001), Measurements of the parameters of the phi(1020) resonance through studies of the processes $e^+e^- \rightarrow K^+K^-$, $K_S K_L$, and $\pi^+\pi^-\pi^0$.
- [75] E. Solodov, $g - 2$ Theory Initiative Workshop **Mainz June 22nd** (2018), News from CMD-3, SND Experiments at VEPP2000.
- [76] BaBar, J. P. Lees *et al.*, Phys. Rev. **D88**, 032013 (2013), 1306.3600, Precision measurement of the $e^+e^- \rightarrow K^+K^-$ cross section with the initial-state radiation method at BABAR.
- [77] E. A. Kozyrev *et al.*, (2017), 1710.02989, Study of the process $e^+e^- \rightarrow K^+K^-$ in the center-of-mass energy range 1010–1060 MeV with the CMD-3 detector.
- [78] CMD-2, R. R. Akhmetshin *et al.*, Phys. Lett. **B578**, 285 (2004), hep-ex/0308008, Re-analysis of Hadronic Cross Section Measurements at CMD- 2.

- [79] CMD-3, E. A. Kozyrev *et al.*, Phys. Lett. **B760**, 314 (2016), 1604.02981, Study of the process $e^+e^- \rightarrow K_S K_L$ in the center-of-mass energy range 1004–1060 MeV with the CMD-3 detector at the VEPP-2000 e^+e^- collider.
- [80] CMD2, R. R. Akhmetshin *et al.*, Phys. Lett. **B605**, 26 (2005), hep-ex/0409030, Study of the Processes $e^+e^- \rightarrow \eta\gamma$, $e^+e^- \rightarrow \pi^0\gamma \rightarrow 3\gamma$ in the c.m. Energy Range 600–1380 MeV at CMD-2.
- [81] SND, M. N. Achasov *et al.*, Phys. Rev. **D93**, 092001 (2016), 1601.08061, Study of the reaction $e^+e^- \rightarrow \pi^0\gamma$ with the SND detector at the VEPP-2M collider.
- [82] M. N. Achasov *et al.*, Phys. Lett. **B559**, 171 (2003), hep-ex/0302004, Experimental study of the $e^+e^- \rightarrow \pi^0\gamma$ process in the energy region $\sqrt{s} = 0.60 - 0.97$ GeV.
- [83] M. N. Achasov *et al.*, Eur. Phys. J. **C12**, 25 (2000), Experimental study of the processes $e^+e^- \rightarrow \phi \rightarrow \eta\gamma, \pi^0\gamma$ at VEPP-2M.
- [84] CMD2, R. R. Akhmetshin *et al.*, Phys. Lett. **B460**, 242 (1999), hep-ex/9907003, Study of the radiative decay $\phi \rightarrow \eta\gamma$ with CMD-2 detector.
- [85] CMD-2, R. R. Akhmetshin *et al.*, Phys. Lett. **B509**, 217 (2001), hep-ex/0103043, Study of the Process $e^+e^- \rightarrow \eta\gamma$ in c.m. Energy Range 600–1380 MeV at CMD-2.
- [86] M. N. Achasov *et al.*, Phys. Rev. **D76**, 077101 (2007), 0709.1007, Reanalysis of the $e^+e^- \rightarrow \eta\gamma$ reaction cross section.
- [87] R. R. Akhmetshin *et al.*, Phys. Lett. **B642**, 203 (2006), Study of $\phi \rightarrow \pi^+\pi^-\pi^0$ with CMD-2 detector.
- [88] R. R. Akhmetshin *et al.*, Phys. Lett. **B434**, 426 (1998), Study of dynamics of $\phi \rightarrow \pi^+\pi^-\pi^0$ decay with CMD-2 detector.
- [89] M. N. Achasov *et al.*, Phys. Rev. **D68**, 052006 (2003), hep-ex/0305049, Study of the process $e^+e^- \rightarrow \pi^+\pi^-\pi^0$ in the energy region \sqrt{s} below 0.98 GeV.
- [90] M. N. Achasov *et al.*, Phys. Rev. **D66**, 032001 (2002), hep-ex/0201040, Study of the process $e^+e^- \rightarrow \pi^+\pi^-\pi^0$ in the energy region \sqrt{s} from 0.98 to 1.38 GeV.
- [91] S. I. Dolinsky *et al.*, Phys. Rept. **202**, 99 (1991), Summary of experiments with the neutral detector at the e^+e^- storage ring VEPP-2M.
- [92] M. Hoferichter, B. Kubis, S. Leupold, F. Niecknig, and S. P. Schneider, Eur. Phys. J. **C74**, 3180 (2014), 1410.4691, Dispersive analysis of the pion transition form factor.
- [93] E. B. Dally *et al.*, Phys. Rev. Lett. **48**, 375 (1982), Elastic Scattering Measurement of the Negative Pion Radius.
- [94] E. B. Dally *et al.*, Phys. Rev. Lett. **45**, 232 (1980), Direct Measurement of the Negative Kaon Form Factor.

- [95] B. C.J. *et al.*, Phys. Rev **D17**, 1693 (1978), Electroproduction of Single Pions at low Q^2 and a Measurement of the Pion Form Factor up to $Q^2 = 10 \text{ GeV}^2$.
- [96] Jefferson Lab F(pi), J. Volmer *et al.*, Phys. Rev. Lett. **86**, 1713 (2001), nucl-ex/0010009, Measurement of the Charged Pion Electromagnetic Form-Factor.
- [97] Jefferson Lab F(pi), V. Tadevosyan *et al.*, Phys. Rev. **C75**, 055205 (2007), nucl-ex/0607007, Determination of the pion charge form factor for $Q^2=0.60\text{--}1.60 \text{ GeV}^2$.
- [98] Jefferson Lab, H. P. Blok *et al.*, Phys. Rev. **C78**, 045202 (2008), 0809.3161, Charged pion form factor between $Q^2=0.60$ and 2.45 GeV^2 . I. Measurements of the cross section for the $^1\text{H}(e, e'\pi^+)n$ reaction.
- [99] Jefferson Lab, G. M. Huber *et al.*, Phys. Rev. **C78**, 045203 (2008), 0809.3052, Charged pion form-factor between $Q^2 = 0.60 \text{ GeV}^2$ and 2.45 GeV^2 . II. Determination of, and results for, the pion form-factor.
- [100] H. Ackermann *et al.*, Nucl. Phys. **B137**, 294 (1978), Determination of the Longitudinal and the Transverse Part in π^+ Electroproduction .
- [101] P. Brauel *et al.*, Z. Phys. **C3**, 101 (1979), Electroproduction of π^+n , π^-n and $K^+\Lambda$, $K^+\Sigma^0$ Final States above the Resonance Region .
- [102] NA48, A. Lai *et al.*, Eur. Phys. J. **C30**, 33 (2003), Investigation of $K(L,S) \rightarrow \pi^+\pi^-e^+e^-$ decays.
- [103] KTeV, E. Abouzaid *et al.*, Phys. Rev. Lett. **96**, 101801 (2006), hep-ex/0508010, A Measurement of the K^0 charge radius and a CP violating asymmetry together with a search for CP violating e^+ direct photon emission in the rare decay $K(L) \rightarrow \pi^+\pi^-e^+e^-$.
- [104] R. W. Peelle, Informal Memorandum, Oak Ridge National Laboratory, TN, USA (1987), Peelle's Pertinent Puzzle.
- [105] R. Fruehwirth, D. Neudecker, and H. Leeb, EPJ Web of Conferences **27**, 00008 (2012), Peelle's Pertinent Puzzle and its Solution.
- [106] S. Ciba and D. Smith, Nuclear Data and Measurements Series, Argonne National Laboratory, Argonne, IL, USA ANL/NDM-121 (1991), A suggested procedure for resolving an anomaly in Least-squares data analysis known as 'Peelle's Pertinent Puzzle' and the general implications for nuclear data evaluation.
- [107] NNPDF, R. D. Ball *et al.*, JHEP **5**, 075 (2010), 0912.2276, Fitting Parton Distribution Data with Multiplicative Normalization Uncertainties.
- [108] BaBar, J. P. Lees *et al.*, Phys. Rev. **D89**, 092002 (2014), 1403.7593, Cross sections for the reactions $e^+e^- \rightarrow K_S^0 K_L^0$, $K_S^0 K_L^0 \pi^+ \pi^-$, $K_S^0 K_S^0 \pi^+ \pi^-$, and $K_S^0 K_S^0 K^+ K^-$ from events with initial-state radiation.
- [109] M. Guidal, J. M. Laget, and M. Vanderhaeghen, Nucl. Phys. **A627**, 645 (1997), Pion and kaon photoproduction at high-energies: Forward and intermediate angles.

- [110] M. Vanderhaeghen, M. Guidal, and J. M. Laget, Phys. Rev. **C57**, 1454 (1998), Regge description of charged pseudoscalar meson electroproduction above the resonance region.
- [111] J. Koponen, F. Bursa, C. T. H. Davies, R. J. Dowdall, and G. P. Lepage, Phys. Rev. **D93**, 054503 (2016), 1511.07382, Size of the pion from full lattice QCD with physical u , d , s and c quarks.
- [112] ETM, C. Alexandrou *et al.*, Phys. Rev. **D97**, 014508 (2018), 1710.10401, Pion vector form factor from lattice QCD at the physical point.
- [113] ETM, A. Abdel-Rehim *et al.*, Phys. Rev. **D95**, 094515 (2017), 1507.05068, First physics results at the physical pion mass from $N_f = 2$ Wilson twisted mass fermions at maximal twist.
- [114] G. Colangelo, M. Hoferichter, and P. Stoffer, JHEP **02**, 006 (2019), 1810.00007, Two-pion contribution to hadronic vacuum polarization.
- [115] B. Ananthanarayan, I. Caprini, and D. Das, Phys. Rev. Lett. **119**, 132002 (2017), 1706.04020, Electromagnetic charge radius of the pion at high precision.
- [116] J. Bijnens, G. Colangelo, and P. Talavera, JHEP **05**, 014 (1998), hep-ph/9805389, The Vector and scalar form-factors of the pion to two loops.
- [117] J. Bijnens and P. Talavera, JHEP **03**, 046 (2002), hep-ph/0203049, Pion and kaon electromagnetic form-factors.
- [118] S. Aoki *et al.*, Eur. Phys. J. **C77**, 112 (2017), 1607.00299, Review of lattice results concerning low-energy particle physics.
- [119] B. Hyams *et al.*, Nucl. Phys. **B64**, 134 (1973), $\pi\pi$ Phase Shift Analysis from 600-MeV to 1900-MeV.
- [120] B. Ananthanarayan, G. Colangelo, J. Gasser, and H. Leutwyler, Phys. Rept. **353**, 207 (2001), hep-ph/0005297, Roy equation analysis of $\pi\pi$ scattering.
- [121] S. D. Protopopescu *et al.*, Phys. Rev. **D7**, 1279 (1973), $\pi\pi$ Partial Wave Analysis from Reactions $\pi^+p \rightarrow \pi^+\pi^-\Delta^{++}$ and $\pi^+p \rightarrow K^+K^-\Delta^{++}$ at 7.1-GeV/c.
- [122] G. Colangelo, J. Gasser, and H. Leutwyler, Nucl.Phys. **B603**, 125 (2001), hep-ph/0103088, $\pi\pi$ scattering.
- [123] P. Estabrooks *et al.*, Nucl. Phys. **B81**, 70 (1974), $\rho - \omega$ interference in $\pi^-p \rightarrow \pi^-\pi^+n$ at 17.2 GeV.
- [124] G. Colangelo, Nucl. Phys. Proc. Suppl. **131**, 185 (2004), hep-ph/0312017, Hadronic contributions to $a(\mu)$ below one-GeV.
- [125] Particle Data Group, K. Nakamura *et al.*, J. Phys. **G37**, 075021 (2010), Review of Particle Physics.

- [126] M. Davier, S. Eidelman, A. Hocker, and Z. Zhang, Eur. Phys. J. **C27**, 497 (2003), hep-ph/0208177, Confronting spectral functions from e^+e^- annihilation and tau decays: Consequences for the muon magnetic moment.
- [127] M. Davier, S. Eidelman, A. Hocker, and Z. Zhang, Eur. Phys. J. **C31**, 503 (2003), hep-ph/0308213, Updated estimate of the muon magnetic moment using revised results from e^+e^- annihilation.
- [128] N. M. Kroll, T. D. Lee, and B. Zumino, Phys. Rev. **157**, 1376 (1967), Neutral Vector Mesons and the Hadronic Electromagnetic Current.
- [129] F. Jegerlehner, EPJ Web Conf. **218**, 01003 (2019), 1711.06089, Variations on Photon Vacuum Polarization.
- [130] M. Davier, A. Hoecker, B. Malaescu, and Z. Zhang, Eur. Phys. J. **C77**, 827 (2017), 1706.09436, Reevaluation of the hadronic vacuum polarisation contributions to the Standard Model predictions of the muon $g - 2$ and $\alpha(m_Z^2)$ using newest hadronic cross-section data.
- [131] A. Kurz, T. Liu, P. Marquard, and M. Steinhauser, Phys.Lett. **B734**, 144 (2014), 1403.6400, Hadronic contribution to the muon anomalous magnetic moment to next-to-next-to-leading order.
- [132] J. Prades, E. de Rafael, and A. Vainshtein, (2009), 0901.0306, Hadronic Light-by-Light Scattering Contribution to the Muon Anomalous Magnetic Moment.
- [133] G. Colangelo, M. Hoferichter, A. Nyffeler, M. Passera, and P. Stoffer, Phys.Lett. **B735**, 90 (2014), 1403.7512, Remarks on higher-order hadronic corrections to the muon $g - 2$.
- [134] M. Passera, Phys.Rev. **D75**, 013002 (2007), hep-ph/0606174, Precise mass-dependent QED contributions to leptonic $g-2$ at order α^2 and α^3 .
- [135] F. Jegerlehner, Acta Phys.Polon. **B44**, 2257 (2013), 1312.3978, Application of Chiral Resonance Lagrangian Theories to the Muon $g - 2$.
- [136] F. Jegerlehner and A. Nyffeler, Phys. Rept. **477**, 1 (2009), 0902.3360, The Muon $g-2$.
- [137] C. T. H. Davies *et al.*, (2019), 1902.04223, Hadronic-vacuum-polarization contribution to the muon's anomalous magnetic moment from four-flavor lattice QCD.
- [138] ETMC, D. Giusti and S. Simula, PoS **LATTICE2019**, 104 (2019), 1910.03874, Lepton anomalous magnetic moments in Lattice QCD+QED.
- [139] RBC, UKQCD, T. Blum *et al.*, Phys. Rev. Lett. **121**, 022003 (2018), 1801.07224, Calculation of the hadronic vacuum polarization contribution to the muon anomalous magnetic moment.
- [140] Budapest-Marseille-Wuppertal, S. Borsanyi *et al.*, Phys. Rev. Lett. **121**, 022002 (2018), 1711.04980, Hadronic vacuum polarization contribution to the anomalous magnetic moments of leptons from first principles.

- [141] A. Grardin *et al.*, Phys. Rev. **D100**, 014510 (2019), 1904.03120, The leading hadronic contribution to $(g - 2)_\mu$ from lattice QCD with $N_f = 2 + 1$ flavours of $O(a)$ improved Wilson quarks.
- [142] I. Danilkin, C. F. Redmer, and M. Vanderhaeghen, (2019), 1901.10346, The hadronic light-by-light contribution to the muon's anomalous magnetic moment.
- [143] M. Benayoun, P. David, L. DelBuono, and F. Jegerlehner, (2016), 1605.04474, A BHLS model based moment analysis of muon g-2, and its use for lattice QCD evaluations of a_μ^{had} .
- [144] H. Leutwyler, Phys.Lett. **B374**, 181 (1996), hep-ph/9601236, Implications of $\eta - \eta'$ mixing for the decay $\eta \rightarrow 3\pi$.